E-472

MEASUREMENT OF ϕ MESON PRODUCTION IN PROTON-NUCLEUS COLLISIONS AT 400 GeV/c

by

David Stanley Koltick

A dissertation submitted in partial fulfillment
of the requirements for the degree of
Doctor of Philosophy
(Physics)
at The University of Michigan
1978

Doctoral Committee:

Associate Professor Rudolf Thun, Chairman
Professor Carl W. Akerlof
Associate Professor Michael Bretz
Professor Gordon L. Kane
Associate Professor Richard L. Sears

ABSTRACT

MEASUREMENT OF ϕ MESON PRODUCTION IN PROTON-NUCLEUS COLLISIONS AT 400 GeV/c

by

David Stanley Koltick

Chairman: Rudolf Thun

ϕ meson production has been observed in 400 GeV/c proton-nucleus collisions using a high resolution double arm spectrometer, centered near 90 degrees in the center-of-mass. An accurate measurement of the ϕ mass and width was made and an analysis of the systematic error in the measurements was carried out. The inclusive ϕ invariant cross section was measured over the range $0.8 \leq P_{\perp} \leq 3.5$ GeV/c and the slope parameter was found. The ϕ/π^- ratio as a function of $P_{\perp}$ was measured and compared to the thermodynamic model and the Field and Feynman model. The comparison suggested that ϕ production may be dominated by different mechanisms at low and high $P_{\perp}$. Using the measured ϕ/π^- ratio and the known $\phi \rightarrow \mu^+\mu^-$ branching ratio, the ϕ meson's contribution to the prompt μ/π ratio was found as a function transverse momentum. The ϕ meson's contribution was found to be almost 2 orders of magnitude below the total μ/π ratio. A test of the Okubo-Zweig-Iizuka (O-Z-I) rule was made by searching for an enhancement of K mesons produced in association with the ϕ. No enhancement was found,

indicating a possible violation of the O-Z-I rule. This lack of enhancement could not be explained away by ϕ production through nonstrange quarks in its wave function.

ACKNOWLEDEMENTS

I would like to thank Rudi Thun, my thesis advisor, and Carl Akerlof for their continuous support and advice while doing my research work at The University of Michigan. I would also like to thank David Bintinger at Fermi Lab for the many discussions about the data and the analysis and for his friendship.

I would also like to acknowledge my fellow graduate students David Finley, Ralph Fabrizio, and Phil Kraushaar for working on the experiment.

This experiment took the efforts of many people working both directly and indirectly for its completion. I want to thank Rod Ditzler, Orland Johnson, Frank Loeffler, and Ed Shibata of Purdue University, Drasko Yovanovitch, Ken Stanfield, and Bob Loveless of Fermi National Accelerator Laboratory, Paul Alley and Don Meyer of The University of Michigan for working on the experiment and teaching me about experimental physics. I would also like to thank Fermi Lab for supporting the experiment and for the pleasant working environment at the laboratory.

In addition, I would like to thank my wife, Rhoda, for understanding my desire to work in high energy physics and for all the help and encouragment she has given me.

TABLE OF CONTENTS

Page

LIST OF TABLES

LIST OF ILLUSTRATIONS

CHAPTER I

INTRODUCTION

The original purpose of the experiment was to look for massive (> 1.5 GeV/c^2), narrow width (< 10 MeV/c^2) particles. More specifically, we searched for the charmed D^o in its predicted decay to a charged π meson and a charged K meson[1]. To make this observation, a high resolution double arm spectrometer was set up in the Meson Lab at Fermi National Accelerator Laboratory. But as is often the case with experimental science, what one finds and what one is looking for can be two different things. We did not observe the D^o, but did set strong upper limits on its production cross section in hadron reactions[2]. In fact, to date no one has yet observed the D^o in a hadronic production experiment. One of the very interesting things we did observe was the ϕ meson[3].

The ϕ meson was observed in our experiment through its decay into a pair of charged K mesons (Figure 1). The sum of the two K meson masses is almost that of the ϕ meson, so the momentum of each K meson in the rest frame of the ϕ is small (128 MeV/c). This fact allowed the ϕ meson decay products to be detected in a single spectrometer arm. For

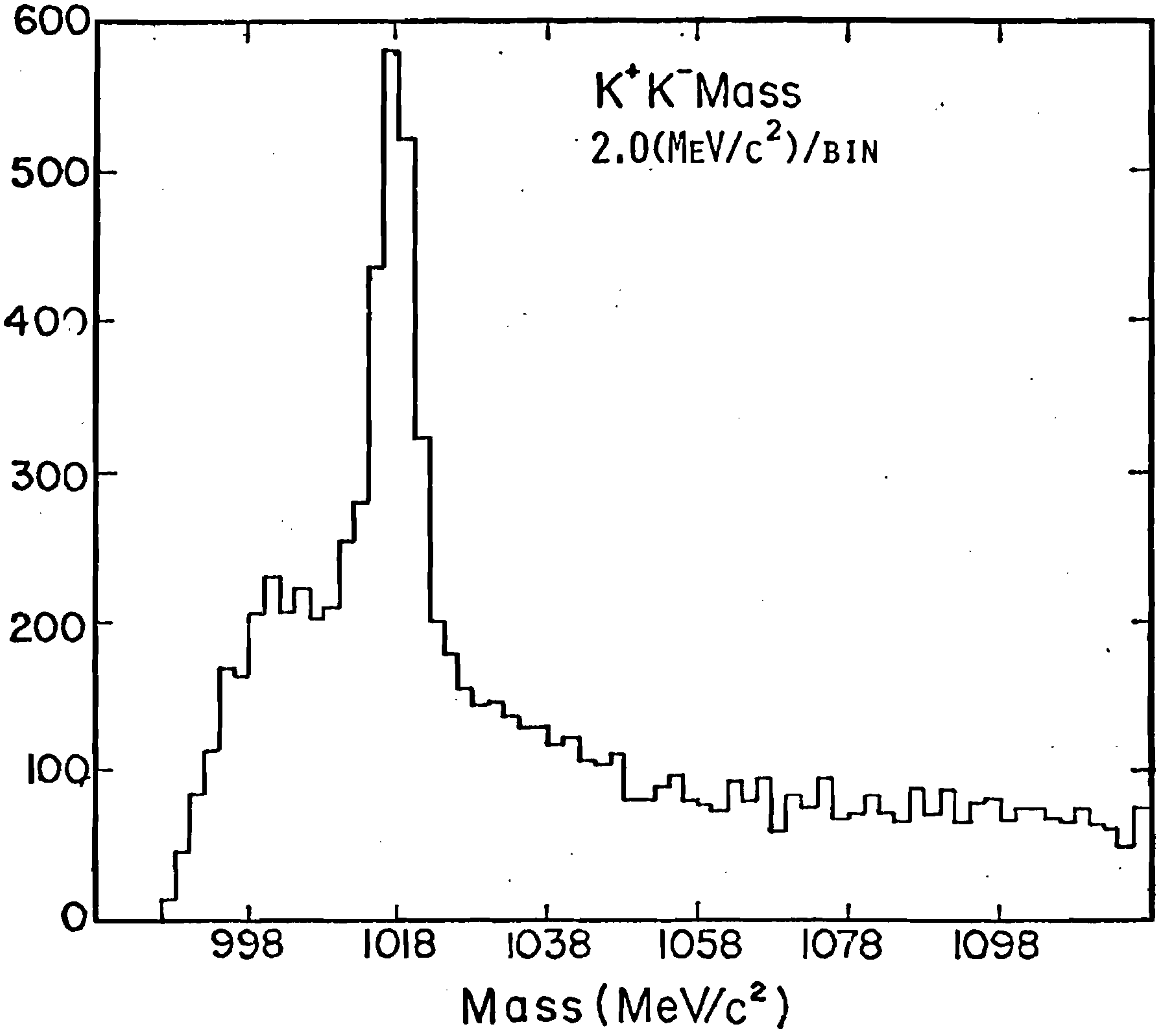

Figure 1. The number of observed events consistent with being a K^+ K^- pair versus the invariant mass of the pair. A clear ϕ signal is observed. The mass resolution in the ϕ mass region is less than 1 MeV/c^2 or about 1/2 a bin width.

this reason, ϕ meson data were taken in two forms. In the first form only one spectrometer arm was used to initiate data-taking. This mode allowed for an accurate measurement of: 1) the mass and width of the ϕ meson; 2) the invariant ϕ meson cross section as a function of transverse momentum; 3) the ϕ meson to π^- meson ratio as a function of transverse momentum, and by using the known branching ratio for the ϕ meson decay to a $\mu^+\mu^-$ pair, the ϕ meson's contribution to the prompt μ/π ratio as a function of momentum. The other mode of data-taking was the D^0 search mode in which a particle was demanded in each spectrometer arm. In this mode, the strength of the correlation of the ϕ meson to K mesons can be measured and compared to the correlation of a K^+ meson to a K^- meson. This comparison can be used to check if ϕ meson production at high energies is consistent with Zweig's rule.

The ϕ meson is of current interest because of its relationship to the other vector mesons (Table 1) and the "new" physics. The new physics is concerned with quark spectroscopy and how quarks bind together to form hadrons. The vector mesons are of great interest in this respect because they couple directly to the photon of electromagnetism, which makes their detection relatively easy. For this reason, detection of a new vector meson has become the experimenter's signal to the onset of a new quark species or quark quantum number "flavor". Although the vector

Vector Mesons $J^P = 1^-$

Particle	Mass	Quark Wave Function	Width
ρ	0.776 GeV/c^2	$\frac{u\bar{u} - d\bar{d}}{\sqrt{2}}$	155 MeV/c^2
ω	0.783 GeV/c^2	$\frac{u\bar{u} + d\bar{d}}{\sqrt{2}}$	10 MeV/c^2
ϕ	1.019 GeV/c^2	$s\bar{s}$	4 MeV/c^2
Ψ	3.098 GeV/c^2	$c\bar{c}$	70 KeV/c^2
Υ	9.45 GeV/c^2	$b\bar{b}$	Γ_{ee} = 1.3 KeV/c^2

Table 1. The lowest lying meson states which contain the "hidden" flavor quantum numbers u, d, s, c, and b. These vector mesons have a total angular momentum of J = 1 and negative parity, the same quantum numbers as the photon. The total width of the Υ has not been measured.

mesons do not exhibit this new quantum flavor, they are said to have hidden flavor.

The now famous J/Ψ meson has the hidden quantum flavor of charm. The ϕ meson has the hidden quantum flavor of strangeness. These hidden flavor systems are thought to be positronium-like systems; that is, a bound state system of a particle and an anti-particle, except that the binding force in the mesons is that of the strong interaction and not the electromagnetic interaction. The lowest lying vector mesons have the same quantum numbers as ortho-positronium, or that of a photon. The flavor quantum number and the lepton number are similar in that each is separately conserved by the strong and the electromagnetic interaction.

CHAPTER II

THEORY

A current theory of the strong interaction, Quantum Chromodynamics (QCD), attempts to quantitatively explain the strong interactions of hadrons in terms of hadron constituents, quarks and gluons. Whether or not the present mathematical form of this theory is correct will not be of importance to the discussion that follows. Many high energy physicists feel the underlying ideas of the theory are correct. It is these basic ideas I want to discuss. The evolution and coherence of the theory makes a discussion of these ideas simpler.

Quantum Chromodynamics

The fundamental particles of the theory are spin 1/2 fermions, called quarks, which are bound together by vector gluons to form hadrons. QCD, a gauge theory with a local SU(3) color symmetry[4], is a generalization of Quantum Electrodynamics (QED). The main differences between QCD and QED are:

a.) There are eight massless, electrically neutral gluons with a quantum number color, compared to only one electrically neutral, colorless photon in QED.

b.) The coupling constant, α_s, is a function of the interaction energy, E, instead of being a universal constant.

Because free quarks have never been observed[5], the color force is believed to confine the quarks to exist only inside a hadron. The color quantum number is also believed to be a non-observable. Color, being a perfect local symmetry, allows only color neutral states to be observables. The interaction of quarks through the color force has a short distance or high energy behavior described by asymptotic freedom. The idea of asymptotic freedom is contained in the energy dependence of the strong coupling constant[6],

$$\alpha_s(E) \simeq \frac{\alpha_o(E_o)}{1 + C \cdot \alpha_o(E_o) \cdot \ln(E/E_o)} \qquad 2.1$$

E_o is an arbitrary normalization energy. C is a constant. As can be seen, the greater the interaction energy or shorter the interaction distance, the weaker the coupling between the quarks. As the interaction energy between the quarks becomes large, the coupling constant goes to zero and the asymptotic behavior of the quarks is to act as free particles.

ϕ-ω Mixing

The ϕ meson has played a role in the development of these ideas, starting with the eight-fold way[7] (quark model) of Gell-mann. The quark model mass formula developed for the lowest lying baryon octet was experimentally well satisfied. However, the corresponding linear mass formula for the $J^P = 1^-$ vector octet[8]

$$m(K^*) = \frac{1}{4}\{3m(\omega_8) + m(\rho)\} \qquad 2.2$$

predicted a mass value for $m(\omega_8)$ of 931 MeV/c^2, which is between the experimental values of two vector mesons $m(\phi)$ = 1020 MeV/c^2 and $m(\omega)$ = 783 MeV/c^2.

In order to account for the difference between the group theoretic predictions and the physical states, Sakurai proposed the ω-ϕ mixing model[9]. The physical states ϕ and ω were coherent mixtures of the singlet ω_o and octet ω_8 eigen states:

$$\begin{bmatrix} \phi \\ \omega \end{bmatrix} = \begin{bmatrix} \cos\theta & -\sin\theta \\ \sin\theta & \cos\theta \end{bmatrix} \begin{bmatrix} \omega_8 \\ \omega_o \end{bmatrix} \qquad 2.3$$

where

$$\omega_o = \frac{1}{\sqrt{3}} (u\bar{u} + d\bar{d} + s\bar{s})$$
$$\omega_8 = \frac{1}{\sqrt{6}} (u\bar{u} + d\bar{d} - 2s\bar{s}) \qquad 2.4$$

Using equation 2.2 and 2.3, the mixing angle is found to be $\theta = 37.5 \pm 0.3$ degrees.

Having solved the mass problem another problem arises. Why is the partial width of the decay $\phi \rightarrow \pi^+ \pi^- \pi^o$ (0.67 MeV/c^2) so small compared to the partial width of the decay $\omega \rightarrow \pi^+ \pi^- \pi^o$ (9.0 MeV/c^2)? The phase space for $\phi \rightarrow 3\pi$ is much larger than $\omega \rightarrow 3\pi$; just the opposite would have been expected.

The very small width of the ϕ to 3π decay was explained by the Ideal Mixing Model of ω-ϕ proposed by Okubo[9]. Using SU(6) relationships among the coupling constants involved in the decays, and combining the vector octet and

and singlet to form a nonet, Okubo found the mixing angle $\theta = \tan^{-1}(\frac{1}{\sqrt{2}})$. This angle is called the ideal mixing angle because it is only this value of θ for which the matrix element for the decay $\phi \rightarrow 3\pi$ is zero. Other values will allow the transition.

This result was more clearly understood when it was reinterpreted in terms of the quark model by Zweig[11] and later independently by Iizuka[12]. In the quark model, ideal mixing implies:

$$\begin{aligned} \phi &= s\bar{s} \\ \omega &= \frac{1}{\sqrt{2}}(u\bar{u} + d\bar{d}) \end{aligned} \qquad 2.5$$

This means the ϕ is a state made up of a strange and an anti-strange quark while the ω is a state made of ordinary up and down quarks. The reinterpretation is that the strange and anti-strange quarks in the ϕ meson are inhibited to annihilate and reappear as a 3π state. This then forms the basis for what is today called the Okubo-Zweig-Iizuka (O-Z-I) rule.

The O-Z-I Rule

The O-Z-I rule is only qualitative and can be stated as:[11,12,13]

> Quarks in a hadron do not annihilate. Instead production and decay take place by connected quark diagrams.

The rule seems well satisfied in the case of the ϕ meson. Its decays are used to illustrate the rule in Figure 2. The

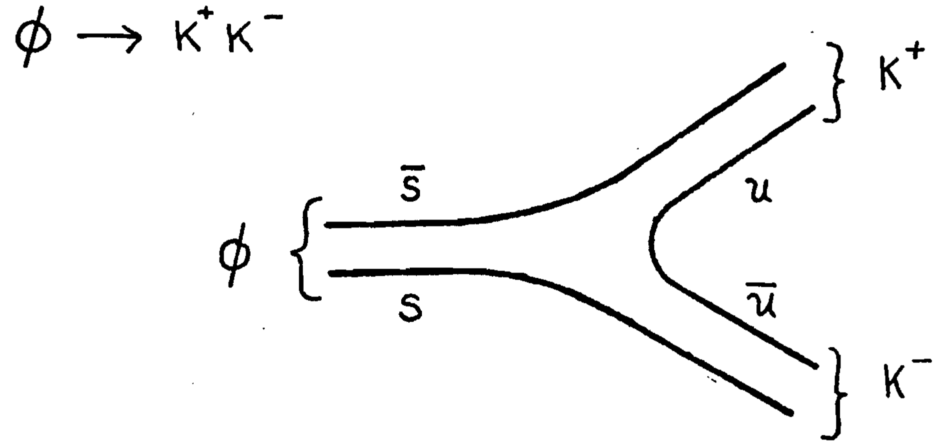

Figure 2A. O-Z-I allowed decay of the ϕ meson.

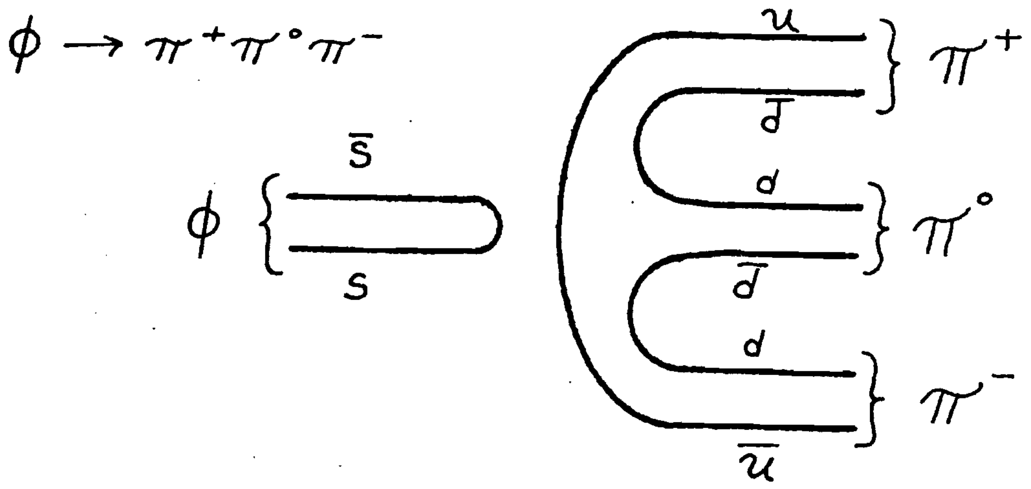

Figure 2B. O-Z-I violating decay of the ϕ meson.

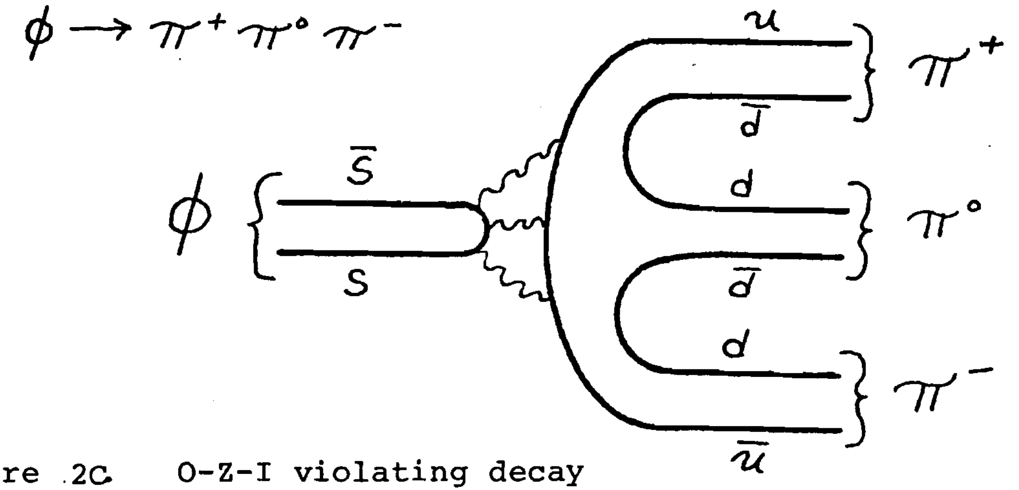

Figure 2C O-Z-I violating decay of the ϕ meson showing the 3 gluons expected by QCD.

dominate ϕ meson decay mode is the O-Z-I-allowed mode, $\phi \rightarrow K\bar{K}$, with a branching ratio of 82% (Figure 2). The ϕ has an O-Z-I-forbidden decay mode $\phi \rightarrow 3\pi$, which has a branching ratio of 16%. This decay is shown in Figure 2B by a disconnected diagram. If the larger phase space of the 3π decay is taken into account, it is estimated that the 3π decay suppression factor is greater than 50 in the transition rate[14].

The 3π transition rate shows that a small amount of nonstrange quarks are mixed into the wave function of the ϕ meson[15]. Recently, measurements of ω and ϕ production in $\pi^{\pm}$-nucleon reactions have been made[16] whose quark model interpretation measures the fraction of nonstrange quarks in the ϕ meson[17]. The measurement gives a mixing angle for ω-ϕ of $\theta = 38.5 \pm 0.5$. Using this value in equation 2.3, the ϕ meson quark wave function is found to be:

$$|\phi\rangle = -0.056 \, \frac{(|u\bar{u}\rangle + |d\bar{d}\rangle)}{\sqrt{2}} - 0.998|s\bar{s}\rangle \qquad 2.6$$

This, then, is the best estimate of the ϕ meson's wave function and exhibits the degree to which O-Z-I violations are expected to occur.

The O-Z-I rule as I have stated it is only qualitative. QCD tries to make the rule more quantitative using gluons and their energy dependent coupling constant[18]. In the connected diagrams the interaction between quarks is provided by "soft" gluons and hence α_s is large and so is the transition rate.

In the disconnected diagrams "hard" gluons are exchanged so α_s is small and likewise the transition rate is small. Take the decay $\phi \rightarrow 3\pi$ as an example and ask how many vector gluons have to be exchanged to go from an $s\bar{s}$ state to a 3π state. The minimum is 3. One is ruled out because of the conservation of color charge. Two is forbidden by charge conjugation. This can be compared to ortho-positronium which decays into 3 photons. Here, one photon decay is forbidden by energy and momentum conservation. Two is forbidden by charge conjugation. Both QED and QCD predict a suppression in the transition rate, which goes like

$$\{\alpha_s(E)\}^n \qquad 2.7$$

where n is the number of "gluons". α_s is estimated to be 0.47 for the ϕ meson.[18]

ϕ Production

We would like to apply these ideas to particle production in high energy collisions, but the theory is not developed enough to do this. We can, however, ask a global question: Does particle production in high energy collisions proceed through O-Z-I allowed processes? Observation of ϕ meson production can give an answer to this question. If O-Z-I production dominates, two strange particles would be produced along with the ϕ . This is illustrated in Figure 3, with the production of ϕ-K-$\bar{K}$. If O-Z-I violating processes dominated, the ϕ meson could be produced alone, or if with strange particles, the ϕ would not be correlated to them.

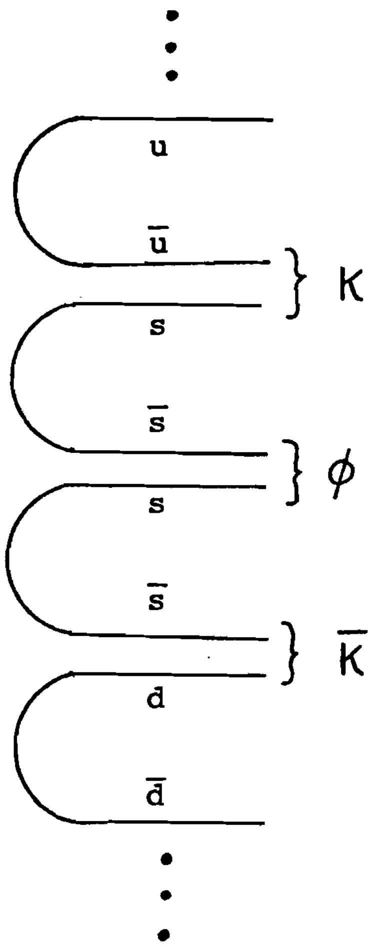

Figure 3. φ meson production in an O-Z-I allowed process. This diagram shows the quark lines in the central rapidity region of a proton-nucleus collision.

This idea can be checked using our data by looking for a correlation between ϕ mesons and K mesons.

Recently a model has been developed in which particles are produced in an O-Z-I allowed manner and which makes a prediction for ϕ meson production. This model by Field and Feynman[19] is based on the asymptotic freedom idea that the short distance interactions between quarks should be point-like and observable in the large transverse products of hadron interactions. In fact, the model completely leaves out any aspect of gluons in a hadron, even though from deep inelastic electron-proton scattering[20] and neutrino interactions[21] it is known that only about half the momentum of a nucleon is carried by the quarks (partons) in the nucleon.

Using quark momentum wave functions found in lepton-hadron interactions, they allow a quark in one hadron to collide with a quark in the opposite going hadron. The short distance interaction is for quarks to elastically scatter, then move away from the collision region. Because free quarks have never been observed, it is expected that the outgoing high transverse momentum quark will form a jet of hadronic particles. It is the particles in this hadronic jet that the experimenter detects.

Field and Feynman give an algorithm for how this jet forms and predict particle ratios an experimenter should detect[19]. Specifically they make a prediction for the ϕ/π ratio as a function of transverse momentum, which can be observed in our detector. They have developed the model into computer code, using Monte Carlo techniques to calculate results. Figure 4 shows a scattered quark moving away from the interaction region. As it moves away, quark-antiquark pairs are formed in an O-Z-I allowed way. These quarks combine to form mesons. The entire jet production is done in a simple way:

> I.) A random variable function $f(\eta)$ is used and gives the probability that a given part of the quark cascade leaves a fraction of its momentum η to the remaining cascade.
>
> II.) SU(3) is broken in the formation of quark-antiquark pairs. The ratio of the probabilities to form quark-antiquark pairs is:
>
> $$\begin{array}{ccccc} uu & : & dd & : & ss \\ 1 & : & 1 & : & 1/2 \end{array}$$
>
> III.) The spin of the "prompt" mesons are assumed to be vector and pseudoscalar only, with equal probability.
>
> IV.) The transverse momentum given to the quark and antiquark of a pair is $K_\perp$ and $-K_\perp$ respectively. $K_\perp$ is found using a Gaussian distribution with a sigma of 323 MeV/c.

This model will be compared with the data later.

A model of hadron collisions which does not produce particles through a O-Z-I allowed process is the strict thermodynamic model[22]. In this model a fireball is created in the hadronic collision. Because of the strong coupling of hadrons, full thermodynamic equilibrium is attained before the fireball starts to decay. This gives a final state distribution of particles which can only depend on

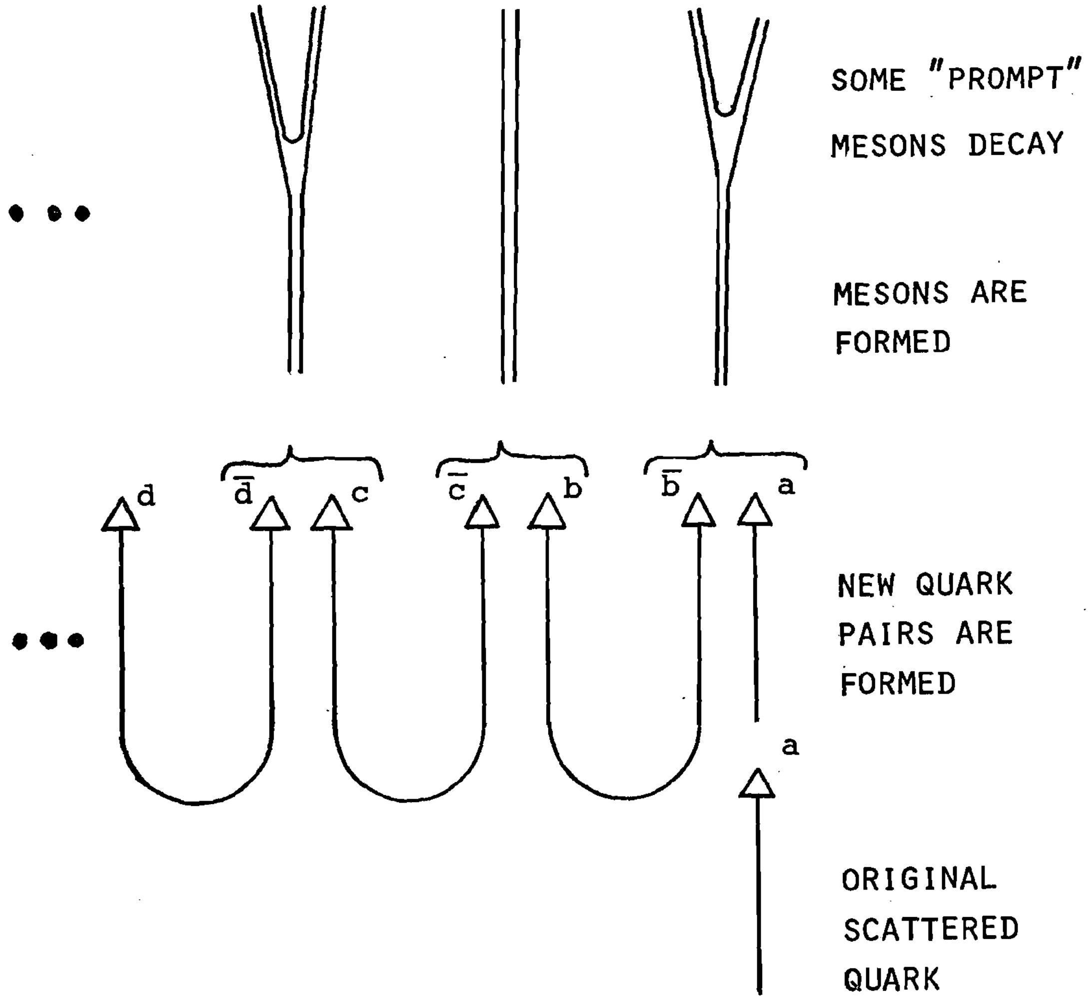

Figure 4. Field and Feynman jet model of particle production. a, b, c, and d are arbitrary quark flavors.

thermodynamic properties. Dynamic properties such as the O-Z-I rule could not matter. The rate and distribution of particle production depends only on the energy of the particle and a coupling constant.

$$\text{rate} \sim \int \text{EXP}\left(\frac{-(p^2c^2 + m^2c^4)^{-1/2}}{T} \right) d^3p \qquad 2.8$$

where T is about 160 MeV. However, it is doubtful that hadronic matter can come to equilibrium in the short time of a collision. With this consideration the model becomes difficult as far as predictive powers. Although there have been attempts to add dynamic effects such as the O-Z-I rule to the thermodynamic model[23], they are done in a somewhat arbitrary way. This model can be used to predict the shape of the ϕ/π ratio but not its level.

The μ to π Ratio

Another decay mode of the ϕ meson is its annihilation through a virtual photon into a pair of charged leptons. This decay means the ϕ will make some contribution to the prompt lepton cross section. The μ/π ratio as a function of transverse momentum has been of great interest because new heavy particle production is expected to have decay products which contain muons. Large transverse momentum muons have an enhanced probability to be the decay products of heavy particles for two reasons.[24] 1.) At large transverse momenta, kinematics no longer favor the production of light hadrons such as π and K mesons. 2.) In high energy collisions light hadrons are so long lived that they can be made to react in a dense material and be absorbed before they can decay weakly into muons. This implies that the large transverse momentum muon data is associated with the production of heavy particles. By understanding how possible known sources contribute to the μ/π ratio, the Drell-Yan process, the Bethe-Heitler process, vector meson production, etc., the remaining unexplained portion can be attributed to new physics.

Before the discovery of the J/Ψ, the ρ, ω , and ϕ mesons were thought to be the main source of prompt muons. But for these particles to account for the μ/π ratio, the ϕ/π ratio would have to be about 3.[25] Our experiment was the first to measure the ϕ/π ratio at large transverse momentum, near $y = 0.0$, and find the ϕ meson's contribution to the μ/π ratio as a function of transverse momentum. The best previous upper limits to the ϕ meson's contribution to the μ/π ratio were set by a Columbia-Fermilab group[26]. Our data shows the ϕ/π ratio to be less than 0.1 and that the ϕ meson's contribution to the μ/π ratio is a factor of $\sim$50 below the total prompt production. Currently, the main contribution to the μ/π ratio at large transverse momentum is believed to be the vector mesons and the direct photon continuum. The contribution due to charmed particle decay is believed to be less than $5 \cdot 10^{-5}$ (27).

Test of Theory

Once the theory of QCD or a similar theory has been fully developed, it will be necessary to test it against experimental results. The new, higher mass, quark states will be able to test the asymptotic freedom limit of the theory. The lower mass quark states containing u, d and s quarks will be important in testing the confining limit of the theory and how quarks combine to form hadrons. Understanding these lower mass states and their production will constitute important tests of any theory of strong interaction.

CHAPTER III

THE APPARATUS

The experiment took place in the Meson Lab at Fermi National Accelerator Laboratory near Batavia, Illinois. The detector consisted of two identical spectrometers, each symmetrically placed on a line which made an angle of 100 milliradians with respect to the beam (Figures 5 and 6). The active elements of a single spectrometer consisted of 3 Cherenkov counters, 16 planes of drift chambers, a hodoscope system and an analyzing magnet. Behind each arm, a muon telescope system was set up to detect muons. Each spectrometer was able to measure the momenta of charged particle trajectories and separate protons, K mesons, π mesons and muons over a wide momentum range. This is sufficient information to reconstruct the particles' four vector. If a massive particle has decay products which are all charged and pass through the spectrometer system, then its four vector can be reconstructed by adding together the measured four vectors of its decay products. This, then, is the purpose of the detector: to measure the four vectors of

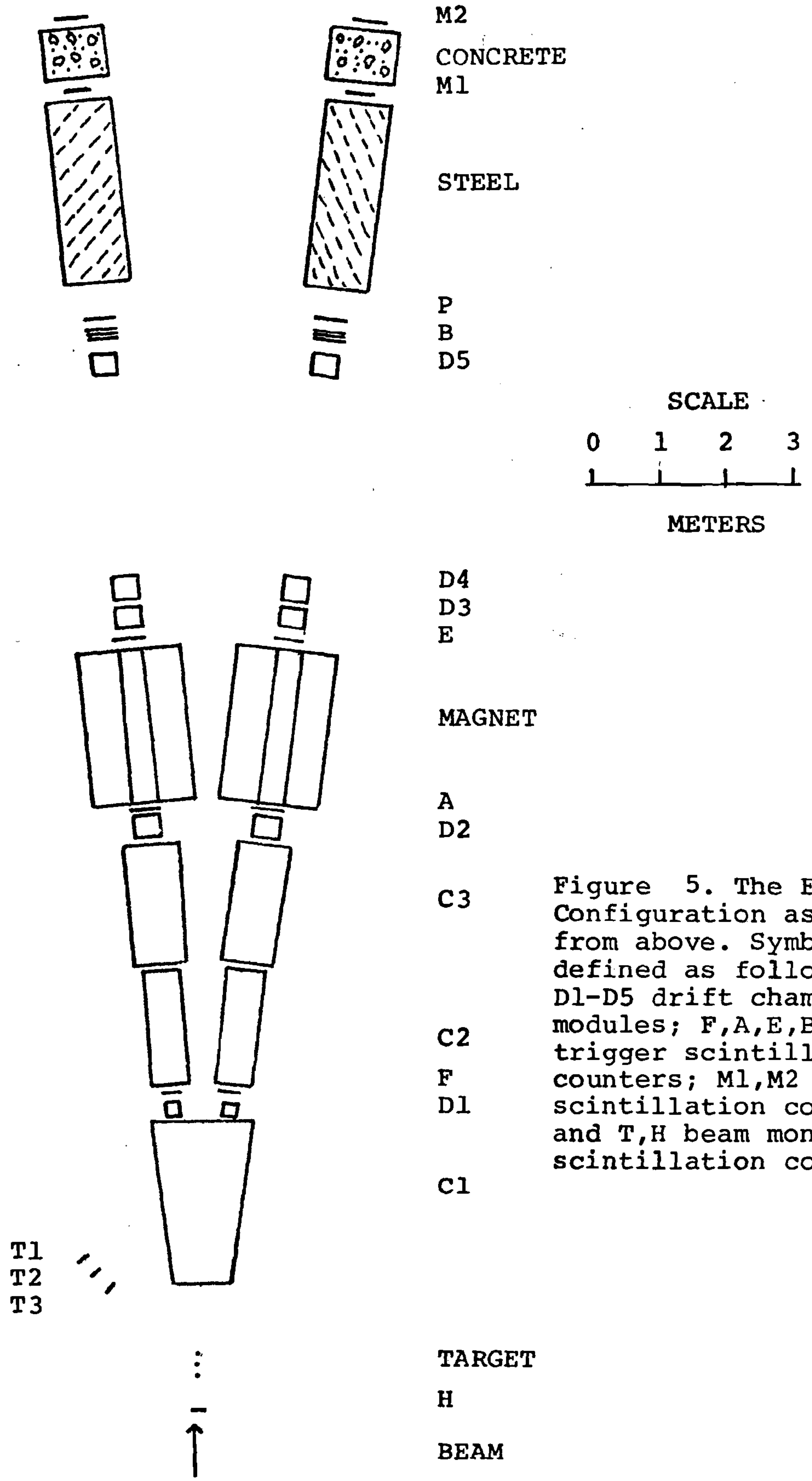

Figure 5. The E-357 Configuration as seen from above. Symbols are defined as follows: D1-D5 drift chamber modules; F,A,E,B,P, trigger scintillation counters; M1,M2 muon scintillation counters; and T,H beam monitor scintillation counters.

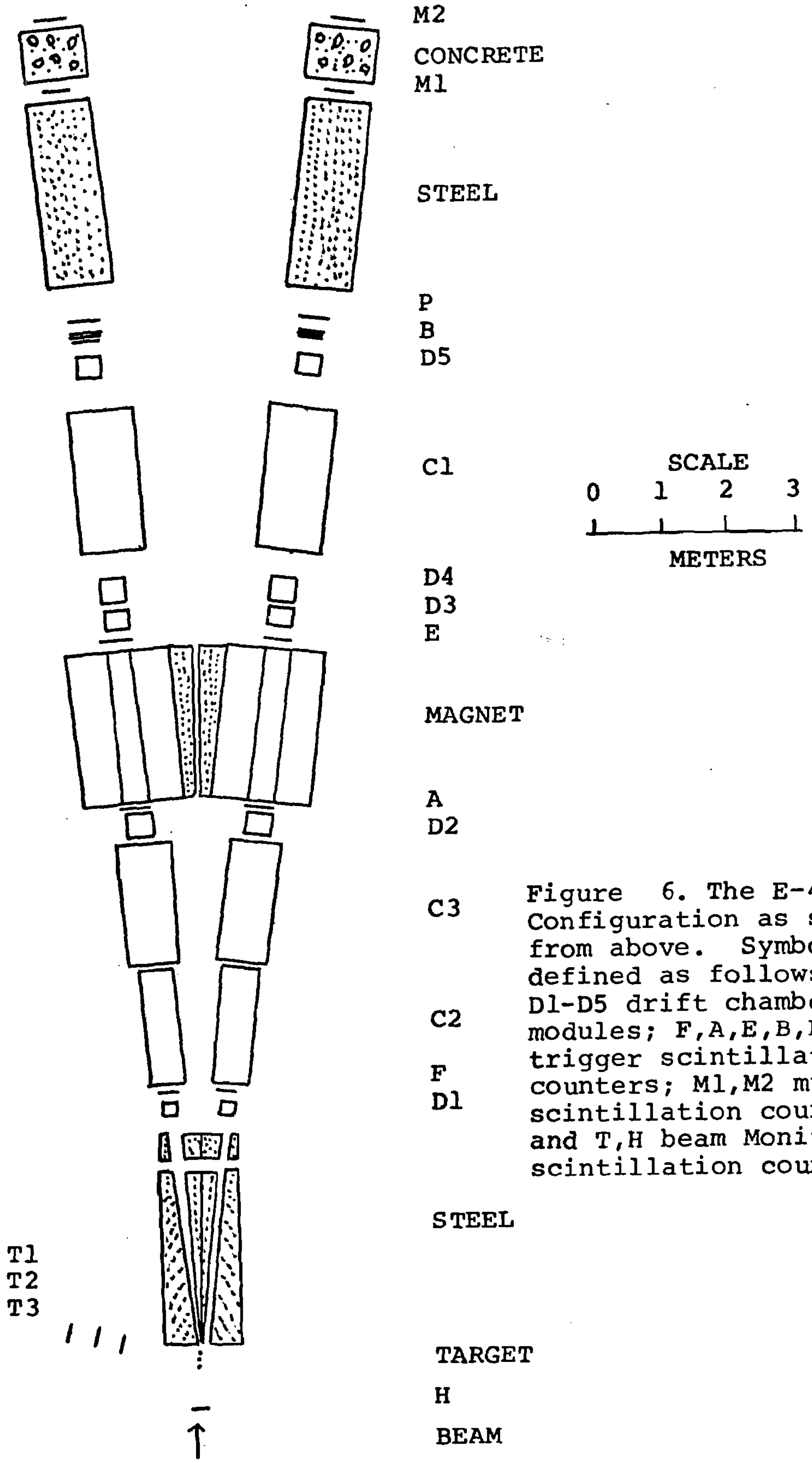

Figure 6. The E-472 Configuration as seen from above. Symbols are defined as follows: D1-D5 drift chamber modules; F,A,E,B,P, trigger scintillation counters; M1,M2 muon scintillation counters; and T,H beam Monitor scintillation counters.

massive states whose charged decay products pass through the detector. More specifically, the spectrometer system was optimally designed to detect the charmed D^o decay into a charged K and π meson. Each spectrometer arm would detect either the π or K meson at high transverse momentum ($\sim$1 GeV/c) from a D^o produced at rest in the center-of-mass of the collision. This detection scheme gave the best signal-to-background ratio for D^o detection because the mass of the D^o was expected to be large ($\sim$2 GeV/c^2), allowing decay products to have a large transverse momentum, while direct production of π and K mesons, a source of backgroud, decreases rapidly with the transverse momentum of the π and K meson. Although the detector was designed for a single particle in each spectrometer arm, clear signals for $K^o_s \to \pi^+\pi^-$, $\Lambda^o \to P\,\pi^-$, $\bar{\Lambda}^o \to \bar{P}\,\pi^+$ and $\phi \to K^+K^-$ were observed in events with two tracks in a single arm.

The Beam and Targets

The beam was a diffracted proton beam taken off the Meson Lab target at 1 milliradian. The beam had an R.F. structure of 18.8 nanoseconds and a spill time of 1 second for 400 GeV/c protons. The beam line consisted of nine quadrupole magnets, two bending strings consisting of dipole magnets, horizontal and vertical pitching magnets (small dipole magnets), horizontal and vertical collimators, and a beam stop. We controlled all the beam elements to bring the beam to a focus at our target and determined the beam size and intensity. The beam size was typically about 0.32 centimeters in diameter at our target. The beam intensities for data-taking ranged from 5 · 10^6 to 5 · 10^7 protons per spill. The beam momentum for all of the single arm running was 400 GeV/c. During the double arm running, the majority of the data was taken with a beam momentum of 400 GeV/c, but there were some data taken at 200 GeV/c and 300 GeV/c. The targets for the single arm running were beryllium. The double arm running had targets of beryllium alone, polyethylene alone and a combination target of beryllium and lead. All the targets were approximately 10% of an interaction length for the beam. Most of the data on the correlation of ϕ mesons to kaons is from a 400 GeV/c beam on a beryllium target.

Beam Calibration

The beam calibration was done using the counters H, T1, T2 and T3 (Figures 5 and 6). The calibration proceeded as follows. The beam was focused and accurately centered on the target. The beam was then counted at different beam rates using the H counter, which was in the beam, and the T counters, which formed a telescope viewing only the target and were not in the beam. A plot of the number of counts in the T counter coincidence per number of counts in the H counter, versus the number of counts in the H counter, for various beam rates, was made. The calibration value was the extrapolation of the plot to zero beam rate. This extrapolation eliminated the loss of counts due to voltage drops in the H phototube during the beam spill and the effects of more than one beam particle passing through the H counter at a time. The calibration value was 2000 counts in the T coincidence for every 10^8 particles on target. The accuracy of the calibration was 10% to 15%.

Two Detector Configurations

The detector existed in two major configurations. All the single arm ϕ meson data and much of the double arm correlation data come from the E-472 configuration. This configuration is shown in Figure 6. In this configuration, the detector had a 2.74 meter block of steel immediately following the target, with three channels cut in it. One channel was in the center to allow the beam to pass cleanly through and two others were centered at angles of 100 milliradians on either side of the beam to allow particles moving in the direction of the spectrometer arms to pass through unobstructed. The other particles in the interaction would then interact in the shielding and be absorbed, except for muons with energies above 3.5 GeV/c, which would pass through the steel. 2.3 meters of steel shielding with a channel to pass the beam were also placed between the two analyzing magnets. The original purpose of the steel was to filter hadrons and demand muons in the trigger to search for associated production of charmed particles. The shielding had the effect of lowering the number of random hits in the other spectrometer elements as compared to the original E-357 configuration. In the E-357 configuration, there was no shielding (Figure 5). The region downstream of the target was taken up by a segmented Cherenkov counter which was later displaced by the shielding in E-472. The task of this forward Cherenkov counter was taken over by placing a Cherenkov counter behind each analyzing magnet. The other elements of the spectrometer system were identical in both configurations.

Cherenkov Counters

Each spectrometer arm had three threshold Cherenkov counters to separate protons, K mesons and π mesons in the momentum range from 7 GeV/c to 20 GeV/c. The counters contained:

C1 - Air at 1 atmosphere of pressure
C2 - Propane at 1.8 atmospheres of pressure
C3 - Carbon dioxide at 1.4 atmospheres of pressure

The Cherenkov counters had high efficiencies, above 97%, except the C1 counters used to count π mesons in the E-472 configuration. Table 2 gives the Cherenkov counter parameters. The problem with these C1 counters was that their efficiency depended on the momentum of the particle and the position at which the particle hit the mirror in the counter. Figure 7 shows the efficiency versus the mirror position for negative pions. To study the efficiency, the counters were divided into horizontal bands of 4 inch widths at the mirror (the efficiency difference for vertical bands

CHERENKOV COUNTERS

Cherenkov Counter	Threshold Proton	Threshold Kaon	Threshold Pion	Efficiency	Number of Photo Electrons	Counter Length
C1-357	39.0	20.5*	5.8*	97%	12 ± 2	2.16
C2	13.7*	7.1*	2.0	99%	23 ± 5	1.52
C3	24.7	13.0*	3.7	98%	11 ± 2	1.73
C1-472	39.0	20.5	5.8*	85%	11 ± 2	2.64

Table 2. * indicates a threshold value which was measured. Other values were found using the equation:

$$\frac{P'_o}{m'} = \frac{P_o}{m} \qquad 3.1$$

P_o is the threshold momentum for a particle of mass m. P' is the derived threshold for a particle of mass m'. The average number of photoelectrons and threshold values were found by fitting the threshold curves to the form: (28)

$$1 - \mathrm{EXP}(\ n\ (\ 1 - (P_o/P)^2)\ ) \qquad 3.2$$

n is the average number of photoelectrons and P is the momentum of the particle. The threshold values are accurate to ± 100 MeV/c. All counters were filled with air to measure their efficiency. Any two counters were used to check the efficiency of the third. Counter lengths are in meters.

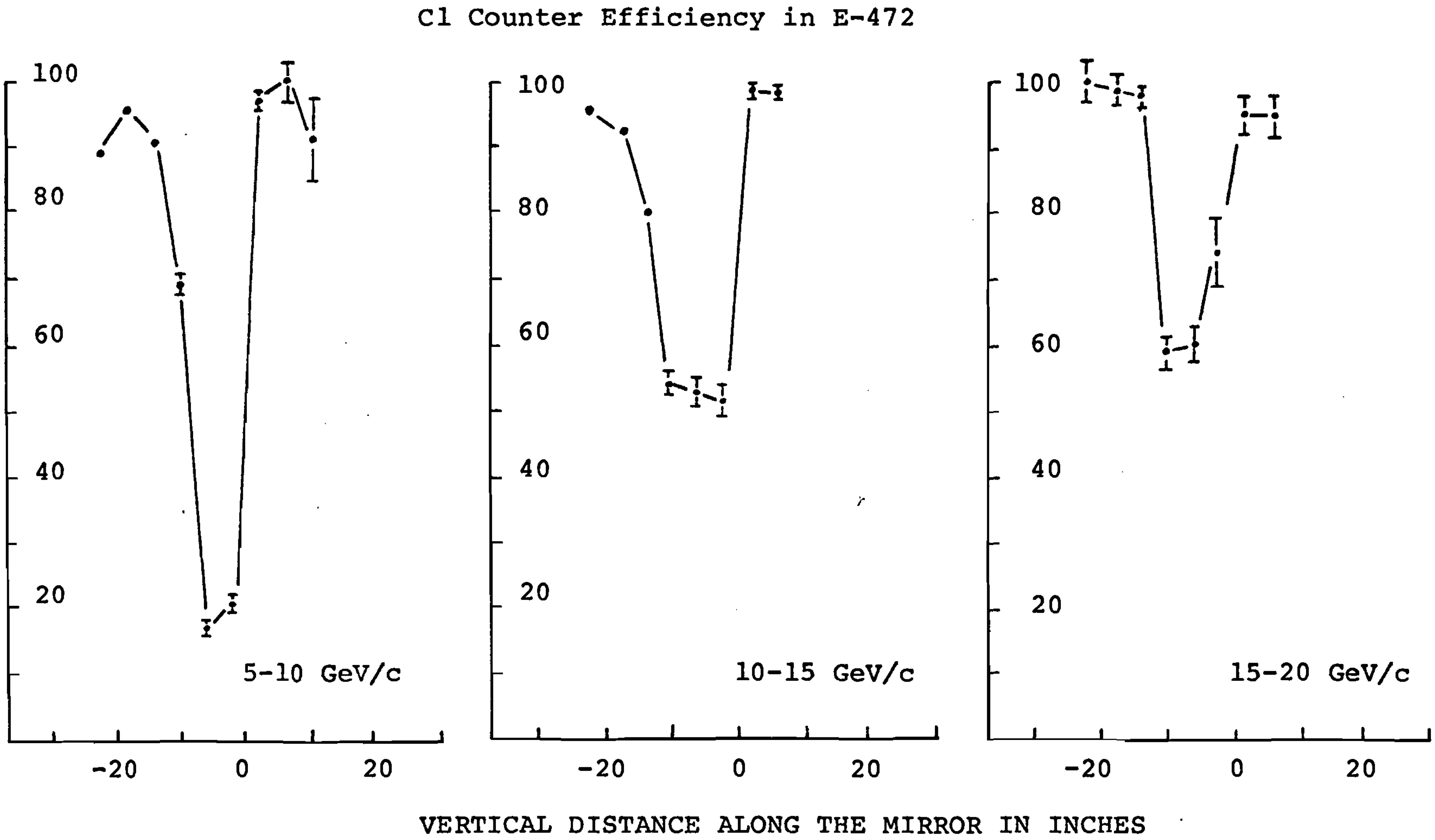

Figure 7. The C1 counter efficiency in the E-472 configuration as a function of distance along the mirror in 5 GeV/c intervals.

was found to be small). The counter efficiency in each band was determined as a function of momentum using events with air in all three Cherenkov counters. The efficiency as a function of momentum and mirror location was parameterized using the data in Figure 7 and a linear interpolation method. Fortunately, most of the particle flux was in the areas of high efficiency so that the average efficiency of the two counters was ~85%.

Phototubes and The Hodoscope System

Most of the counters in our experiment used RCA 8575 phototubes. The 10% to 90% rise time was 2.4 nanoseconds with a half-width output pulse of 10 nanoseconds. Clip lines were added to all the phototube outputs and the final output was a 90 millivolt pulse with a half-width of 6 to 7 nanoseconds. The output from the phototubes went into a LeCroy LRS 621 discriminator set to a 30 millivolt threshold. All timing was done to the 1 nanosecond level by graphing the time correlation of phototube pluses. the maximum rate capabilities of the phototubes in our experiment were 5 megahertz.

The hodoscope system is shown in Figure 8. The effect of the hodoscope is to limit the acceptance of low momentum particles. The effect for single particles passing through a spectrometer arm is shown in Figure 9. As can be seen, its purpose was to accept single particles with a transverse momentum above 1 GeV/c. The acceptance drops rapidly for

SCINTILLATION COUNTER HODOSCOPE SYSTEM

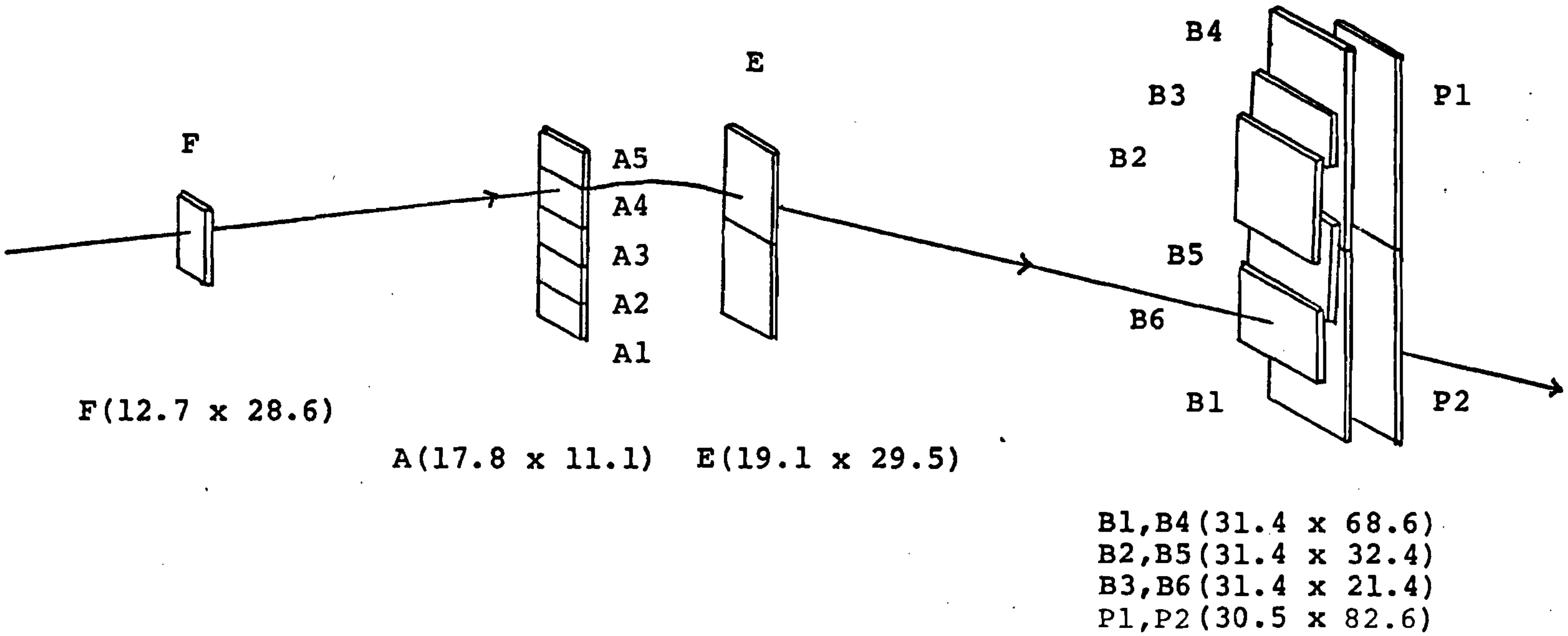

Figure 8. This is a view of the trigger scintillation counters in a single spectrometer arm. The figure is not to scale. All counter sizes are in centimeters. A, E and P sizes are for a single counter. All counters are 0.32 centimeters thick. Although there are two counters in the group labeled E, their outputs were always logically OR-ed and are labeled as a single counter. The distance of each counter group from the target is: (F) 3.91 meters, (A) 8.01 meters, (E) 10.45 meters, (B2,B6) 14.70 meters, (B3,B5) 14.71 meters (B1,B4) 14.88 meters, (P) 14.96 meters. The figure also shows the trajectory of a negative particle that would cause an event trigger.

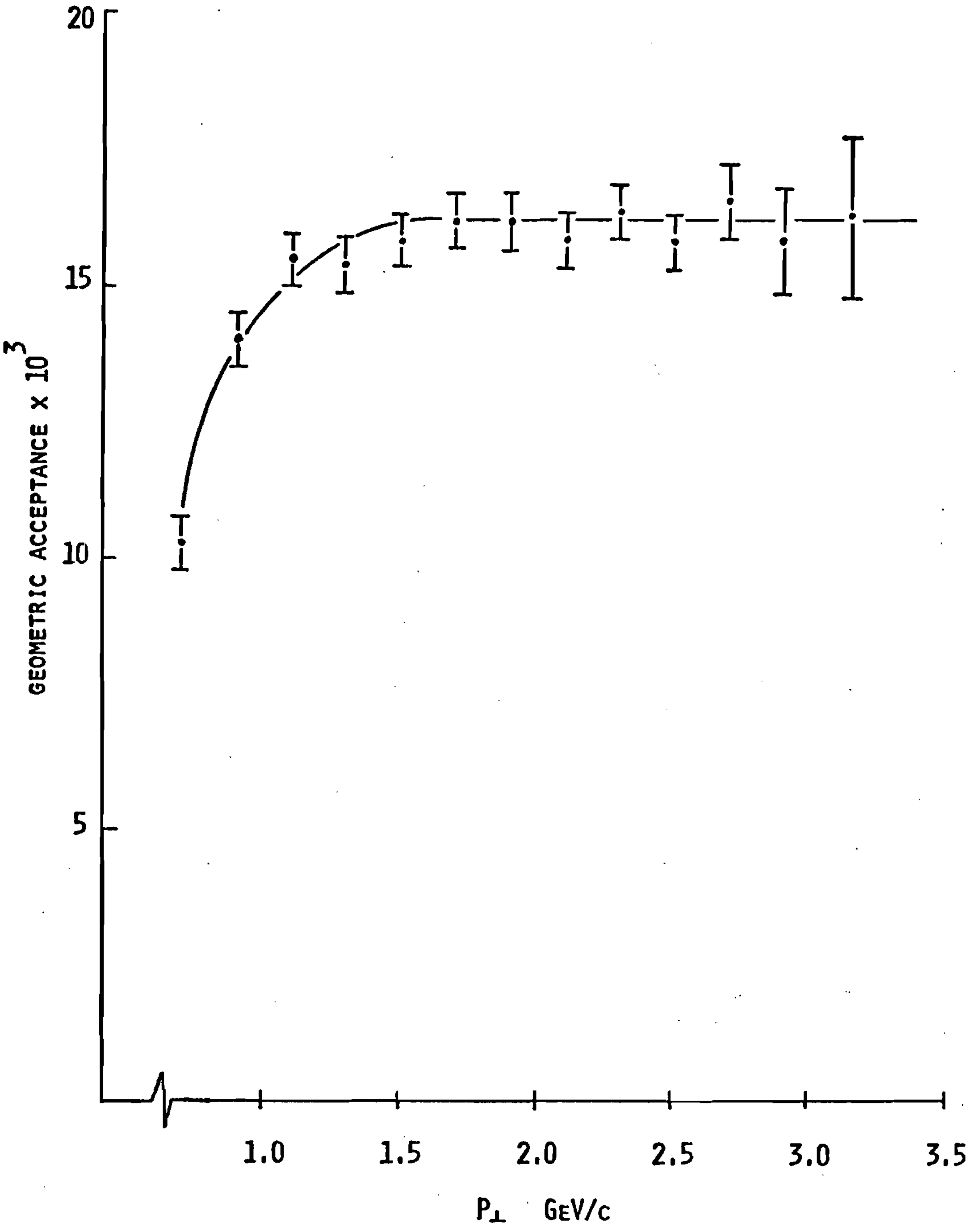

Figure 9. Single particle (π^-) geometric acceptance as a function of transverse momentum.

particles with a transverse momentum less than 1 GeV/c and is flat for particles greater than 1 GeV/c. In reality, extra hits in the hodoscope system can cause particles with a lower momentum to be accepted in the trigger, but these can be cut from the data by using the drift chamber information to check which hodoscope counters the particle hit and requiring these counters to form a trigger.

A simplified schematic diagram of the fast electronics and triggering logic is shown in Figure 10. All the discriminator units, coincidence units, fan-outs, time-to-digital converters (TDC's), analog-to-digital converters (ADC's), scalers and latch units used in the experiment were standard NIM modules manufactured by EG&G or LeCroy. Not shown in the logic diagram are the scalers used to monitor certain counters and various coincidences in order to check that the logic and hodoscope system was working properly.

The normal single arm trigger consisted of:

$$XL \text{ or } XR = F\cdot\{A\}\cdot E\cdot\{B\}\cdot(P1 \text{ or } P2) \qquad 3.3$$

where { } stands for the appropriate "A" and "B" combinations (Figure 10). A '•' means logical AND. The trigger would be an XL if the counters in the left arm formed a correct coincidence or an XR if the coincidence was formed in the right arm. The XL and XR triggers were used to take single arm inclusive pion data. The single arm inclusive ϕ meson data were taken with a "ϕ" trigger:

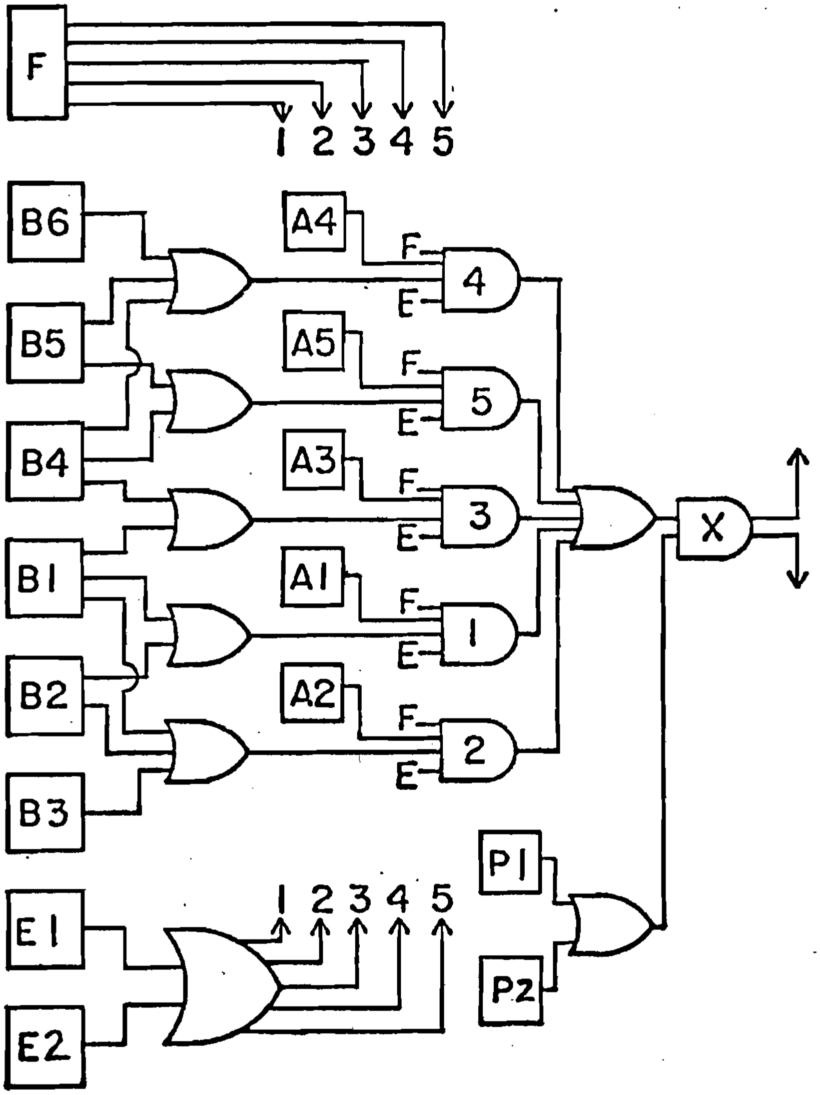

Figure 10. A simplified diagram of the trigger logic for a single spectrometer arm. Here X represents XL or XR. Squares represent discriminators. P1 and P2 are shown as logically OR-ed. In the ϕ-trigger they were logically AND-ed.

$$\text{"}\phi\text{ trigger"} = F\cdot\{A\geq 2\}\cdot E\cdot\{B\}\cdot P1\cdot P2 \qquad 3.4$$

The ϕ trigger enhanced the recording of ϕ events by demanding two particles in a single spectrometer arm. This was accomplished by demanding two or more A counters to fire and both P counters to fire. The ϕ trigger also demanded that the Cherenkov counters' response be consistent with that of a K meson.

The double arm data were taken with a "hadron" trigger which required XL and XR.

$$\text{Hadron} = XL\cdot XR \qquad 3.5$$

This required at least one particle in each spectrometer arm. The hadron trigger was often modified to include specific Cherenkov responses in order to enhance certain particle types. In those cases, we were attempting to eliminate events with a π meson in both spectrometer arms and enhance the recording of events with K mesons.

Drift Chambers

Drift chambers were used in this experiment to locate trajectories of particles after the hodoscope system gave the proper trigger. Each spectrometer arm had 184 drift cells. Each cell consisted of one sense wire and a group of field shaping wires. The field shaping wires were spaced 0.51 centimeters apart and had a voltage distribution which gave a voltage gradient of 670 volts per centimeter in the drift region. The sense wires were at ground, in the center of the cell. When a charged particle passes through the cell, the primary electrons produced in the gas by the particle move towards the sense wire. Near the wire, the field becomes strong enough that the drifting electrons cause an electron avalanche, producing a signal on the sense wire.

The sense wire signal was carried to a LeCroy LD 603 hybrid circuit chip mounted on the chamber module. The output of the chip was transmitted by cable to a LeCroy model 2228 octal TDC. The TDC was started by a trigger and stopped by the output signal from the drift cell. In this mode, only one pulse per cell per event could be recorded. If more than one track went through the same cell in the same event, only the one closest to the sense wire would be recorded. The TDC information was read by a PDP-11 on-line computer through a Camac interface, stripped of all overflow TDC information, and written on a 800 BPI magnetic tape.

The cells were of three sizes: 2.03 centimeters, 3.05 centimters and 6.10 centimeters. A row of the same size cells made up a drift chamber plane. The planes had three orientations: horizontal, vertical and tilted at an angle of $\theta = \tan^{-1}(1/4)$ with respect to the vertical. Each plane was associated with another plane of its same orientation, and having the same cell size, but having its sense wires shifted half a cell's length. By matching hits on the two planes, the left-right ambiguity problem was solved.

Being able to calculate the time at which the particle passed through the drift chamber and knowing the TDC stop time, the difference, the drift time, was measured. The spatial distance of the track from the wire could then be found by converting the drift time to a distance using our time-to-space calibration.

The drift cell calibration was done off-line. The calibration was found by generating the normalized time distribution f(t) for all the cells of a given size:

$$f(t) = 1/N * N(t) \tag{3.6}$$

Here N is the total number of counts observed and N(t) is the number of counts observed at time t. f(t) is then the probability to observe an event at time t. It was then assumed that the particle flux, originating in the target, uniformly illuminated any cell. In our experiment, the cell sizes were small enough that this condition was approximately satisfied. This assumption yields the following conditions:

$$df(t)/dx = c \tag{3.7}$$

$$df(t)/dt * dt/dx = c \tag{3.8}$$

where c is a constant. The path length x(t) corresponding to a drift time t is then given by the simple form:

$$F(t) = \int_0^t df(t) = c\int_0^t v(t)\ dt = x(t)/D \qquad 3.9$$

Here D is the total drift space or half a cell's width, and v(t) is the velocity of the drifting electrons. F(t) was fit to a third order polynomial in t. Figure 11 shows the time-to-space conversion for all three cell types. This simple method yielded a resolution sigma of 250 microns, with only four constants for each of the three different cell sizes or twelve constants in all for 368 individual drift cells. Higher resolution was unnecessary because the mass resolution was already dominated by the multiple scattering of the particles as they passed through the spectrometer system. This method was checked using both direct measurements of the time-to-space relationship and another off-line calibration method. The agreement between all three methods was excellent. A more detailed description of the drift chamber system used in the experiment can be found in reference (29).

Analyzing Magnets

The experiment used two BM-109 analyzing magnets, one in each spectrometer arm. The dimensions of the magnet apertures were 20.3 centimeters by 61.0 centimeters and were enclosed in an iron yoke 182.9 centimeters long. The maximum field developed by these magnets is 18 kilogauss with an effective length of 1.88 meters. The field integral $\int B * dl$ and effective length were measured using a flip

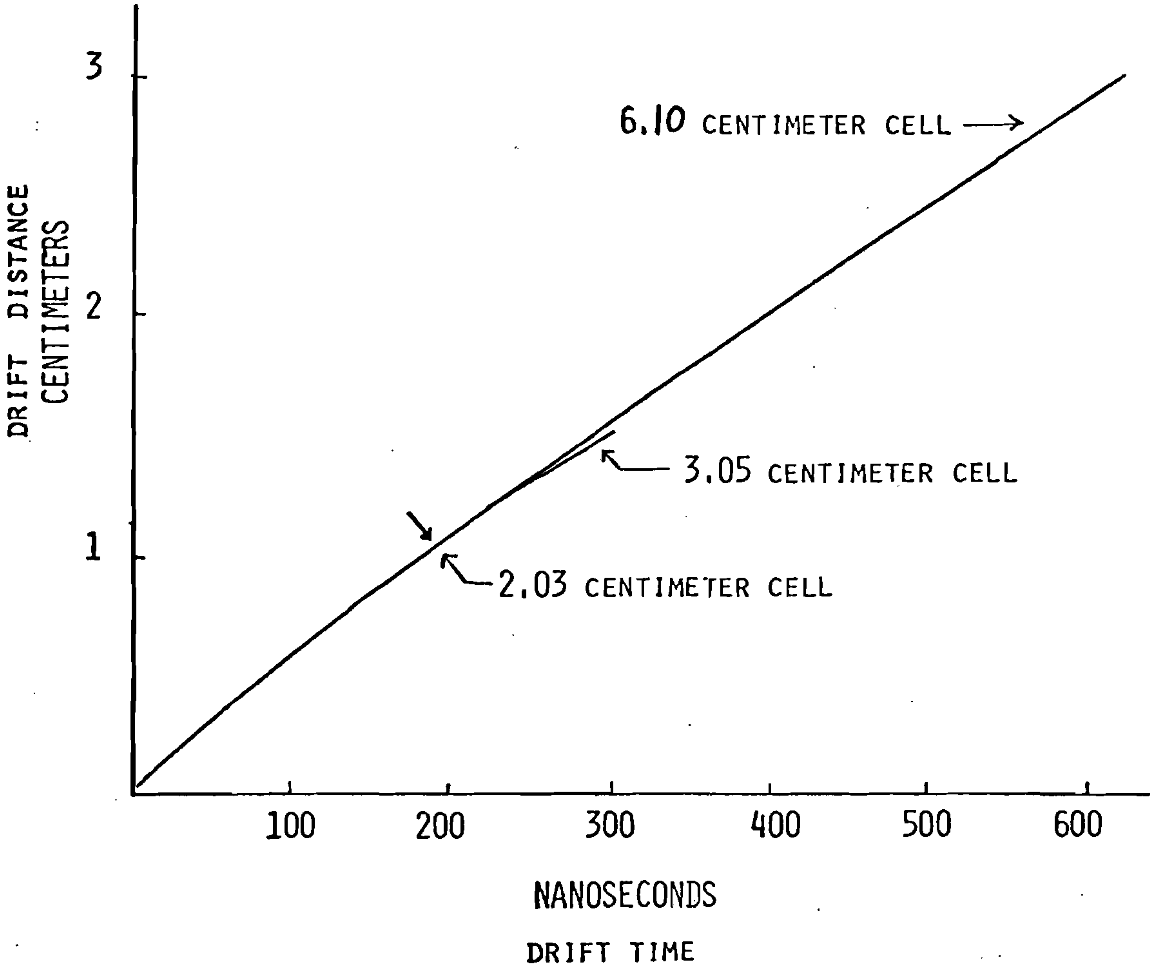

Figure 11. The time-to-space conversion for the three cell types used in this experiment.

DRIFT CHAMBER SYSTEM

Plane Number	Drift Box	Number of Cells	Cell Size	Wire Orientation	Plane Efficiency
1	1	11	3.05	Horizontal	.974
2	1	10	3.05	Horizontal	.971
3	1	8	2.03	Vertical	.971
4	1	7	2.03	Vertical	.962
5	2	9	6.10	Horizontal	.977
6	2	10	6.10	Horizontal	.980
7	2	10	2.03	Vertical	.993
8	2	9	2.03	Vertical	.994
9	3	12	6.10	Tilted	.987
10	3	11	6.10	Tilted	.990
11	4	11	6.10	Horizontal	.976
12	4	10	6.10	Horizontal	.975
13	4	10	2.03	Vertical	.995
14	4	11	2.03	Vertical	.993
15	5	23	6.10	Horizontal	.983
16	5	22	6.10	Horizontal	.983

Table 3. This table gives information for a single spectrometer arm. The spectrometer system is symmetric so the information applies to both arms. The efficiencies are those found during the E-472 running period and are typical values. The cell sizes are in centimeters.

coil and a nuclear magnetic moment resonance probe. These values were used in the tracking program.

In the tracking program and all analysis programs, the field was assumed to be uniform over its effective length and particle trajectories were assumed affected only in the plane perpendicular to the field. Other effects, such as fringe fields and focusing, were found to be small and negligible. The momentum was then found by using the equation:

$$\frac{P \times B}{|B|} = \frac{|q| \int B \, dl}{\sin \theta_{out} - \sin \theta_{in}} \qquad 3.10$$

where a negatively charged particle gave a negative value and a positively charged particle gave a positive value. θ_{in} and θ_{out} are the projected angles in the bending view a particle makes entering and exiting the field.

The current passing through each magnet was monitored by a digital volt meter (DVM) which measured the voltage required to null the flux in a magnetic circuit surrounding one of the power supply busses. Variations in this voltage were recorded along with the data and the particles's momentum was corrected off-line for changes in the field about the nominal value. Changes in the DVM value of more than 0.1% caused the on-line computer to cease data-taking. The final field integral values used in the analysis were found by adjusting a momentum multiplier until the measured K_s^o mass observed in a single spectrometer arm, in its $\pi^+ \pi^-$ decay mode, coincided with its present world average. Typical corrections at this stage were always less than 3%. The actual field values and correction factors used in the analysis are listed in Table 4.

Data Acquisition

The experiment was monitored by a PDP-11 computer with 80k of 16 bit memory. Peripherals included two Digital Equipment Corporation 800 BPI 9 track tape drives, a teletype, two disk drives, and a Tektronix display terminal. The computer was Camac-interfaced to the fast electronics used in the experiment.

Upon receipt of a start signal from the trigger logic, the TDCs would run to completion and generate a computer interrupt. The computer then proceeded into its programmed routine of data acquisition. A gate was generated to stop further event triggers and to stop certain scalers, until the computer was finished processing the particular event. The computer would read in the latch information for all the counters, the drift chamber TDC information, and the Cherenkov counters ADC information. Information on power supplies, DVM readings and TDC calibrations was periodically read and recorded.

The PDP-11 computer was limited by its speed to taking about 180 events per second. The beam was run at a rate necessary to saturate the computer. While the computer was reading in data, the trigger was stopped. This dead time

Magnet Fields

Nominal Fraction of Full Field	Field Integral		Momentum Correction	
	L	R	L	R
100%	33.30	32.46	0.996	1.012
72%	23.98	23.37	0.994	1.027
50%	17.16	16.33	0.997	1.021

Table 4. This table gives the field integrals in units of kilogauss-meters. The momentum corrections were found by calibrating on the K-zero short mass, observed in a single spectrometer arm.

amounted to 60% of the time for the double arm spectrometer and 90% of the time for the single arm trigger. Data was written on a magnetic tape and normally contained ∿50,000 triggers. A full tape constituted a run. A run took about two hours, after which all scaler information, including beam flux information, was hand-written on a run summary sheet.

In addition to the task of data acquisition, the computer monitored the power supplies, DVM and TDCs and printed messages when it detected anomalous conditions. There was also an on-line tracking program and many interactive diagnostic programs the experimenter could use to monitor the experiment's performance.

CHAPTER IV

ANALYSIS

In the course of E-357 and E-472, we wrote about $5 \cdot 10^7$ event triggers on magnetic tape. Each event contained about $2 \cdot 10^3$ bits of information. To render this 10^{11} bits of information useable, a distillation process was necessary. The data tapes were presented to a tracking program which wrote summary tapes. A summary tape contained the tracking output of 10 to 15 full data tapes. The summary tapes were then searched for specific information, which was written on an analysis tape. In most cases, the information for an analysis could be contained on one magnetic tape. The analysis tape along with corrections to the data would then be used to generate the final results for a particular analysis.

Tracking Program

The tracking program took the drift chamber TDC information and converted it to track information. The program first searched for matched hits on all pairs of drift planes. If a hit could not be matched, it was still used but had two possible locations because of the left-right ambiguity problem. Each view, bending view and non-bending view, was searched for tracks separately. They were later joined together using the tilted or stereo chamber. The bending view had two pairs of chambers in front of a magnet and two pairs behind a magnet. The non-bending view had two pairs of chambers in front of a magnet and only one pair behind a magnet. The tilted chamber was behind each magnet.

In both views, the search for tracks began behind the magnets, where the number of random hits in the chambers was much lower than for the chambers in front of the magnet. In the bending view, all possible lines were formed between the two pairs of planes behind a magnet. A line had to have at least three hits out of a possible four. The points of intersection of these lines with a plane at the center of the magnetic field was found. A line was then drawn from each intersection point to the center of the target. Within a certain distance of these lines, hits in the front chambers were searched for. Both pairs of chambers in the front bending view had to have at least one hit to form a line. Once a line was found, its intersection with the magnet center plane was found. Two lines formed a particle trajectory in the bending view if the intersection points at the magnet's center plane of a line in front and a line behind the magnet were within 0.760 centimeters of one another. If two or more lines behind the magnet matched a single line in front of the magnet, the one with the best match at the magnet center formed the trajectory.

In the non-bending view, lines were drawn to the target using first, matched pairs in the chamber behind the magnet, then using matched pairs in front of the magnet.
Hits were searched for along one line at a time. A trajectory was formed if at least four out of six possible hits were found. In this view, each pair of planes had to have at least one hit.

To have a track output to the summary tape, the two views had to be consistent with the coordinate information of a matched pair or of one hit in the tilted chamber.

The data consisted of four event types:

I. One track in one spectrometer arm. No track in the other.

II. Two tracks in one spectrometer arm. No track in the other.

III. One track in each spectrometer arm.

IV. Two tracks in one arm and one track in opposite.

Types I and II are called single arm events, while types III and IV are called double arm events.

Target Cuts

Target cuts were applied to the data to assure that the events of interest originated in the target and in the case of more than one track per event assured that the tracks originated from the same beam-target interaction.

Each cut began by finding the point of closest approach on each of the two tracks. In the case of single track events, the beam line, as determined from double arm data was used as one of the tracks. The distance between these points, the distance of closest approach, was restricted ($\sim$0.75 centimeters) depending on the type of event. The vertex or interaction point of the two tracks was defined to be the point midway between the two closest approach points. The interaction point was restricted to be in the target region (Figure 13). Events with three tracks were handled slightly differently because three interaction points were involved (Figure 12). The half-width resolution obtainable using tracks in opposite arms was 1.0 centimeter along the beam and 0.1 centimeters perpendicular to the beam. The half-width resolution for tracks in the same arm was 4.5 centimeters along the beam and 0.7 centimeters perpendicular to the beam.

Figure 13 shows target distributions found for double arm events.

Particle Identification

A single track in a spectrometer arm could be unambiguously identified as a pion or a kaon over the momentum range 7.1 GeV/c to 19.9 GeV/c. To be identified as a pion all three Cherenkov counters were required to give a response. To be identified as a kaon in the range 7.1 GeV/c to 13.5 GeV/c, only C2 could respond. In the range 13.5 GeV/c to 19.9 GeV/c, both C2 and C3 had to respond and not C1. Using these Cherenkov responses, the probablility

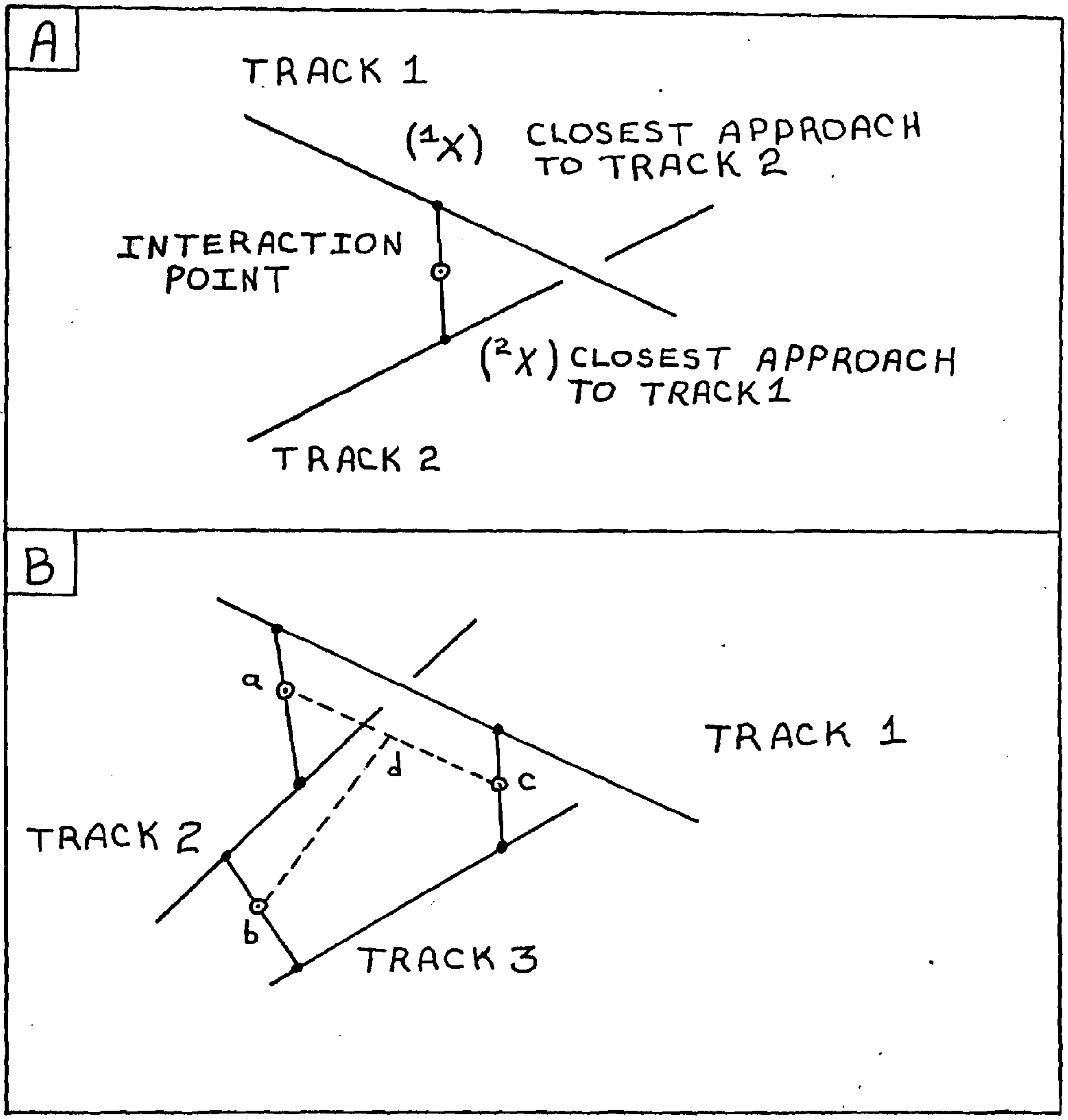

Figure 12. A.) Shows the interaction point formed midway between the distance of closest approach of two tracks. B.) Shows a 3 track event in which tracks 2 and 3 are in a single spectrometer arm. Track 1 is in the opposite arm. a, b, and c are the interaction points. Because of the good resolution obtainable for tracks in opposite arms a strong cut is applied to their interaction point. A weaker cut is applied to the same side interaction point.

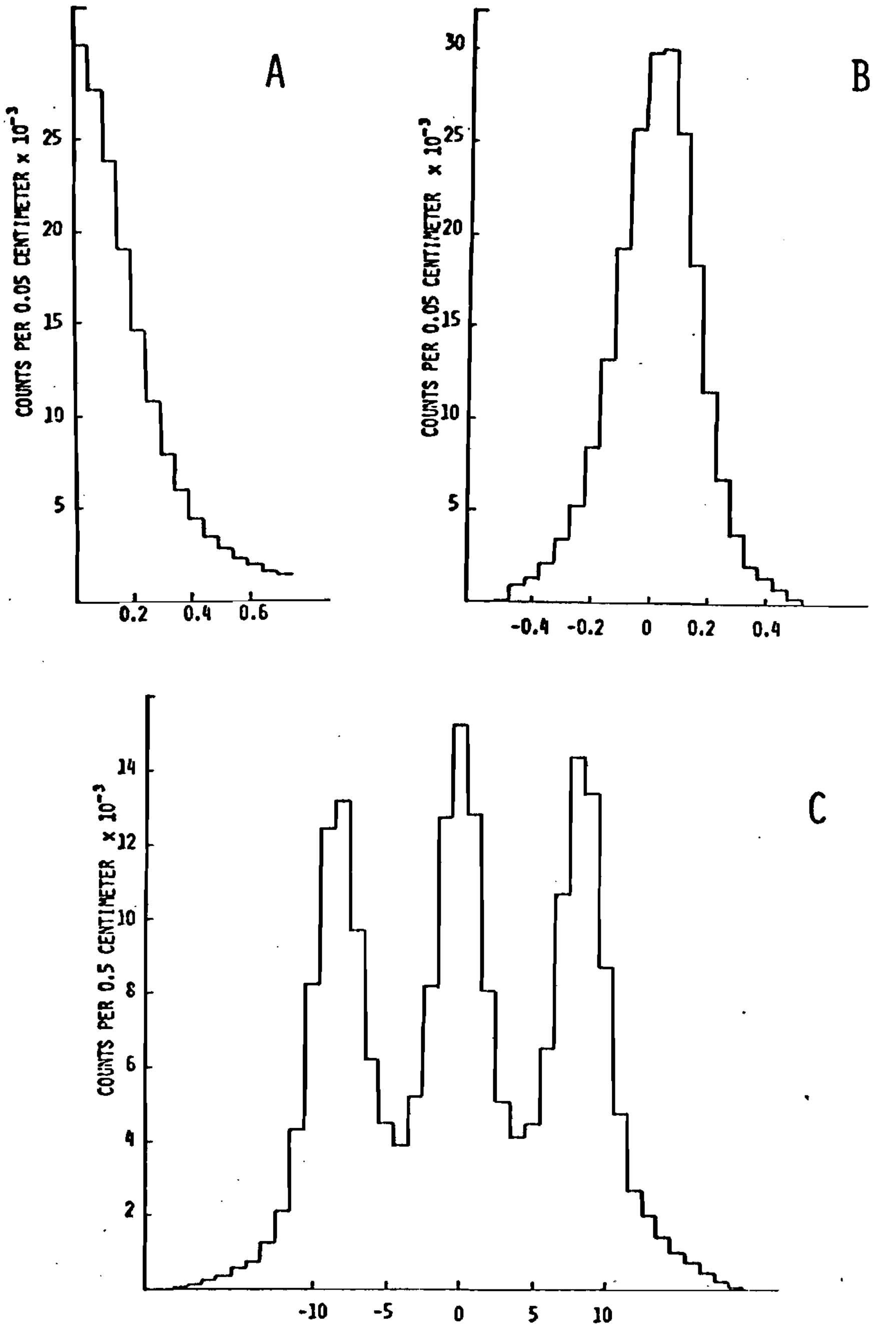

Figure 13. Target distributions after target cuts for tracks in opposite spectrometer arms. A.) The distance of closest approach of two tracks. B.) The interaction point perpendicular to the beam. C.) The interaction point parallel to the beam, showing the three element beryllium target. All units are in centimeters.

that an identification was correct in E-472 was 99% for π mesons, 91% for K mesons with a momentum below 13.5 GeV/c, and 70% for K mesons above 13.5 GeV/c. The poor separation for the higher momentum K mesons was due largely to the inefficiency of the C1 counter which allowed the π mesons to contaminate the K mesons. Even so, the average probability that a particle identified as a K meson was a K meson is 85%.

ϕ Meson Identification

Using the event summary information, a sample of ϕ mesons can be generated by choosing only those events, with two tracks in a single arm, which are consistent with being a K^+K^- pair. To be consistent, the following conditions had to be satisfied:

I. The tracks had to be of opposite charge.

II. The event had to pass the appropriate target cuts.

III. The Cherenkov counters must give a response consistent with the highest momentum track being a kaon. Table 5 gives the momentum versus Cherenkov responses for the highest momentum track. The momentum overlap of the Cherenkov regions in Table 5 was allowed in order to avoid any loss of ϕ signal due to threshold inefficiencies. The small background this created was subtracted out.

IV. The trajectories of the K^+K^- pair through the hodoscope system were checked to assure that the pair caused the trigger and not random hits in the hodoscope system. This off-line trigger requirement caused a 5.3% loss of ϕ signal. More than simplifying the acceptance corrections, it was felt that

Accepted Cherenkov Counter
Responses to a K^+K^- pair

Highest Momentum Track	Cherenkov Counter Response C1	C2	C3
0.0 to 7.5 GeV/c	0	0	0
7.0 to 14.1 GeV/c	0	1	0
13.0 to 20.5 GeV/c	0	1	1

Table 5. The Cherenkov counter responses to a pair of kaons. "0" means the counter gives no response. "1" means the counter gives a response. The overlapping momentum regions assure that no K^+K^- pairs are lost in the Cherenkov counters threshold regions.

> this small loss was preferable to trying to understand the frequency of random hits, and any correlations they may have with a variable of interest.

The Monte Carlo Model

To generate final results, corrections to the data had to be made. Many of these corrections were found using a computer model of the spectrometer system incorporating Monte Carlo techniques. Corrections to the data for geometric acceptances, particle decay in flight, finite drift cell size, drift chamber efficiency, Cherenkov counter efficiency, resolution and random noise accompanying the event were all found using Monte Carlo techniques. The physical size, material composition and response of each element of the spectrometer were included. The sizes and location of all the elements of the spectrometer were accurately measured and recorded during the construction phase of the spectrometer. The geometric apertures of the spectrometers were determined at each trigger counter by using events with more than one track in one of the spectrometer arms. This allowed one track to trigger the system while the other was allowed the full range of the apertures.

The trajectory of a prompt particle was determined using the three independent random variables:

I. $P_\perp$, the transverse momentum.

II. y, the rapidity, defined as:

$$y = 1/2 \cdot \ln((E + P_{\parallel})/(E - P_{\parallel})) \qquad 4.5$$

where E is the particle's energy and $P_{\parallel}$ is the particle's momentum parallel to the beam.

III. The azimuth angle.

The distribution of particles in azimuth was assumed to be flat. The distribution of particles over our limited rapidity range of 0.25 units centered near $y = -0.4$ was also assumed to be flat. The distribution of particles in transverse momentum was assumed to be:

$$P_{\perp} \cdot \mathrm{EXP}\ (-\alpha \cdot P_{\perp}) \qquad 4.6$$

The slope parameter, α, was found using experimental data. All particle decay distributions, such as ϕ decaying to K^+K^-, and K meson decay to $\mu\nu$, were assumed to be uniform in the center of mass of the decaying system. The corrections and results found using the Monte Carlo model of the spectrometer arm are discussed in the next chapter.

CHAPTER V

THE RESULTS

In this chapter, this experiment's results are presented on the production of ϕ mesons in proton-nucleus collisons. The corrections used to obtain these results and the errors in the results will be discussed. The results will also be compared to other experiments and theoretical models where possible.

Mass and Width of the ϕ Meson

A measurement of the mass and width of the ϕ meson was made using a sample containing 1300 ϕ meson events collected using the single arm, ϕ -trigger mode (Figure 1). The mass and full width of the ϕ were found to be:

$$\begin{aligned} M_\phi &= 1.0197 \pm 0.0002 \ \mathrm{GeV}/c^2 \\ \Gamma_\phi &= 0.0045 \pm 0.0004 \ \mathrm{GeV}/c^2 \end{aligned} \tag{5.1}$$

To obtain these results it was necessary to 1.) calibrate the mass scale, 2.) correct the data for geometric acceptance as a function of mass, 3.) find the mass resolution in the ϕ mass region, 4.) fit the data and 5.) evaluate the systematic and statistical errors. These corrections and errors are now discussed.

The field integral of each magnet was calibrated using the K_s^o meson signal observed in a single spectrometer arm during the ϕ-trigger data-taking period. The systematic error in the K_s^o mass measurement was found by generating events using a Monte Carlo model of the spectrometer system and subsequently presenting the accepted events to the same tracking program that was used to track the real signal. A mass shift, after the tracking program, of 0.5 MeV/c^2 was found for these events (using the same technique, no mass shift was found for the ϕ meson). Adding this systematic error in quadrature with the statistical error in the K_s^o mass measurement yielded an uncertainty in the K_s^o mass measurement of 1.0 MeV/c^2. The systematic error due to the relative uncertainty in the drift chamber wire locations was found to be negligible.

Using the Monte Carlo model it was found that a 1% shift of the magnetic field integral away from its true value caused a 0.4 MeV/c^2 shift in the measured ϕ mass and a 3.0 MeV/c^2 shift in the measured K_s^o mass. The 1.0 MeV/c^2 uncertainty in the K_s^o mass measurement then implies a calibration uncertainty in the ϕ meson mass of 0.13 MeV/c^2.

The correction for geometric acceptance as a function of mass for the $K^+ K^-$ mass histogram was found using the Monte Carlo model of the spectrometer system. The mass acceptance is shown in Figure 14. The $K^+ K^-$ mass plot with all corrections is shown in Figure 15.

The mass resolution of the detector is the result of multiple scattering and to a lesser extent drift chamber resolution. The mass resolution in the ϕ mass region was found using Monte Carlo techniques. The multiple scattering method used is discussed in Appendix A. As is stated there, the Monte Carlo resolution calculation was checked for accuracy by comparing the resultant resolution for the K_s^o with its experimentally found value. The K_s^o has a negligible width in comparison to the mass resolution in the K_s^0 mass region.

The uncertainty in the mass resolution in the ϕ mass region was found by changing the multiple scattering constants in the Monte Carlo until the mass resolution found by the Monte Carlo for the K_s^o changed by an amount equal to the uncertainty in the K_s^o experimental mass resolution. This method yielded a mass resolution for the ϕ mass region of 0.83 ± 0.09 MeV/c^2. This mass resolution uncertainty contributed an uncertainty to the measured width of the ϕ meson of 0.14 MeV/c^2. The measured mass value was not affected.

Because a ϕ meson could be observed in either spectrometer arm, the data from each arm was analyzed separately and compared. The resultant mass and width found for the two arms separately agreed to within statistical uncertainty. To generate the final values, the

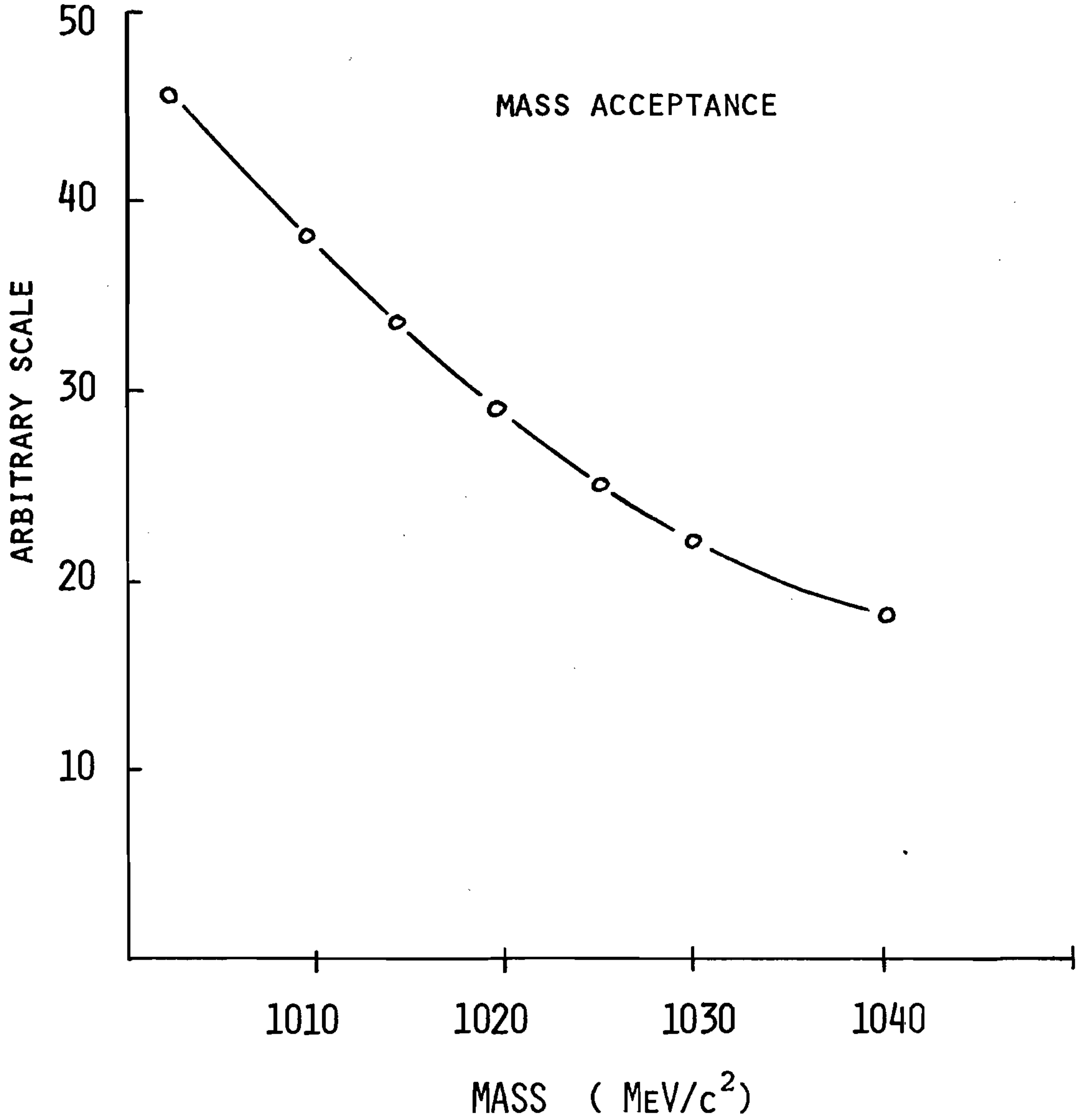

Figure 14. Geometric acceptance for $\phi \rightarrow K^+K^-$ as a function of mass.

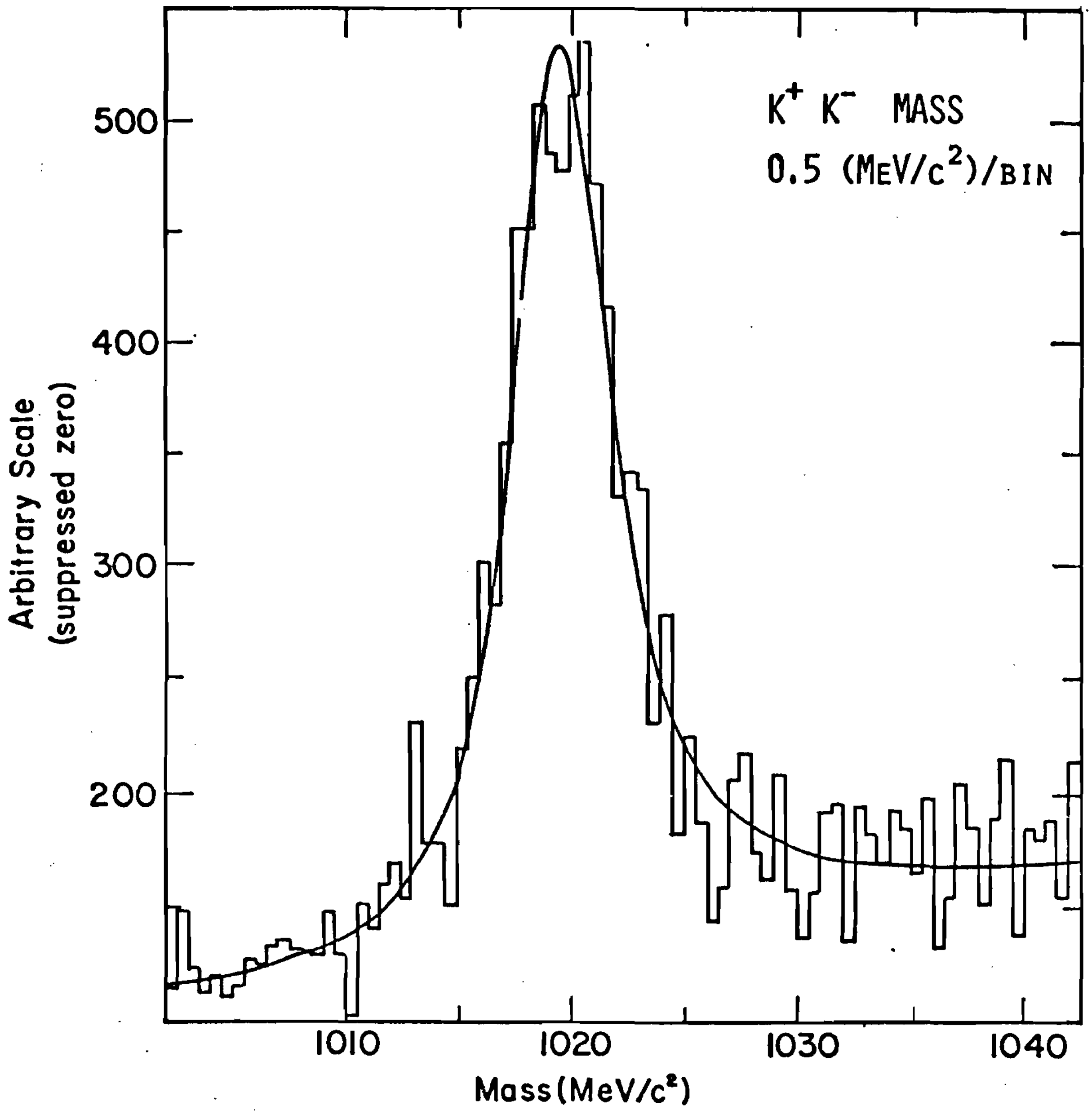

Figure 15. Corrected K^+K^- mass plot showing the fit described in the text. The χ^2 per degree of freedom is 0.9 with 80 degrees of freedom.

two data sets were added and fit with a linear background term and a signal term F(m) from 1.002 MeV/c^2 to 1.045 MeV/c^2 in 0.5 MeV/c^2 steps. The signal term is given by[30]:

$$F(m) = \int \frac{MM_o \; \Gamma(M) \; e^{-(m-M)^2/2\sigma_m^2} \, dM}{(M_o^2 - M^2)^2 + M_o^2 \, \Gamma^2(M)} \qquad 5.2$$

σ_m is the mass resolution found using the Monte Carlo. M_o is the ϕ mass value. m is the mass of the data point. M is the true mass of the particles in the mass bin m. The mass resolution was taken to be a Gaussian function of the mass. $\Gamma(M)$ is given by[30]:

$$\Gamma(M) = \Gamma_o \left[\frac{1 - (M/2m_k)^2}{1 - (M_o/2m_k)^2} \right]^{3/2} \frac{M_o}{M} \qquad 5.3$$

Γ_o is the width of the ϕ meson. m_k is the K meson mass. $\Gamma(M)$ takes into account the larger phase space for larger values of M. Because of the narrow width of the ϕ, the effect of using $\Gamma(M)$ instead of Γ_o is small. Replacing $\Gamma(M)$ by Γ_o would change the measured mass value by at most 0.1 MeV/c^2 and the measured width by 0.2 MeV/c^2. The fit had a χ^2 per degree of freedom of 0.9 with 80 degrees of freedom. The results of the fit are the mass and width values in equation 5.1. The statistical uncertainty in the fitted values were found to be 0.12 MeV/c^2 for the mass of the ϕ and 0.34 MeV/c^2 for its full width.

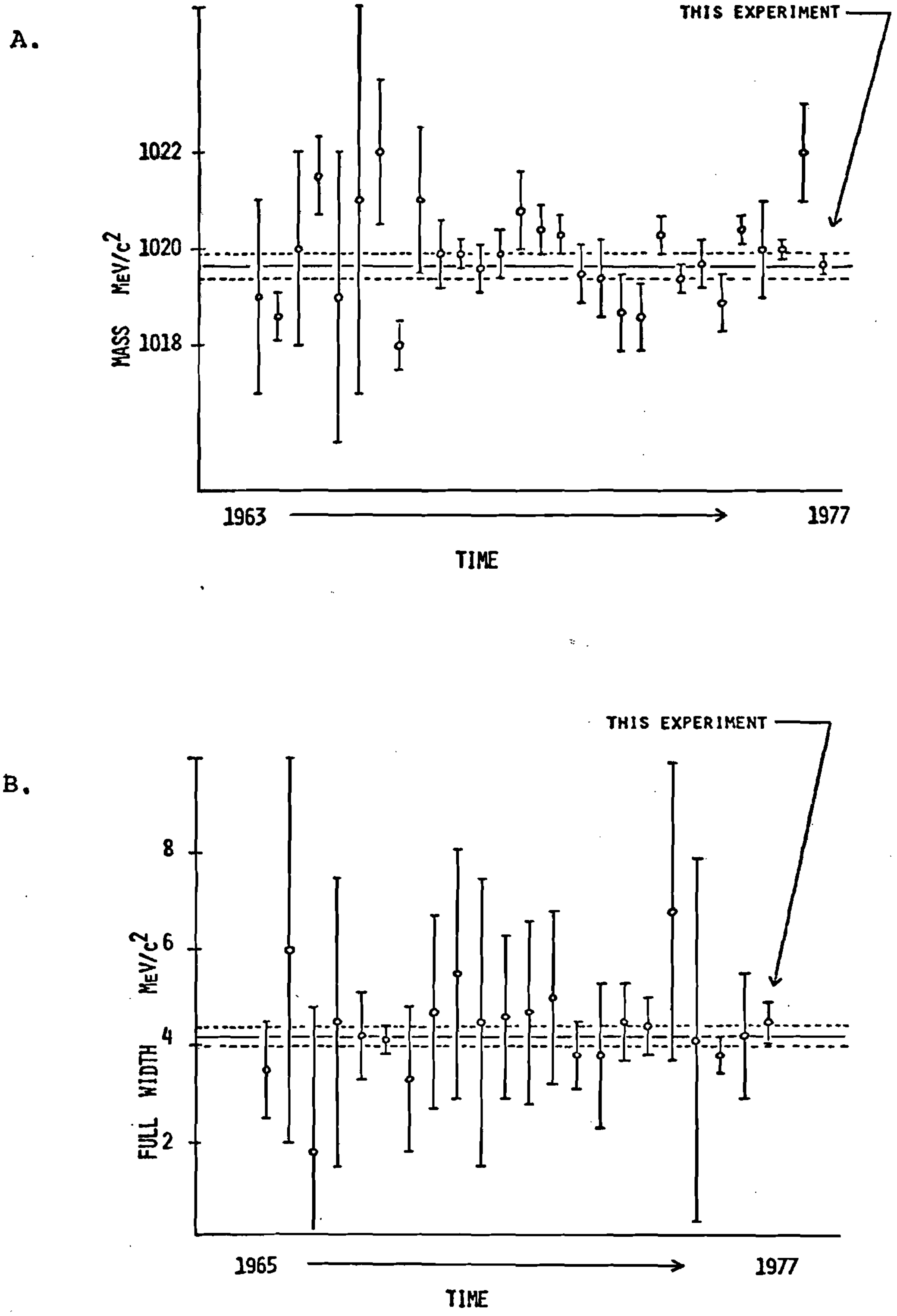

Figure 16. Figure A is the world's measurements of the ϕ meson mass. Figure B is the world's measurements of the full width of the ϕ meson. The present world average values are shown as a solid line. The band is the uncertainty in the average value. The data is taken from reference (31).

The systematic error due to uncertainties in the location of the sense wires on a drift plane was investigated and an error of 0.1 MeV/c^2 was assigned. The tracking efficiency versus mass was also investigated and found to be consistent with having no mass dependence over the narrow width of the ϕ.

The uncertainties shown in equation 5.1 are the result of all the errors, both systematic and statistical, being added in quadrature. The present world average mass and width values for the ϕ meson are[31]:

$$\begin{aligned} \langle M_\phi \rangle &= 1.01962 \pm 0.00024 \text{ GeV/c}^2 \\ \langle \Gamma_o \rangle &= 0.00413 \pm 0.00019 \text{ GeV/c}^2 \end{aligned} \qquad 5.4$$

Other experimental results and the world average values are shown in Figure 16. It should be noted that for about half the points shown, an analysis of the systematic error in the measurement is not known to have been carried out.

The ϕ Meson Invariant Cross Section

A measurement of the invariant cross section for inclusive ϕ meson production was made using 400-GeV/c protons incident on a beryllium target during the single arm ϕ-trigger mode of data taking. The measurement was made near 90 degrees (rapidity $y=-0.2$, Feynman $x_F= -0.08$) in the center-of-mass frame of a proton-nucleon collision with a sample of 1300 ϕ meson events. The ϕ invariant cross section is shown in Figure 16 and tabulated in Table 6.

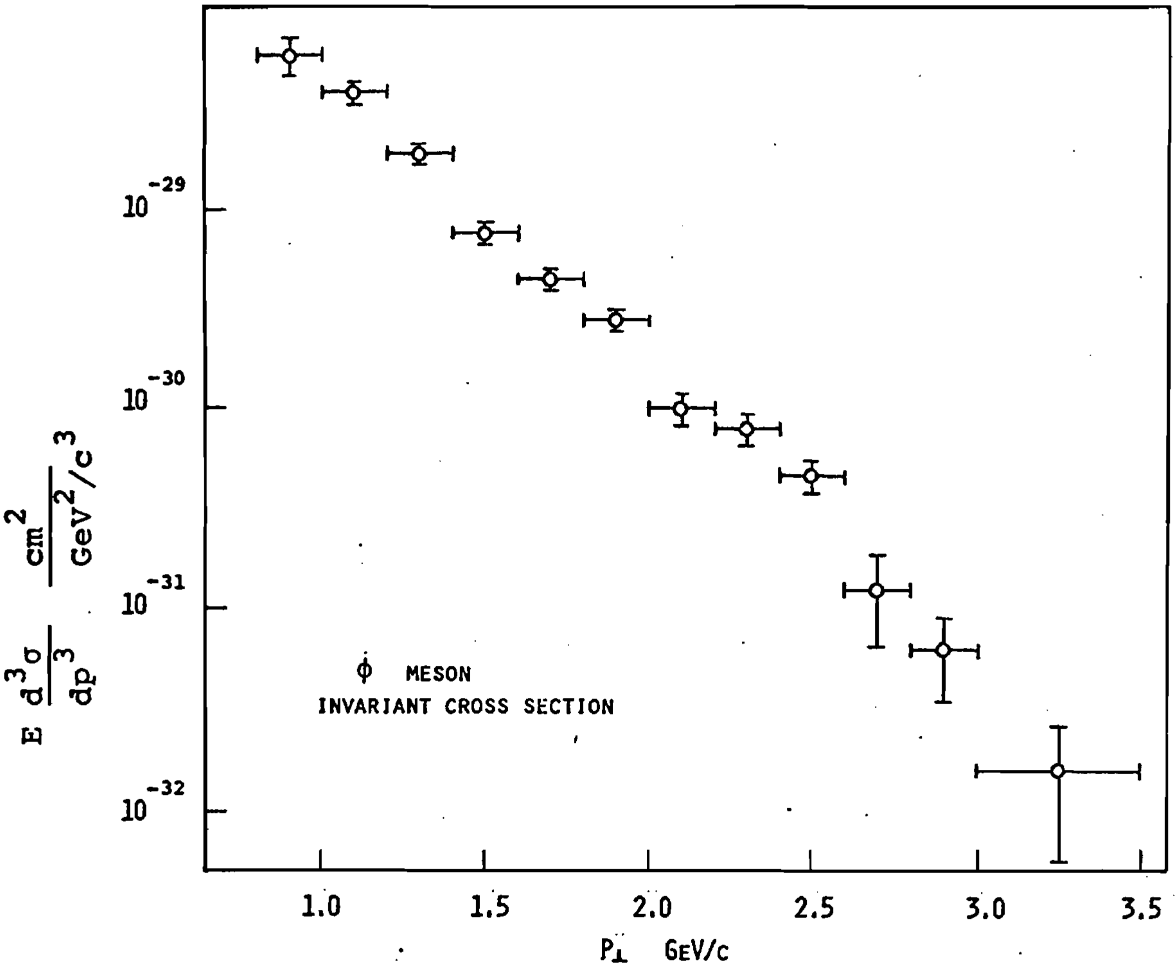

Figure 17. The ϕ meson invariant cross section per nucleus as a function of transverse momentum for the reaction P + Be → ϕ + x.

$P_\perp$	$E \frac{d^3\sigma}{dp^3}$ $\frac{cm^2}{GeV^2/c^3}$	$\frac{\phi}{\pi^-}$	$\frac{\mu^-}{\pi^-}$ From ϕ Production
0.9	$5.84 \pm 1.20 \times 10^{-29}$	$1.04 \pm 0.22 \times 10^{-2}$	$1.97 \pm 0.41 \times 10^{-6}$
1.1	$3.83 \pm 0.53 \times 10^{-29}$	$1.89 \pm 0.26 \times 10^{-2}$	$2.36 \pm 0.33 \times 10^{-6}$
1.3	$1.89 \pm 0.21 \times 10^{-29}$	$2.52 \pm 0.28 \times 10^{-2}$	$2.14 \pm 0.23 \times 10^{-6}$
1.5	$7.51 \pm 0.98 \times 10^{-30}$	$2.44 \pm 0.32 \times 10^{-2}$	$1.57 \pm 0.20 \times 10^{-6}$
1.7	$4.37 \pm 0.57 \times 10^{-30}$	$3.62 \pm 0.47 \times 10^{-2}$	$1.84 \pm 0.24 \times 10^{-6}$
1.9	$2.73 \pm 0.38 \times 10^{-30}$	$5.43 \pm 0.71 \times 10^{-2}$	$2.09 \pm 0.27 \times 10^{-6}$
2.1	$9.98 \pm 1.80 \times 10^{-31}$	$4.99 \pm 0.95 \times 10^{-2}$	$1.43 \pm 0.27 \times 10^{-6}$
2.3	$7.92 \pm 1.43 \times 10^{-31}$	$9.43 \pm 1.79 \times 10^{-2}$	$2.05 \pm 0.39 \times 10^{-6}$
2.5	$4.60 \pm 0.87 \times 10^{-31}$	$1.10 \pm 0.23 \times 10^{-1}$	$2.88 \pm 0.61 \times 10^{-6}$
2.7	$1.24 \pm 0.60 \times 10^{-31}$	$6.70 \pm 3.28 \times 10^{-2}$	$1.38 \pm 0.68 \times 10^{-6}$
2.9	$6.24 \pm 2.81 \times 10^{-32}$	$5.89 \pm 2.77 \times 10^{-2}$	$1.02 \pm 0.48 \times 10^{-6}$
3.25	$1.57 \pm 0.94 \times 10^{-32}$	$5.76 \pm 3.23 \times 10^{-2}$	$8.36 \pm 4.70 \times 10^{-7}$

Table 6. The ϕ invariant cross section, ϕ to π^- ratio, and the μ^- to π^- ratio from ϕ decay to $\mu+$ $\mu-$ as a function of transverse momentum. Not included in the invariant cross section errors is a 10%-15% normalization uncertainty. The bin widths are 200 MeV/c except for the 3.25 GeV/c data point which is 500 MeV/c.

To obtain these results the data had to be corrected for: 1.) the background in the ϕ mass region, 2.) the geometric acceptance, 3.) detection efficiency, 4.) K meson absorption and decay in flight, 5.) finite target tickness, 6.) mass acceptance, and 7.) the ϕ branching ratio to $K^+ K^-$.

The ϕ Mass Region and Background Subtraction

The ϕ mass region was found by fitting a limited portion of the $K^+ K^-$ mass plot with a Gaussian signal term and a linear background term. The Gaussian term gave a sigma of 2.5 MeV/c^2. The ϕ mass region, 1.013 to 1.026 GeV/c^2, was chosen to include 99% of the Gaussian signal.

In the ϕ mass region the signal to background ratio is about 1. In order to eliminate the background a background subtraction method was used. Attempts to subtract the background by combining the tracks in one event with the tracks in another event, to produce a randomized background, failed to produce reasonable results. Another method was to fit the mass plot versus transverse momentum, but this failed because of the small amount of data in the large transverse momentum regions. The simplest and most consistent method was the guardband subtraction method. In this method two guardbands, one below the ϕ mass region, 1.0025 to 1.0090 GeV/c^2, and one above the ϕ mass region, 1.030 to 1.0365 GeV/c^2, were used as the control regions. They were considered to be identical in everyway to the background in the ϕ mass region. Other guardband locations and widths were tested as control regions with the difference in results always within the expected statistical variation. The ϕ signal was generated by histogramming as a function of transverse momentum the difference between the number of counts in the ϕ mass region and the two guardband regions. This difference was considered to be the ϕ signal as a function of transverve momentum.

Acceptance and Detection Efficiency

The geometric acceptance for ϕ meson production as a function of transverse momentum is shown in Figure 18 and was found using the Monte Carlo model of the spectrometer. Further corrections were necessary to account for the detection efficiency because ϕ events can be lost even though the $K^+ K^-$ pair is initially moving down the spectrometer arm.

One loss is due to a K meson from the ϕ decay interacting in one of the spectrometer elements. This interaction correction was found to cause a 9% ± 1% loss of ϕ events using the data in reference (32).

Another loss of events comes from K meson decay in flight. A ϕ event with two K mesons initially moving down a spectrometer arm, has a substantial probability to have a K meson decay because of the length of the spectrometer($\sim$15 meters). (The decay loss of π mesons is less than 1%.) Using Monte Carlo methods the probability of a

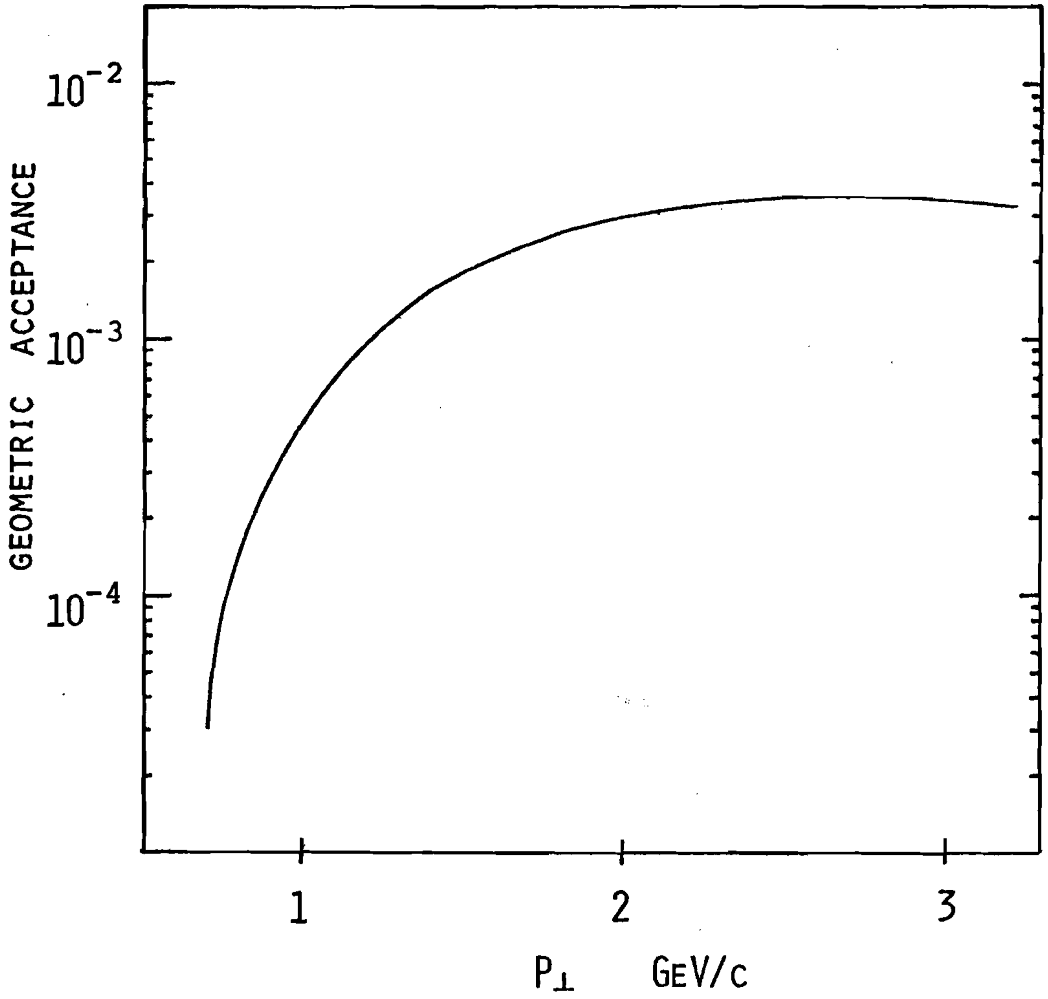

Figure 18. The geometric acceptance for $\phi \to K^+K^-$ versus transverse momentum per unit interval of rapidity.

ϕ event not to have a K meson decay in the spectrometer was found as a function of the transverse momentum of the ϕ. A small correction factor was added to this probability to account for events with decays which passed all the ϕ meson requirements. The correction factor was found to be 0.055 of those events with a K meson decay and independent of the ϕ meson's momentum. The correction for K meson decay in flight is shown in Figure 19.

An effect that can cause the loss of a ϕ event even though its decay products have traversed the geometric apertures of the spectrometer is due to the finite size of the drift chamber cells. If a pair of tracks pass through the same cell of a drift chamber, only the track closest to the sense wire will be recorded. To measure this effect, ϕ events were generated using the Monte Carlo model, and were converted to hit information a certain distance from a sense wire. The tracks were allowed to interfere with one another as in the real drift chamber system by accepting only one hit per cell. At this stage the information was in the same form that real data would be in. The Monte Carlo output in this form was then presented to the tracking program which was used to create the real ϕ data set.

ϕ events from the Monte Carlo which had not been multiple scattered had a 65% probability of being found by the tracking program. When multiple scattering was included

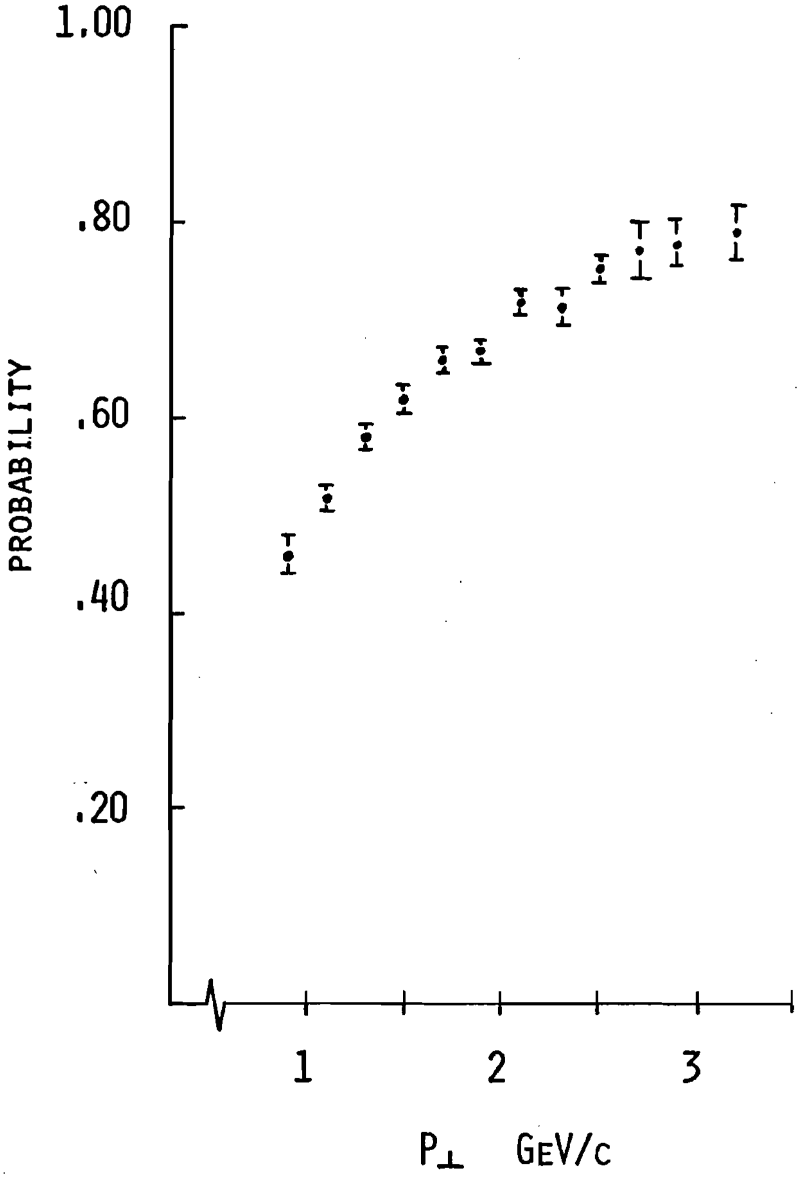

Figure 19. The probability, as a function of the ϕ meson's transverse momentum, that a ϕ event will not be lost due to K meson decay in flight.

this became 63%. Other effects that must be included are drift chamber efficiency, drift chamber resolution and target cuts. The chamber efficiencies were determined from the real data sets by observing how often a chamber missed a hit when, from the other chambers, there was sufficient information to reconstruct a track. Drift chamber resolution was included using a Gaussian smearing function with a variance of 250 microns found from the data. Including the drift chamber efficiency and resolution the tracking efficiency was reduced to 56.5%. Including the target cuts reduced the number of detected phi meson's to 53.7% of those that passed through the detector.

Important effects on the detection efficiency are the extra hits in the drift chambers and the Cherenkov counters, which are due to the high multiplicity associated with high energy collisions. These extra hits have the effect of deleting hit information in the drift chambers and cause spurious counts in the cherenkov counters, both of which cause the loss of phi events. Figure 20 shows a $\phi \rightarrow K^+ K^-$ event with its accompanying extra hits.

A study of the extra hits in the triggering arm and the untriggered arm suggested a natural way to understand how the detection efficiency is affected by these extra hits. The Monte Carlo was used to place tracks onto the

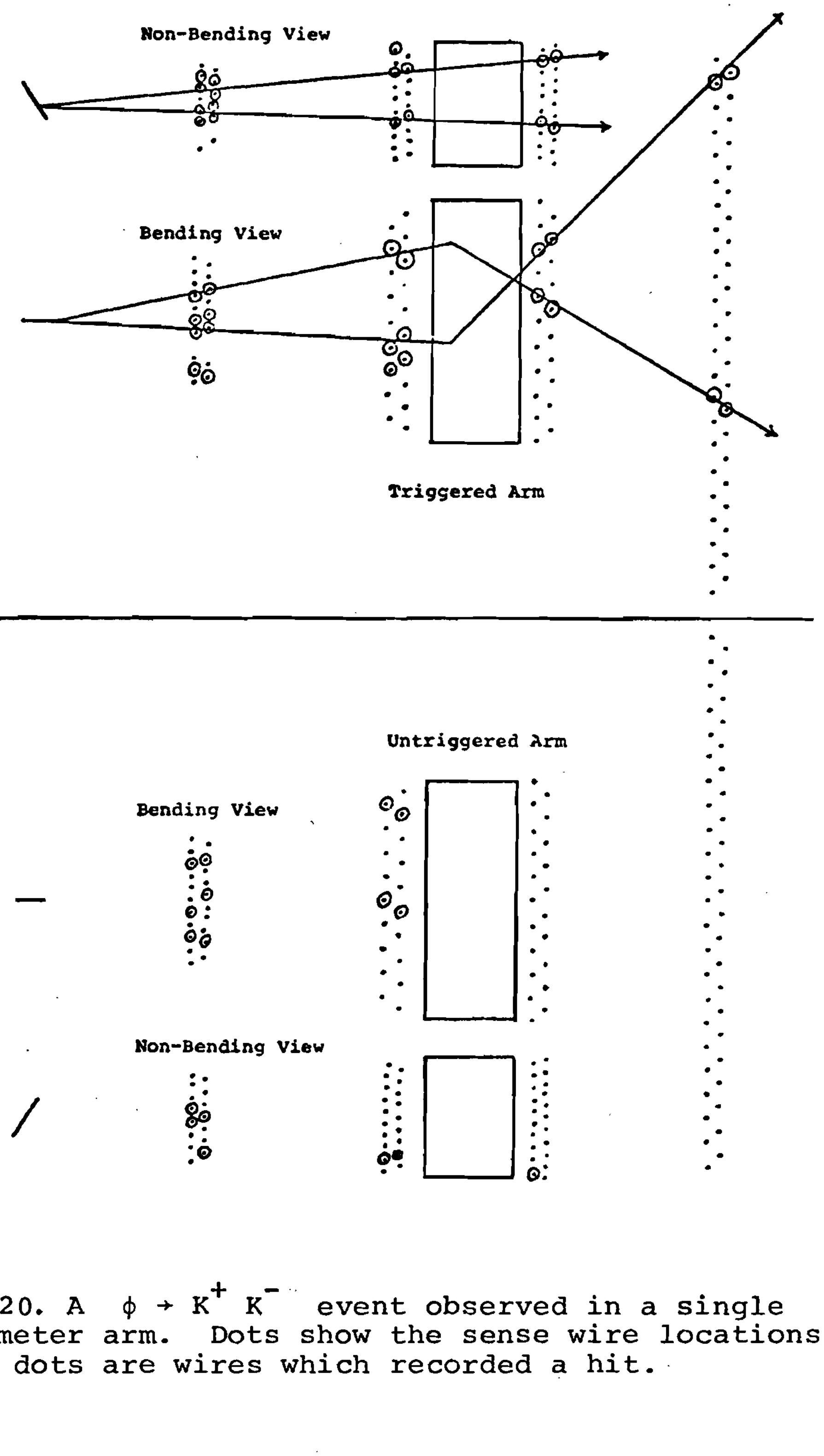

Figure 20. A $\phi \rightarrow K^{+} K^{-}$ event observed in a single spectrometer arm. Dots show the sense wire locations; circled dots are wires which recorded a hit.

drift chamber system, and then these tracks were allowed to interfere with an overlay of extra hits from the untriggered arm of a real data set. This data was then presented to the tracking program to find the corrections. In this way it was found that the correct correlation of the extra hits and the correct number of extra hits is taken into account.

The extra hits were studied using a single arm trigger. The average of the multiplicity distribution of wire hits in the untriggered arm and the triggered arm were found to be consistent with having no dependence with the momentum of the triggering particle. The variance of both distributions was found to be momentum independent. The first drift chamber plane is the most sensitive to extra hits, having the highest average multiplicity. Investigation of its multiplicity distribution for the triggering arm and the untriggered arm also showed no momentum dependent effect. Figure 21 shows plots of these distributions.

A high degree of correlation between hits on one plane and hits in the following plane were found in the data. Figure 22A shows the difference between the number of hits in plane 1 and plane 2 of the triggered arm. Figure 22C shows the resultant difference histogram, from a simple Monte Carlo program, using the multiplicity distributions found for planes 1 and 2, and assuming no correlation between the two planes. The widths of the two difference distributions qualitatively shows that the data has a high

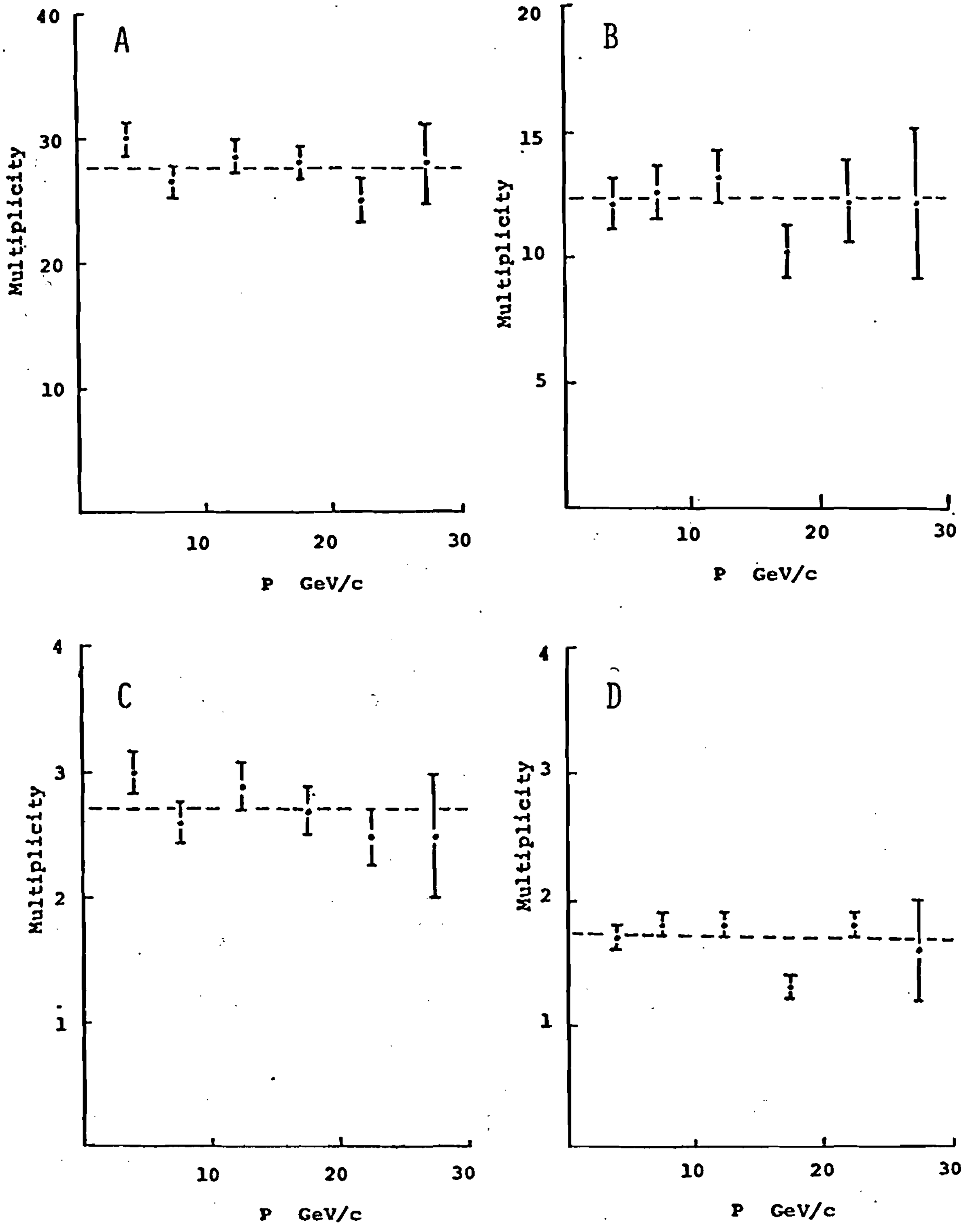

Figure 21. The average multiplicity as a function of the triggering particle's momentum in the A.) triggering arm, B.) untriggered arm, C.) first plane in the triggering arm, D.) first plane in the untriggered arm.

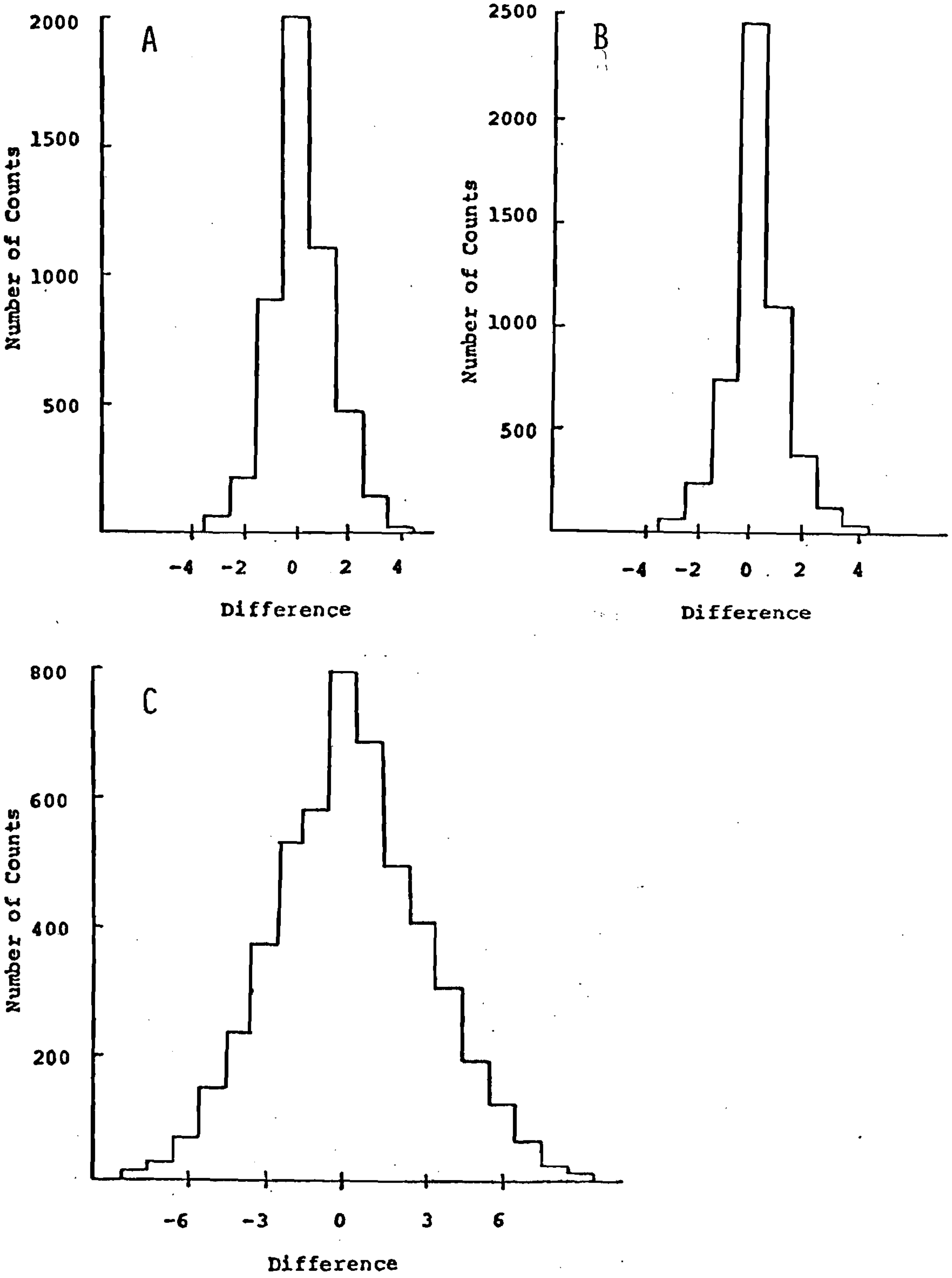

Figure 22. The difference between the hits in plane 1 and 2 in the A.) triggering arm, B.) untriggered arm, C.) Monte Carlo with no correlation.

degree of correlation. Figure 22B shows the difference distribution for the untriggered arm. Notice that its width is very close to the triggered arm's differnece distribution. This indicates that the extra hits in the triggered arm and the untriggered arm behave in a similar manner.

The number of extra hits in the triggered arm and the untriggered arm were compared. The average number of hits in the first drift chamber plane in the triggered arm is 2.40 ± 0.02. The average number of hits in the first drift chamber plane in the untriggered arm is 1.39 ± 0.02. The difference is very close to one, due to the triggering track. The average number of wires hit in the triggered arm is 25.62 ± 0.15. The average number of wires hit in the untriggered arm is 9.62 ± 0.15. Knowing the chamber efficiencies one finds the average number of wires which respond to a track passing through the spectrometer is 15.65. Adding this to the hits in the untriggered arm yields 25.25 ± 0.4. These results indicate that the average number of extra hits accompanying a track is identical to the average number of hits in the untriggered arm.

Using the overlay method the detection efficiency for the ϕ meson drops to 46.6%. Figure 23 shows that there are no momentum dependent effects due to the tracking program. Using the overlay method on a single particle

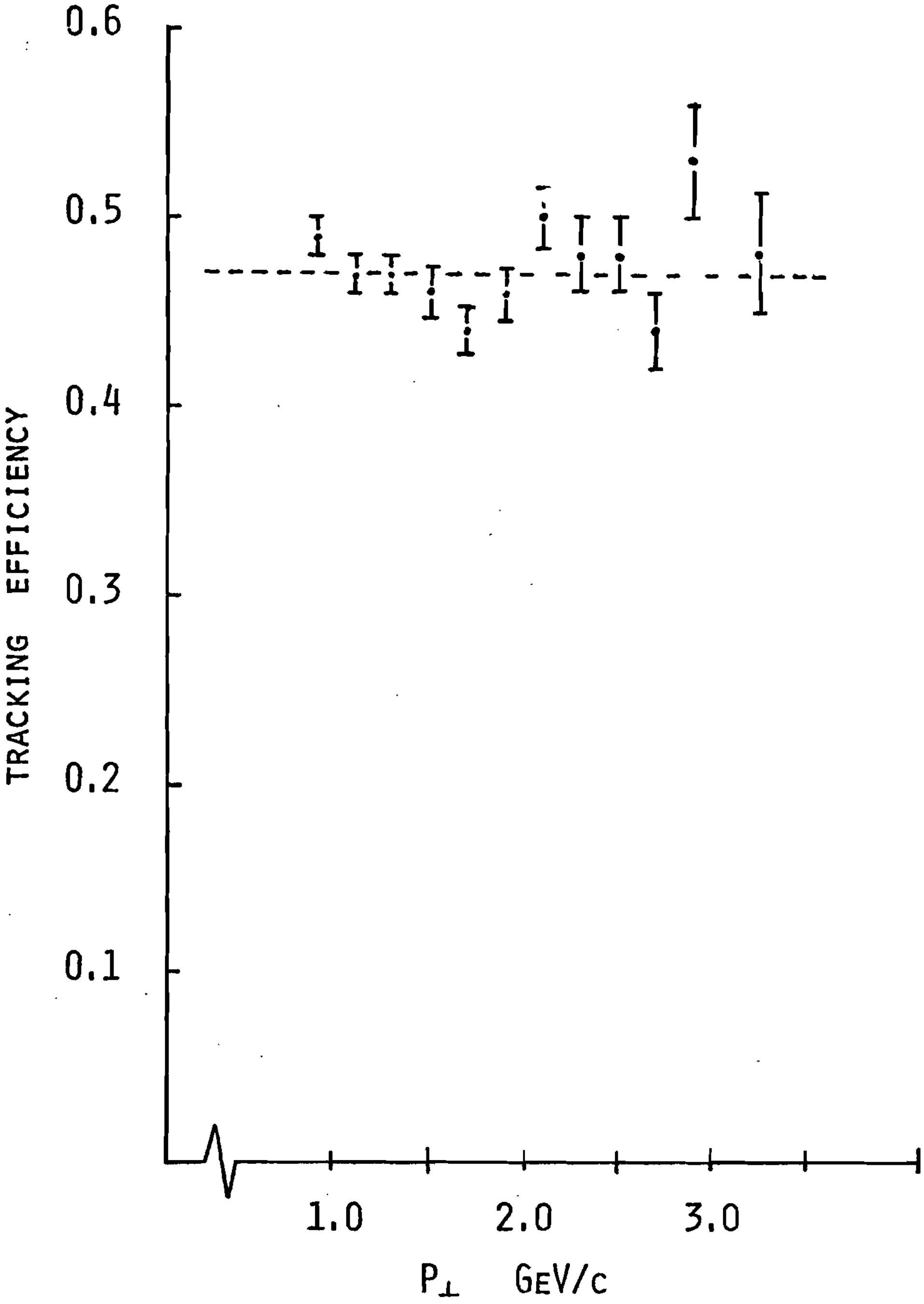

Figure 23. The probability that a $\phi \rightarrow K^+K^-$ event will be tracked if it passes through the geometric apertures of the spectrometer. The tracking efficiency was found using the overlay method.

moving through the spectrometer yields a tracking efficiency of 97%. In other words the effect is only important when two tracks are in the same arm.

To account for ϕ losses due to spurious extra hits in the Cherenkov counters, it was assumed that these extra hits affected the Cherenkov counters in the triggered and untriggered arm in a similar manner. Under this assumption the loss of events can be understood by superimposing the untriggered arm Cherenkov counter responses onto Monte Carlo events as was done in the case of the drift chambers. Table 7 shows the probability of occurrence of each Cherenkov overlay pattern.

The detection efficiency correction was then found by overlaying Monte Carlo events, simultaneously, with the hits in the drift chambers and the Cherenkov counters observed in the untriggered arm of a real data set. Using this method the average detection efficiency for a ϕ event was found to be 38%. The overlay method is outlined in Figure 24.

Using the discussed correction the ϕ invariant cross section as a function of transverse momentum was found using the following equation:

Probability of Occurrence of Each Overlay Pattern

Cherenkov Counter Pattern C1	C2	C3	Probability of Occurrence
0	0	0	0.707
0	0	1	0.015
0	1	0	0.107
0	1	1	0.141
1	0	0	0.011
1	0	1	0.006
1	1	0	0.003
1	1	1	0.015

Table 7. The probability of the occurrence of a given Cherenkov counter pattern in the untriggered arm when a particle is observed in the triggered arm. "0" means the counter gives no response; "1" means the counter gives a response.

OVERLAY METHOD

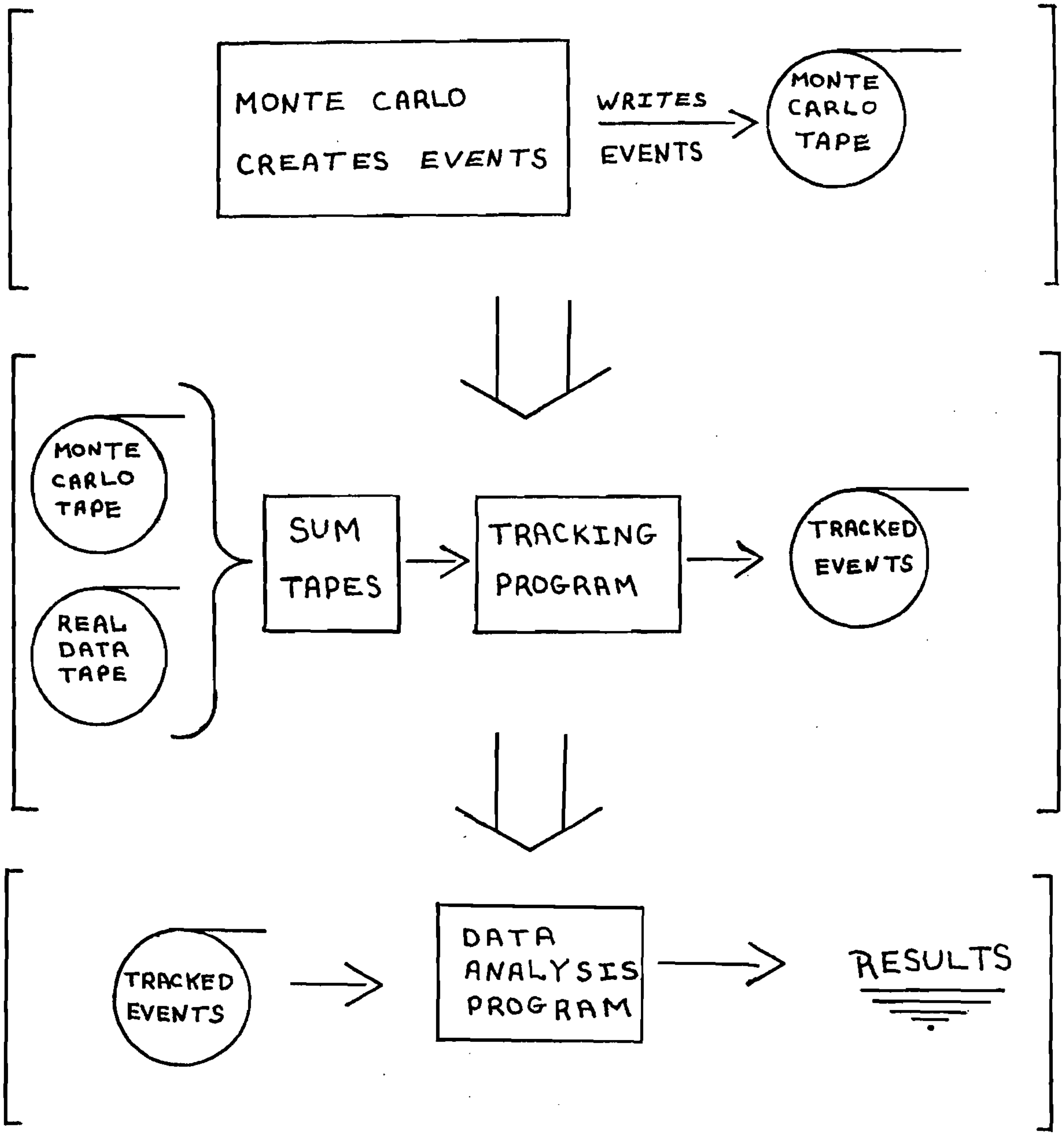

Figure 24 . The overlay method of correcting for extra hits in the drift chambers and Cherenkov counters. In this method the random hits in a real data set are added to Monte Carlo generated ϕ events to find corrections to the data.

$$E\,\frac{d^3\sigma}{d^3p} = \left[\,2\pi\cdot\varepsilon(P_\perp)\cdot T(P_\perp)\cdot\tilde{D}(P_\perp)\cdot M_\varepsilon\cdot A\cdot B_{K^+K^-}\cdot\Delta P_\perp\cdot P_\perp\,\right]^{-1}\ \mathrm{x}\ \frac{N_\phi(P_\perp)}{N_B}\ \mathrm{x}\ \left\{\frac{\sigma_A}{1-\mathrm{EXP}(-\sigma_A\rho\ell)}\right\} \qquad 5.5$$

where:

$P_\perp$	is the transverse momentum
$\varepsilon(P_\perp)$	is the geometric acceptance as a function of $P_\perp$ per unit of rapidity and azimuth angle.
$T(P_\perp)$	the detection efficiency found using the overlay method.
$\tilde{D}(P_\perp)$	the K meson flight decay correction.
M_ε	the ϕ mass cut acceptance 0.99 ± 0.01
A	K meson interaction correction 0.91 ± 0.01.
$B_{K^+K^-}$	the branching ratio for $\phi \to K^+K^-$, 0.466 ± 0.023
$\Delta P_\perp$	the bin width
$N_\phi(P_\perp)$	the number of detected ϕ events at $P_\perp \Delta P_\perp$.
N_B	the number of incident protons.
σ_A	the absorption cross section for 400-GeV/c protons on beryllium(33)
ρ	the target density (nuclei/cm^3)
ℓ	the target length.

The term in { } corrects for absorption of the beam in the target, which is a 6% effect. The errors shown in

Figure 17 and Table 6 are due almost entirely to the statistical uncertainty in the data. A systematic error in the beam flux measurement, estimated to be 10%-15% is not included.

The invariant cross section as a function of transverse momentum was fit to the form:

$$e^{-\alpha P_\perp} \qquad 5.6$$

α, the slope parameter, was found to be 3.36 ± 0.14 $(\mathrm{GeV}/c)^{-1}$. The fit had a χ^2 per degree of freedom of 1.2 for 10 degrees of freedom. This may be compared to $\alpha = 3.93 \pm 0.28$ $(\mathrm{GeV}/c)^{-1}$ obtained in a different experiment[34] using 150-GeV/c protons incident on a beryllium target, for ϕ mesons with $P_\perp \lesssim 2.0$ GeV/c and Feynman $x_F > 0.15$.

Theoretical predictions for ϕ meson production will be compared to our data in terms of the ϕ/π^- ratio in the next section.

The ϕ/π^- Ratio

Particle ratios have become a common way to express results, being more accurate because they eliminate many systematic effects that may cause errors in the single particle cross section. In this experiment, by using the ϕ/π^- ratio, the beam normalization uncertainty is eliminated. Ratios are also easier to predict using models than are the absolute cross sections. The ϕ/π^- ratio is predicted by the thermodynamic model and the Field and Feynman model. Both models will be compared to our data.

To generate the ϕ/π^- ratio, the π^- invariant cross section as a function of transverse momentum was found using the same target and detector configuration as the ϕ meson data sample. The only difference was the use of an XL trigger.

Because π and K mesons could not be separated in the Cherenkov counters above a momentum of 19.9 GeV/c, the number of π^- mesons with a momentum below and above 19.9 GeV/c was found differently. Above 19.9 GeV/c, the number of negatively charged tracks was found as a function of transverse momentum. The particle ratios K^-/π^- and P^-/π^-, as a function of transverse momentum, were extrapolated from data on deuterium to beryllium, using the data in references (35) and (36). The ratios were computed using the equation:

$$\left[\frac{x^-}{\pi^-}\right]_{\text{beryllium}} = \left[\frac{A_{Be}}{A_D}\right]^{\alpha_{x^-}(P_\perp)} \left[\frac{A_D}{A_{Be}}\right]^{\alpha_{\pi^-}(P_\perp)} \left[\frac{x^-}{\pi^-}\right]_{\text{deuterium}} \qquad 5.7$$

A_D and A_{Be} are the atomic numbers of deuterium and beryllium. x stands for K^- meson or anti-proton. The slope parameter, $\alpha(P_\perp)$, is a function of transverse momentum and is known to 1%. These values were used to subtract the K^- meson and anti-proton components in the observed negative particle spectrum. This correction introduces only a 4% uncertainty into the π^- invariant cross section above a transverse momentum of 2 GeV/c.

Below 19.9 GeV/c, a π^- identification was required, as was described in Chapter 4. The number of π^- found in this way was then corrected for Cherenkov counter inefficiencies. At this point, the number of counts in the two regions was added as a function of transverse momentum and corrected for geometric acceptance (Figure 9), tracking efficiency (∿97%), beam attenuation (∿6%) and π^- absorption in the spectrometer (∿4%). The result is the inclusive π^- invariant cross section for 400-GeV/c proton on a beryllium target at a rapidity $y = -0.2$ ($x_F = -0.08$) (Figure 25). The result has been compared to the data in reference (37) and agrees to within 10% (Figure 25). Both experiments have beam normalization uncertainties of 10% to 15%.

The ϕ/π^- ratio can now be found by dividing the ϕ invariant cross section by the π^- invariant cross section. The result is shown in Figure 26 and tabulated in Table 6. The error shown is almost entirely due to the uncertainty in the ϕ invariant cross section. As can be seen, the ϕ/π^- ratio rises from about 1% at a $P_\perp \sim 1$ GeV/c to become flat at 7% or 8% above a $P_\perp \sim 2.5$ GeV/c. In Figure 27 are shown the thermodynamic model prediction and the Field and Feynman model prediction.

The Field and Feynman prediction fits well above a transverse momentum of 2.3 GeV/c. This is consistent with the region in which their model is expected to work. It

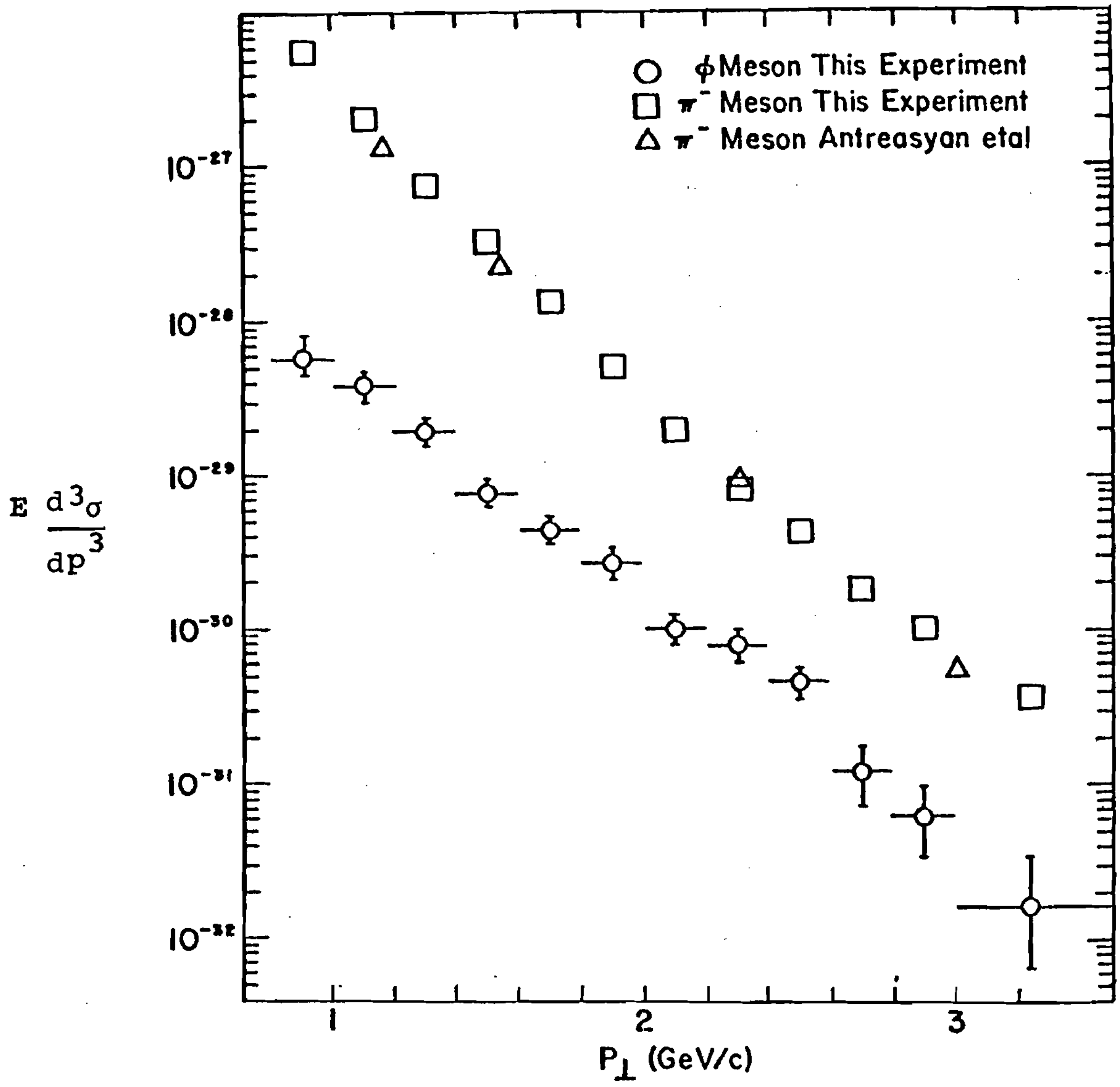

Figure 25. The π^- invariant cross section for the reaction $p + Be \to \pi^- + X$. Also shown is the ϕ invariant cross section.

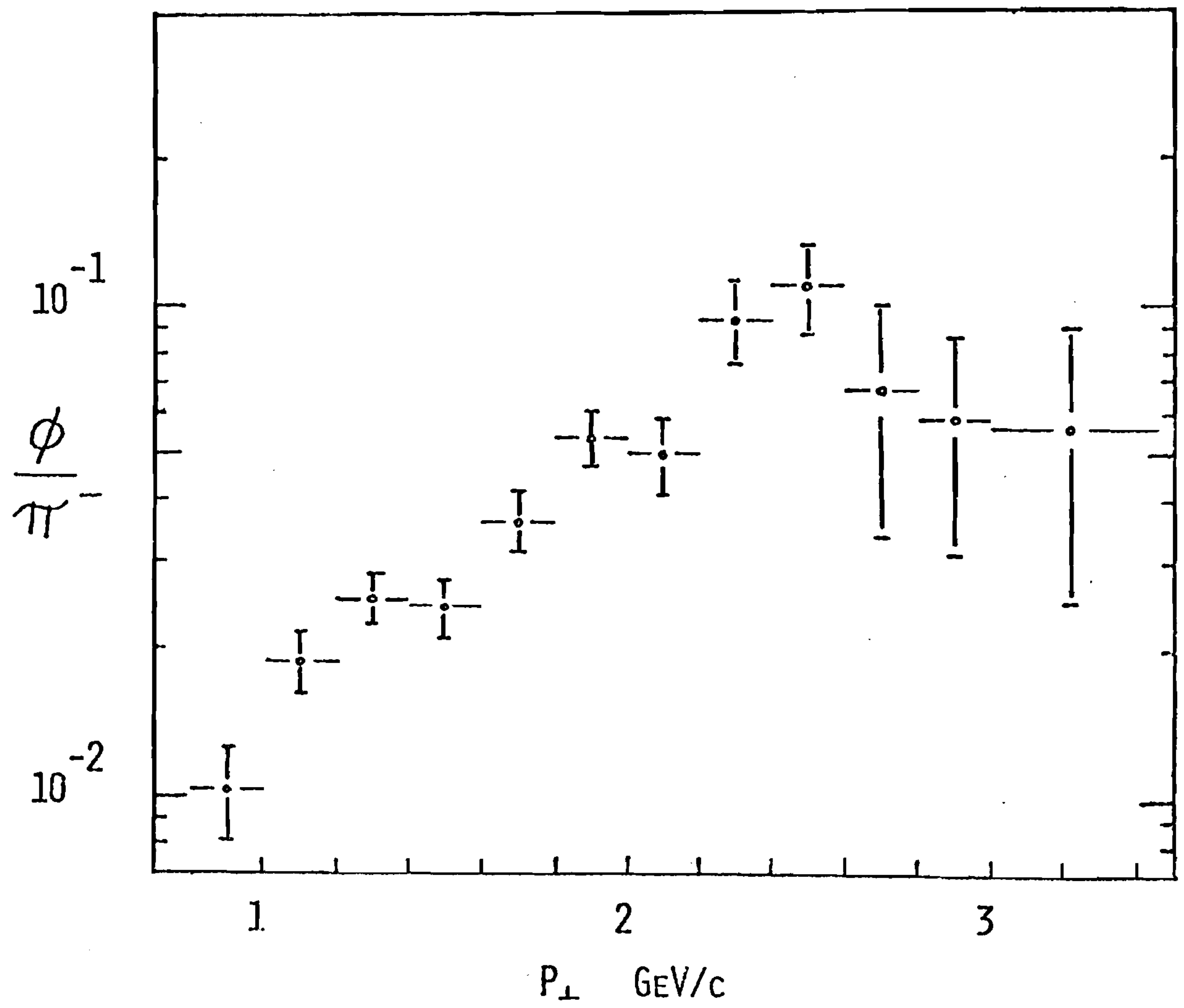

Figure 26. The ϕ/π^- ratio as a function of transverse momentum.

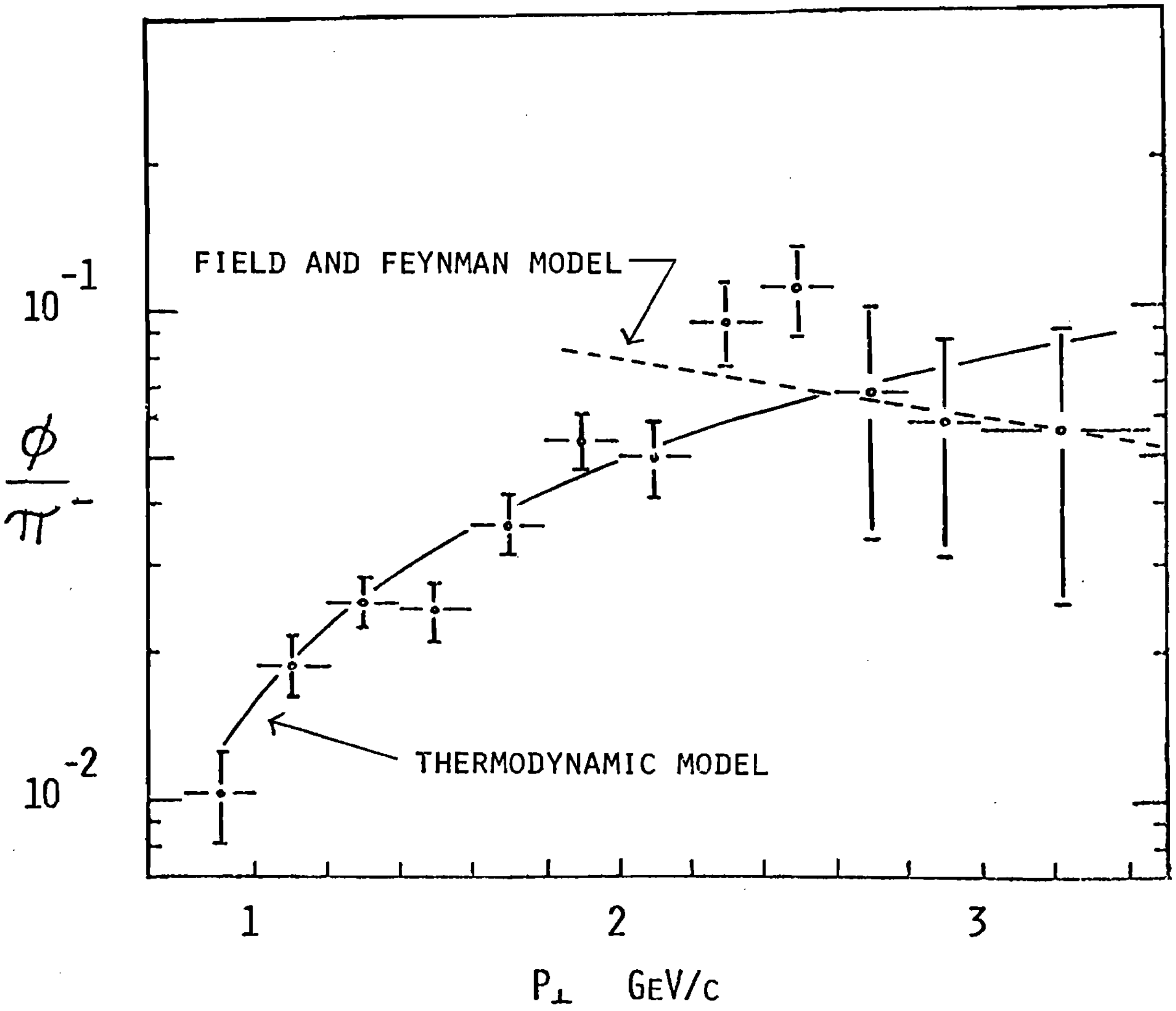

Figure 27. The ϕ/π^- ratio found in this experiment with the Field and Feynman model prediction having no free parameters and the Thermodynamic model prediction with one free parameter.

should be noted that their prediction has no free parameters. The level is set by the degree of SU(3) symmetry breaking found using the known K/π ratio at large $P_\perp$. Below a $P_\perp$ of 2.2 GeV/c, the model predicts a rising ϕ/π^- ratio whereas the data is falling. This may indicate that the ϕ production mechanism is different for low and high transverse momentum.

The thermodynamic model makes a prediction for the ϕ/π^- ratio at 90 degrees in the center of mass which is given by[38]

$$\frac{\phi}{\pi^-} = \frac{X\ (2J_\phi + 1)\ \mathrm{EXP}\ \{-(P_\perp^2c^2 + M_\phi^2c^4)^{1/2}/T\}}{\mathrm{EXP}\ \{-P_\perp^2c^2 + M_\pi^2c^4)^{1/2}/T\}} \qquad 5.9$$

T was taken to be 170 MeV. X is a free parameter. In the strict thermodynamic model, X = 1. But this gives a ratio which is too large by more than an order of magnitude. X is a suppression factor not predicted by the model to take into account that ϕ meson production without associated strange particles violates the O-Z-I rule. This dynamic effect does not allow the ϕ to reach full equilibrium during the collision. From the data, X is found to be $\sim$1/15. The thermodynamic model is not expected to hold for transverse momentum much greater than 1 GeV/c. But as can be seen in Figure 27, its prediction is reasonable at larger transverse momentum once the suppression factor is known.

The Contribution to μ^-/π^- from ϕ Production

Because the ϕ meson decays to $\mu^+\mu^-$, it makes a contribution to the "direct" muon spectrum. As was stated

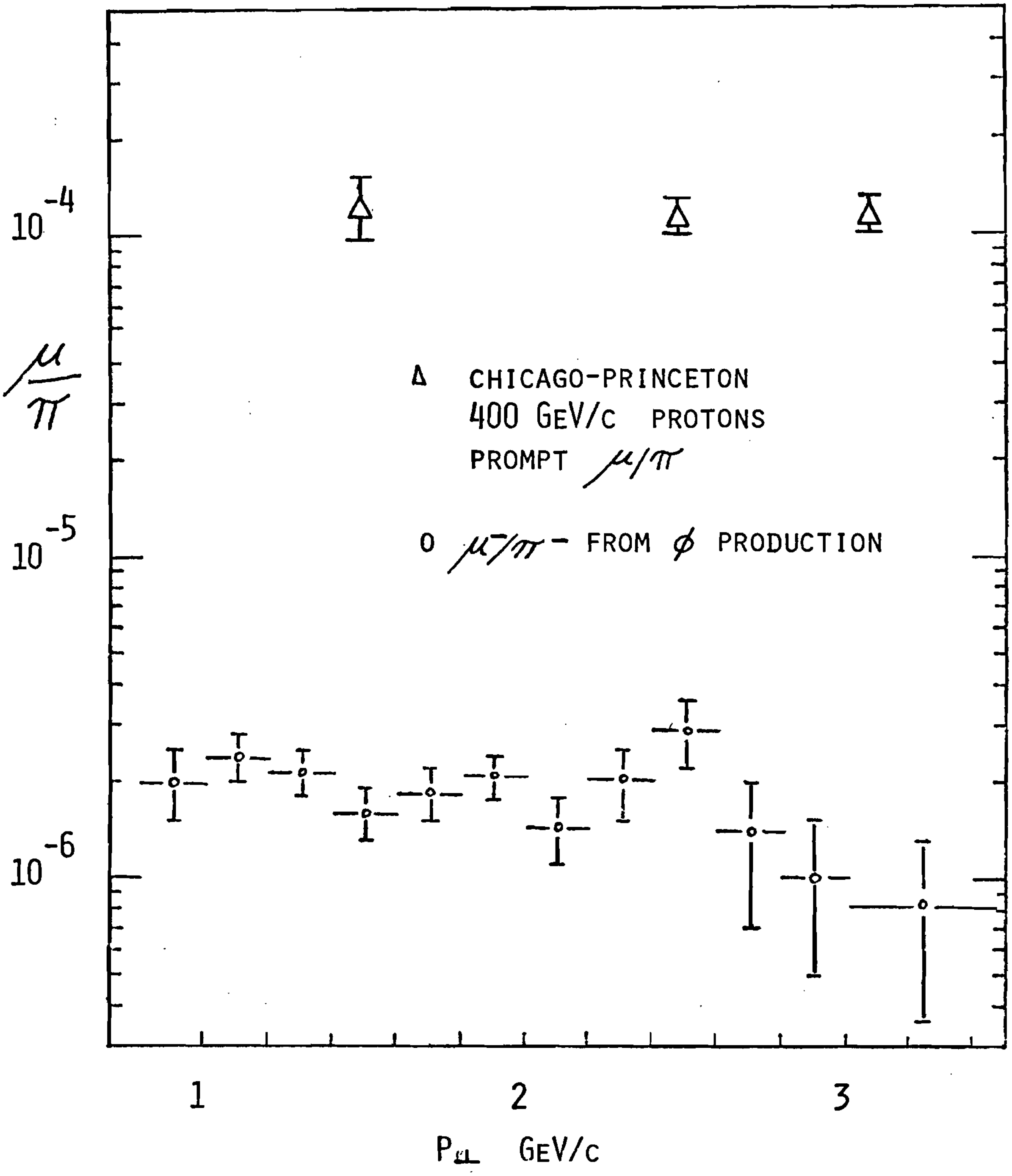

Figure 28. The prompt μ/π ratio and the μ^-/π^- ratio due to ϕ meson production. See reference (27) for a summary of the present μ/π data.

in Chapter II, the μ/π ratio is flat, as a function of transverse momentum and equal to $\sim 10^{-4}$. A larger portion of the ratio was thought to result from the decay of low-mass vector mesons, with the ϕ meson being the major contributor, having a $\mu^+\mu^-$ branching ratio 7 times larger than the ρ^o meson. Another group[26] found strong upper limits for the ϕ meson's contribution to the μ/π ratio, which rule out the ϕ as a significant source of direct leptons, but until our experiment, the ϕ meson's contribution was unknown.

The ϕ meson's contribution to the μ^-/π^- ratio can be found using the equation:

$$\frac{\mu^-(\phi\ \text{decay})}{\pi^-} = \left[\frac{\mu^-(\phi\ \text{decay})}{\phi}\right]_{\text{Monte Carlo}} \cdot \left[\frac{\phi}{\pi^-}\right]_{\text{measured}} \qquad 5.10$$

The ϕ/π^- ratio is known from our previous result. μ^- (ϕ decay)/ϕ was found by using the known branching ratio of $2.5 \pm 0.3 \cdot 10^{-4}$ for $\phi \rightarrow \mu^+\mu^-$ and a Monte Carlo program which generates the μ^- spectrum from the known ϕ spectrum. The Monte Carlo calculation used as input the measured transverse momentum slope parameter found from the ϕ data and the assumption that ϕ production is not polarized. Using this technique, the μ^- (ϕ decay)/π^- ratio was found as a function of transverse momentum. The results are shown in Figure 28 and are tabulated in Table 6. As can be seen, the μ^-(ϕ decay)/π^- ratio is flat at $\sim 2 \cdot 10^{-6}$, whereas the total μ/π ratio is flat at $\sim 10^{-4}$. The μ^-(ϕ decay)/π^- ratio is almost two orders of magnitude below the total direct muon production. This rules out the ϕ as a major contributor to the ratio.

Presently the production of $\mu^+ \mu^-$ pairs seems to account for the observed μ/π ratio[34,39]. This rules out a large contribution from the weak decays of heavy particles. present QCD calculations[40] for di-lepton production make predictions for the μ/π ratio which are in agreement with the data.

Test of the O-Z-I Rule

In searching for the charmed D^0, we recorded events with a single identified hadron, K meson, π meson or proton in each spectrometer arm (2 track events) and events with two tracks in one spectrometer, with an identified hadron in the opposite arm (3 track events). In the 2 track events, a strong $K^+ K^-$ correlation was observed. That is, the probability to detect a K meson in one spectrometer arm was found to be enhanced 49% when a K meson of opposite strangeness was observed in the oposite arm, in comparison with the probability that a K meson is observed opposite a π meson of opposite charge (same strangeness K mesons were found to be uncorrelated)[41]. We attributed this strong K^+K^- correlation to the conservation of strangeness in the strong interaction. Specifically, $K^+ K^-$ production would proceed through a diagram like Figure 29. Likewise, if ϕ meson production proceeds in accordance with the O-Z-I rule, we would expect to observe a strong ϕ-K correlation because the production of a ϕ meson should be associated with the production of two strange particles as in Figure 3. The dynamic consequences of these production mechanisms are unknown, but considering the large amount of center-of-mass energy (27.4 GeV), it seems reasonable to assume that the distribution of ϕ-K in Figure 3 and the distribution of K-K in Figure 29 are not very different at 90 degrees in the center-of-mass system. With this assumption, we expect the observation of a K meson opposite a ϕ meson to have an enhancement 2 times larger than the observed K^+K^- enhancement. This enhancement was searched for using the 3 track events, in which a sample of $\sim$480 ϕ mesons were recorded opposite an identified π or K meson.

To quantify the search, the probability of observing a charged K meson in coincidence with the ϕ is compared to the probability of observing a K meson in coincidence with a π meson. The motivation for this comparison is that the ratio of K meson occurrence in ϕ events to K meson occurrence in π meson events should be one if the ϕ behaves like an ordinary nonstrange particle such as the π. If however, the ϕ is associated with additional strange particle production this ratio should be larger than one. As a measure of K meson occurrence in ϕ or π events, we take

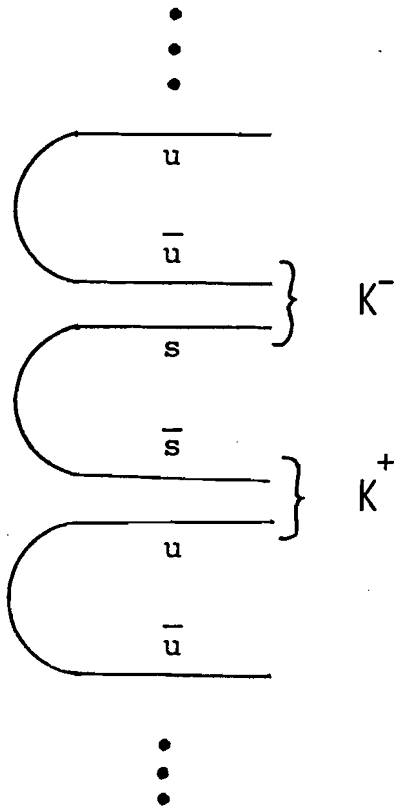

Figure 29. O-Z-I allowed $K^+ K^-$ production.

the ratio of events in which a K meson is observed to events in which a π meson is observed opposite the ϕ or π. This quantity is expressed $\left[\frac{K}{\pi}\right]_\phi$ or $\left[\frac{K}{\pi}\right]_\pi$.

The ϕ-K correlation strength is then defined as:

$$C_{\phi K} = \frac{\left[\frac{K}{\pi}\right]_\phi}{\left[\frac{K}{\pi}\right]_\pi} \qquad 5.11$$

In a similar manner the $K^+ K^-$ correlation strength can also be defined and measured. But in this case the $K^+ K^-$ correlation strength can be measured in two ways;

$$C_{K^+} = \frac{\left[\frac{K^-}{\pi^-}\right]_{K^+}}{\left[\frac{K^-}{\pi^-}\right]_{\pi^+}} \qquad C_{K^-} = \frac{\left[\frac{K^+}{\pi^+}\right]_{K^-}}{\left[\frac{K^+}{\pi^+}\right]_{\pi^-}} \qquad 5.12$$

C_{K^+} (C_{K^-}) measures the enhancement of a K^+ (K^-) in one arm when a K^- (K^+) is observed in the opposite arm, relative to observing a K meson opposite a π meson of opposite charge. C_{K^+} and C_{K^-} measure the same $K^+ K^-$ correlation strength and were found to be equal to within statistical error. The $K^+ K^-$ correlation strength is defined to be:

$$C_{K^+K^-} = (C_{K^+} + C_{K^-})/2 \qquad 5.13$$

Both $C_{\phi K}$ and $C_{K^+K^-}$ are invariant to corrections to the ratio of K and π mesons opposite the sample particle. To show this let ε_k be the correction factor for K meson losses or gains and likewise let ε_π be the π meson correction factor. Correcting $C_{\phi K}$

$$C'_{\phi K} = \frac{\left[\frac{\varepsilon_k}{\varepsilon_\pi}\frac{K}{\pi}\right]_\phi}{\left[\frac{\varepsilon_k}{\varepsilon_\pi}\frac{K}{\pi}\right]_\pi} = \frac{\frac{\varepsilon_k}{\varepsilon_\pi}\left[\frac{K}{\pi}\right]_\phi}{\frac{\varepsilon_k}{\varepsilon_\pi}\left[\frac{K}{\pi}\right]_\pi} = C_{\phi K} \qquad 5.14$$

Hence $C_{\phi K}$ is invariant. Likewise $C_{K^+K^-}$ can be shown to be invariant. $C_{\phi K}$ and $C_{K^+K^-}$ are not, however, invariant to misidentification of the subscripted particle type. For example protons and π mesons misidentified as K mesons tend to reduce the ratio $\left[\frac{K^+}{\pi^+}\right]_{K^-}$ and hence the measured K^+K^- correlation. The multiplicative correction factor to the ratios is

$$\sim (1 + \eta)(\eta + \bar{Z}/Z)^{-1} \qquad 5.15$$

Here η is the signal to noise ratio or the number of correctly identified subscripted particles divided by the number of misidentified subscripted particles. $\bar{Z}$ is the $\frac{K}{\pi}$ ratio of the background and Z is the $\frac{K}{\pi}$ ratio of the signal.

For a sample of π mesons the effect of the correction factor is 2% or less depending on the data set. For a sample of K mesons with a momentum below 13.5 GeV/c the effect of the correction is about 1%. For K mesons with a momentum above 13.5 GeV/c the correction becomes large because of π meson contamination due to the efficiency problems in C1 in E-472. The effect of the correction is about 10% in this region.

The corrected $C_{K^+K^-}$ is shown in Figure 30 as a function of the transverse momentum of the subscripted particles' momenta. $C_{K^+K^-}$ is flat with an average value of 1.49 ± 0.05$^{(60)}$. This value of $C_{K^+K^-}$ means that the probability of detecting a K meson of opposite charge in one arm is 49% larger when the particle in the opposite arm is a K meson instead of a π meson. This sets the scale for interpreting the ϕ data. If the ϕ were always accompanied by two additional strange particles, then one would predict $C_{\phi K} = 1.98 \pm 0.1$

To obtain $C_{\phi K}$ from the data it was first necessary to subtract the background from the ϕ region. The signal-to-noise ratio was ∿0.7. Secondly, unlike $C_{K^+K^-}$ which was found using data from a single running mode, $C_{\phi K}$ was found using data from 9 different running modes (Table 8). The low statistics involved in some of the data sets made it necessary to use a likelihood method to find $C_{\phi K}$.

The $\left[\frac{K}{\pi}\right]_\phi$ ratio for each data set was found using the guardband subtraction method previously described and applied in the following way:

$$\left[\frac{K}{\pi}\right]_\phi = \frac{K_\phi - K_B}{\pi_\phi - \pi_B} \qquad 5.16$$

K_ϕ and π_ϕ are the number of K mesons and π mesons in one

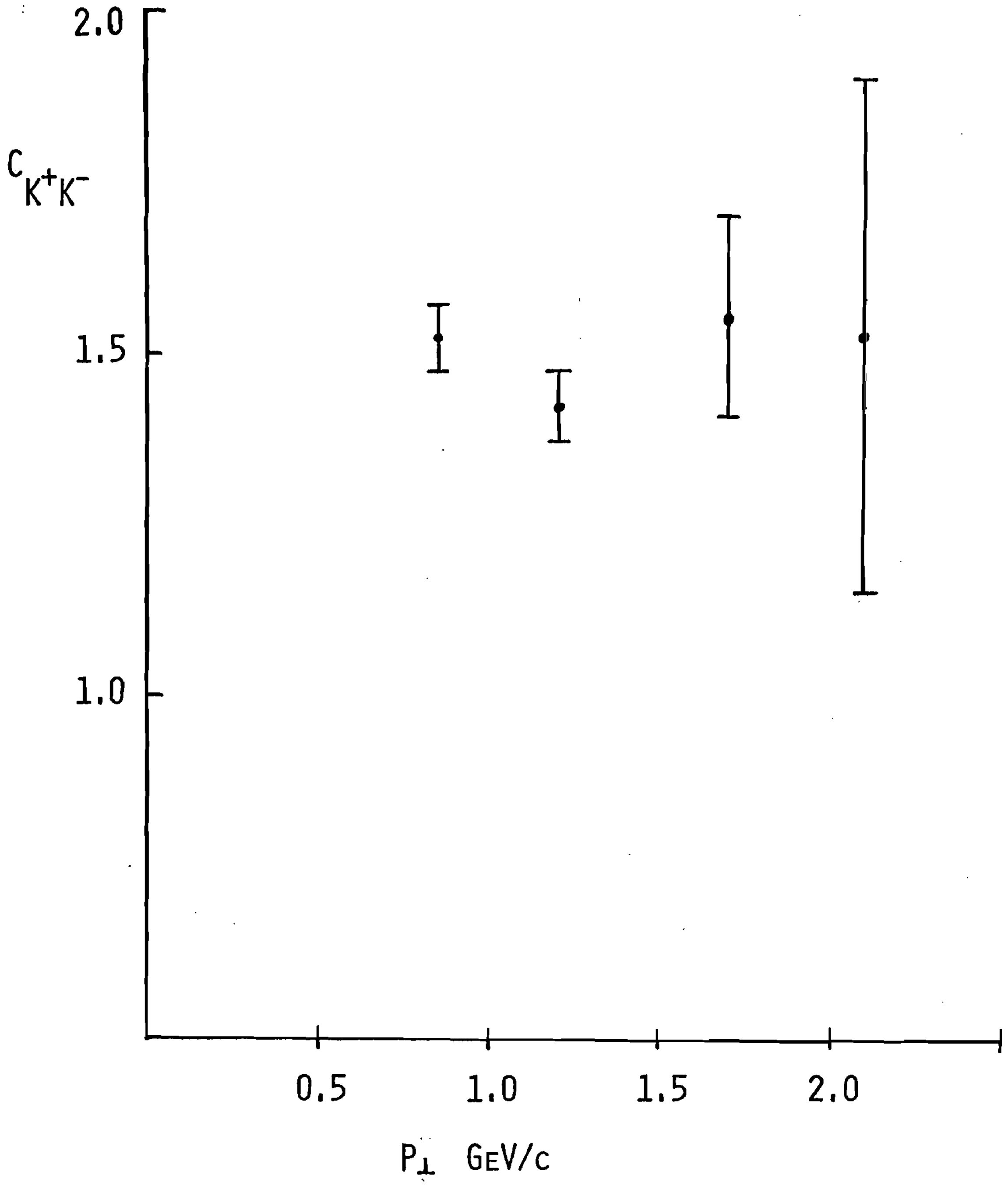

Figure 30. $C_{K^+K^-}$ as a function of transverse momentum.

arm that accompany a pair of tracks in the opposite arm which reconstruct to a mass in the ϕ mass region. K_B and π_B are the number of K and π mesons which accompany a pair of tracks in the opposite arm which reconstruct to a mass in the guardband regions. $(C_{\phi K})_i$ can now be found for each data set by dividing the result in equation 5.16 by the value $\left(\left[\frac{K}{\pi}\right]_\pi\right)_i$, which was found to be independent of the subscripted π meson's momentum (Table 8).

To perform a likelihood calculation on the nine data sets, the probability distribution of each measured set $(C_{\phi K})_i$ must be known. Looking back at equation 5.16, note that each event type of a data set i, K_{ϕ_i}, K_{B_i}, π_{ϕ_i}, and π_{B_i}, is independent of the others and was found by simply counting the number of observed events of that type. For a simple counting experiment of this type, the probability to observe each event type K_{ϕ_i}, K_{B_i}, π_{ϕ_i} or π_{B_i} may be described by the binomial distribution B(N,r,p). Here N is the number of events searched, r is the number observed and p is the probability of observation. For our experiment, the probability to observe a ϕ event in conjunction with an identified K or π meson was less than 10^{-4} of those events written on magnetic tape.

Because of this low probability of observation, the binomial distribution for each event type was approximated[42]

Data Used in O-Z-I Rule Test

Data Set	Target	K_ϕ	K_B	π_ϕ	π_B	$\left[\frac{K}{\pi}\right]_\pi$	$\delta\left[\frac{K}{\pi}\right]_\pi$	$\frac{\left[\frac{K}{\pi}\right]_\phi}{\left[\frac{K}{\pi}\right]_\pi}$	$\delta\frac{\left[\frac{K}{\pi}\right]_\phi}{\left[\frac{K}{\pi}\right]_\pi}$
1	Be	72	38	331	129	0.162	0.002	1.039	0.339
2	Be	14	8	85	32	0.147	0.004	0.770	0.623
3	Be	4	2	26	10	0.142	0.002	0.880	1.127
4	Pb	10	3	63	17	0.127	0.001	1.173	0.645
5	Pb	5	1	27	10	0.120	0.012	1.961	1.404
6	CH_2	11	8	57	24	0.141	0.001	0.645	0.953
7	CH_2	10	2	17	5	0.136	0.002	4.902	2.860
8	Be	13	5	51	31	0.150	0.003	2.667	1.860
9	Be	2	5	14	7	0.172	0.002	-2.492	2.737

Table 8. Data used in the O-Z-I rule test. δ represents the uncertainty in the following value.

by a Poisson distribution if the number of detected events was less than or equal to 25 and a Gaussian distribution if greater. The change at 25 was made in consideration of accuracy and for ease of computation using a computer. The probability distribution, $\mathbb{P}(x', x_t)$, to observe an event type with x_t counts, when the expected number is x', is then:

$$\mathbb{P}(x', x_t) = \begin{cases} \dfrac{x'^{x_t} \exp(-x')}{x_t!} & x_t \le 25 \\ \dfrac{1}{\sqrt{2\pi x'}} \exp(-(x'-x_t)^2/2x') & x_t > 25 \end{cases} \qquad 5.17$$

Note that x_t is necessarily an integer, being the number of observed counts, while x' is the expectation value and is a real number.

Knowing the individual probability distribution for an event type, the probability distribution for $(C_{\phi K})_i$ can now be found. The probability that the observed set, K_{ϕ_i}, K_{B_i}, π_{ϕ_i} and π_{B_i}, is from distributions whose expectation values are the set, K'_{ϕ_i}, K'_{B_i}, π'_{ϕ_i} and π'_{B_i}, is just the product of the individual probabilities

$$\mathbb{P}(K'_{\phi_i}, K_{\phi_i})\, \mathbb{P}(K'_{B_i}, K_{B_i})\, \mathbb{P}(\pi'_{\phi_i}, \pi_{\phi_i})\, \mathbb{P}(\pi'_{B_i}, \pi_{B_i}) \qquad 5.18$$

The probability $\mathcal{P}_i(C_{\phi K})$ to observe a given $C_{\phi K}$ is then just the sum of the joint probability distribution, over all possible combinations of expectation values which will yield the value $C_{\phi K}$. This sum can be written

$$\mathcal{P}_i(C_{\phi K}) = \underbrace{\int dK'_{\phi_i} \int dK'_{B_i} \int d\pi'_{\phi_i} \int d\pi'_{B_i}}_{\text{restricted}} \mathbb{P}(K'_{\phi_i}, K_{\phi_i}) \mathbb{P}(K'_{B_i}, K_{B_i}) \times \mathbb{P}(\pi'_{\phi_i}, \pi_{\phi_i}) \mathbb{P}(\pi'_{B_i}, \pi_{B_i}) \tag{5.19}$$

where integration is restricted such that

$$\left[\frac{K'_{\phi_i} - K'_{B_i}}{\pi'_{\phi_i} - \pi'_{B_i}}\right] \cdot \left[\frac{K}{\pi}\right]_{\pi}^{-1} = C_{\phi K} \tag{5.20}$$

This restriction may be rewritten in terms of a delta function and the integration over K'_{ϕ_i} may be performed. This yields an integral without restrictions.

$$\mathcal{P}_i(C_{\phi K}) = \int dK'_{B_i} \int d\pi'_{B_i} \int d\pi'_{\phi_i} \mathbb{P}\left(\left[\frac{K}{\pi}\right]_{\pi} \cdot C_{\phi K} \cdot (\pi'_{\phi_i} - \pi'_{B_i}) + K'_{B_i}, K_{\phi_i}\right) \times \mathbb{P}(K'_{B_i}, K_{B_i}) \mathbb{P}(\pi'_{B_i}, \pi_{B_i}) \mathbb{P}(\pi'_{\phi_i}, \pi_{\phi_i}) \tag{5.21}$$

The probability distribution $\mathcal{P}_i(C_{\phi K})$ for each data set is now known in terms of the integral equation 5.21.

The nine results may now be combined and the most likely value of $C_{\phi K}$ can be found as the maximum in the likelihood distribution[43,44].

$$L(C_{\phi K}) = \prod_{i=1}^{9} \mathfrak{J}_i \, (C_{\phi K}) \qquad 5.22$$

The integration needed to find the values of $\mathfrak{J}_i(C_{\phi K})$ was done using a Monte Carlo integration technique[45]. The resulting likelihood distribution for $C_{\phi K}$ is shown in Figure 31. The most likely value and variance is[46]:

$$C_{\phi K} = 1.04 \pm 0.21 \qquad 5.23$$

This result implies the ϕ meson has no correlation to K mesons. Comparing the measured value of $C_{\phi K}$ to its predicted value of 1.98 ± 0.1 suggests that the ϕ meson is produced primarily by a mechanism that does not produce additional strange particles and hence production could be in violation of the O-Z-I rule. The possibility that the O-Z-I rule does hold in ϕ production but the production is in a configuration which disallows detection in our spectrometer cannot be ruled out. Such an example would be a jet model. In this case, the ϕ meson along with a pair of strange particles would move in the direction of a single spectrometer arm. This explanation is hard to understand when a K^+K^- correlation is seen which is large and flat to beyond a transverse momentum of 2 GeV/c, while the average transverse momentum of the ϕ data set is $\sim$1.8 GeV/c.

Another explanation could be that the production of

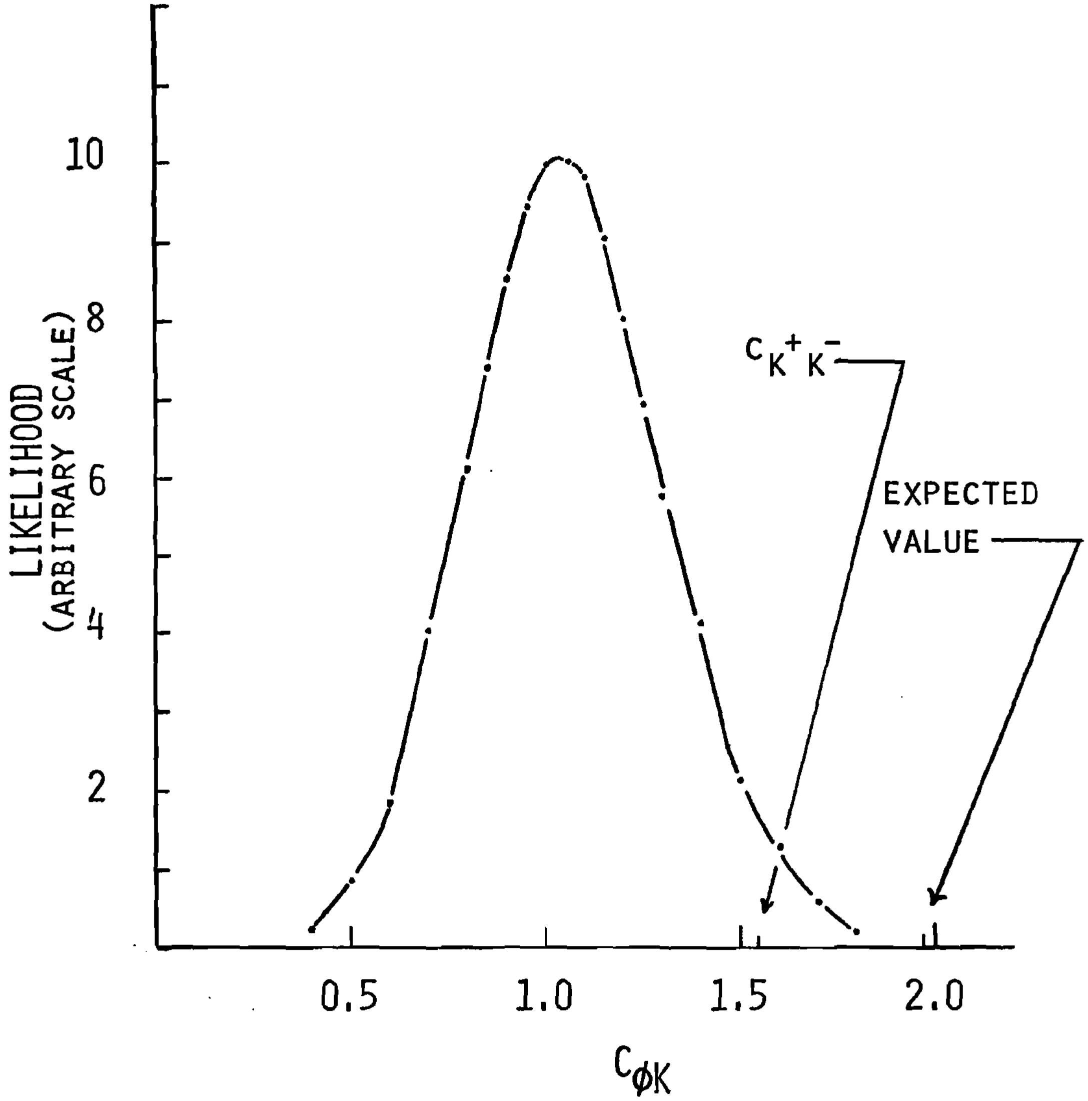

Figure 31. The likelihood distribution for $C_{\phi K}$.

ϕ mesons in proton-nucleus collisions is through the small admixture of nonstrange quarks in the ϕ wave function. Using the ϕ quark wave function in equation 1.6 and the ω quark wave function in Table 1, one finds the expectation of ϕ production through nonstrange quarks to be

$$\sigma_{\phi}^{\text{nonstrange}} = |\langle\omega\ \phi\rangle|^2 = 0.003 \pm 0.001\ \ \sigma_{\omega} \qquad 5.24$$

The cross section for ω production is not known at these energies, but an upper limit of $\omega/\pi^0 < 1$ at an average $P_\perp$ of 3.5 GeV/c has been measured at a higher center-of-mass energy[61]. This indicates that our measured ϕ/π^- ratio of $\sim$0.07 in the same $P_\perp$ range, is more than an order of magnitude larger than that expected by production through nonstrange quarks alone.

Although the ω/π ratio is not known the ρ^0/π^0 ratio is known to be 0.13 ± 0.02 at an average transverse momentum of 0.5 GeV/c, using a 200 GeV/c proton beam[47]. ρ^0/π^0 is also known to be 0.9 ± 0.2 at an average transverse momentum of 3.5 GeV/c in p p collisions at a center-of-mass energy of 54 GeV [61]. Because we expect ω and ρ^0 production to be nearly equal[62] we can write the prediction for ϕ production through the nonstrange quarks in its wave function as

$$\frac{\phi}{\pi}^{\text{nonstrange}} = |\langle\omega\ \phi\rangle|^2 \cdot \frac{\rho^0}{\pi^0} \qquad 5.25$$

The result, using this equation and the known data, is shown in Figure 32. Also shown is a thermodynamic model fit (equation 5.9) constrained by the lowest $P_\perp$ point. As can be seen the ϕ/π^- ratio is more than an order of magnitude larger than the nonstrange production estimate, indicating that the ϕ meson at this energy is produced predominately through the strange quarks in its wave function[63].

There are no other experimental tests of the O-Z-I rule at high energies involving ϕ meson production, but tests have been done at lower energies. The most comparable was done by V. Blobel, et al.,[51] which observed ϕ production in p p collisions at 24 GeV/c. They compared the average number of strange particles produced in conjunction with a ϕ meson to the average number produced with a $K^+ K^-$ pair. The result showed no enhancement of strange particle production in association with the ϕ, implying an O-Z-I violation. They conclude that in their energy region, ϕ production is strongly dominated by production through the nonstrange quarks in the ϕ wave function, which explains the apparent O-Z-I violation.

Another test has been done[48], observing exclusive reaction channels involving ϕ, ω, and ρ mesons, in which the ϕ is produced in an O-Z-I disallowed reaction. Such tests search for an enhancement of ϕ production above the level allowed by ω-ϕ mixing, indicating a violation of the O-Z-I rule. But at these energies ($\leq$ 20 GeV/c), any enhancement is difficult to observe because ϕ production is largely

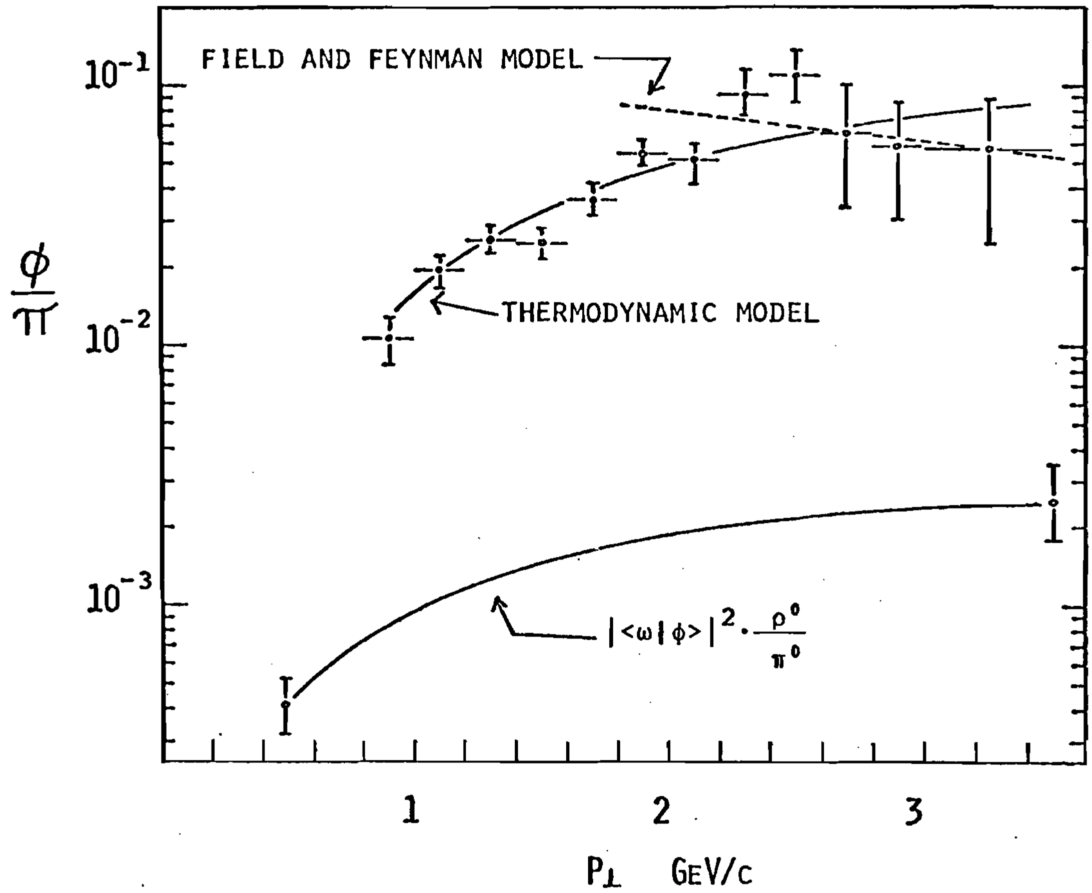

Figure 32. The ϕ/π^- ratio, showing the estimated contribution to ϕ production from the admixture of nonstrange quarks in its wave function. The line through the data points is a thermodynamic model fit (equation 5.9) constrained by the lowest $P_\perp$ point.

through the nonstrange quarks in its wave function.

There are two experiments which observe exclusive reactions in low energy collisions, which suggest that the "excess" ϕ production (that not accounted for by ω-ϕ mixing) is in accordance with the O-Z-I rule. The first is in π^- p collsisions at 19 GeV/c[49] and the other is in $\bar{p}$ p collisions at 3 GeV/c (50). Both find a large enhancement in the production of ϕK^+K^- over that predicted using ω-ϕ mixing and their measured ϕ π^+ π^- cross section. The ratio $(\phi\pi^+\pi^-)/(\phi K^+K^-)$, as measured by reference (49) was found to be 1.7. The value seems to indicate a violation of the O-Z-I rule, but is again explainable by the admixture of nonstrange quarks in the ϕ wave function.

These results suggest that in low energy collisions the ϕ meson is predominately produced without associated strange particles, because production is largely through the nonstrange quarks in the ϕ wave function. However, ϕ production above the level allowed for by ω-ϕ mixing is produced in accordance with the O-Z-I rule. These results are in contrast to our high energy ϕ result which suggests dominant production through the strange quarks in the ϕ wave function and an O-Z-I violation.

Other high energy tests of the O-Z-I rule have been done, observing the J/Ψ production in 400 GeV/c proton-nucleus collisions. Two experiments[52,53] have searched for J/Ψ production in association with other charmed particles.

The present upper limit is

$$\frac{\sigma_{J/\Psi} + c\bar{c}}{\sigma_{J/\Psi}} < 0.01 \qquad 5.26$$

This indicates a strong O-Z-I violation in the production of J/Ψ. To explain the observed violation, models have been proposed[54,55] in which the gluons, in the hadrons, collide and become an important source of J/Ψ mesons. Because the φ is also a vector meson, like the J/Ψ, similar mechanisms could account for O-Z-I violating φ production at these energies.

Summary

φ meson production has been observed in 400 GeV/c proton-nucleus collisions using a high resolution double arm spectrometer, centered near 90 degrees in the center-of-mass. An accurate measurement of the φ mass and width was made and an analysis of the systematic error in the measurements was carried out. The inclusive φ invariant cross section was measured over the range $0.8 \lesssim P_\perp \lesssim 3.5$ GeV/c and the slope parameter was found. The ϕ/π^- ratio as a function of $P_\perp$ was found and compared to the thermodynamic model and the Field and Feynman model. The comparison suggested that φ production may be dominated by different mechanisms at low and high $P_\perp$. Using the measured ϕ/π^- ratio and the known $\phi \rightarrow \mu^+\mu^-$ branching ratio, the φ meson's contribution to the prompt μ/π ratio was found as a function of $P_{\perp}$. The ϕ meson's contribution was found to be almost 2 orders of magnitude below the total μ/π ratio. A test of the O-Z-I rule was made by searching for an enhancement of K mesons produced in association with the ϕ. No enhancement was found indicating a possible violation of the O-Z-I rule. This lack of enhancement could not be explained away by ϕ production through nonstrange quarks in its wave function or easily by a jet model production mechanism because of the large $K^+ K^-$ correlation observed.

APPENDIX A

MULTIPLE SCATTERING

The mass resolution of the detector is the result of multiple scattering and to lesser extent drift chamber resolution. The resolution due to multiple scattering was found using the small-angle multiple scattering approximation. The approximation consists of setting[56]

$$\begin{aligned} \sin(\Theta) &= \Theta \\ \cos(\Theta) &= 1 \end{aligned} \qquad \text{A.1}$$

where Θ is the scattering angle. This yields the relationship

$$\Theta^2 = \phi_x^2 + \phi_y^2 \qquad \text{A.2}$$

for the projected scattering angles ϕ_x and ϕ_y (Figure 33).

If we assume that a single scattering is described by Rutherford's scattering formula and that there is no energy loss in the scattering region (the energy loss is less than 5 MeV for any scattering region in the spectrometer making the energy loss about 0.05% of the particles total energy). Then one finds that the mean square scattering angle is described by[57]

$$\langle\Theta^2\rangle = \left[\frac{21\ \text{MeV}}{p\cdot c}\right]^2 \frac{X}{X_o} \qquad \text{A.3}$$

where X is the length of the scattering material and X_o is the radiation length. p is the momentum in MeV/c and c is

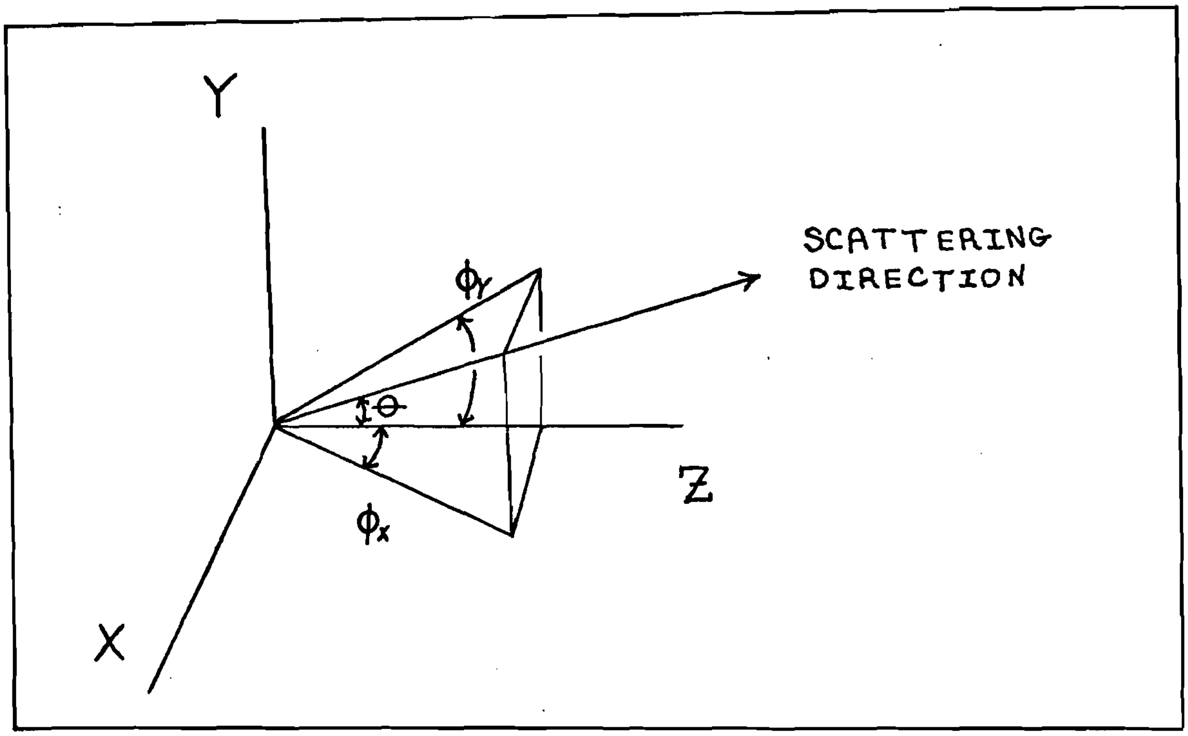

Figure 33. The relationship between the multiple scattering angle θ and the projected scattering angles ϕ_x and ϕ_y.

the speed of light in vacuum. Using typical values for the spectrometer one finds the mean square scattering angle to be $\sim 5 \cdot 10^{-8}$. Thus the small angle approximation is very reasonable.

In order to have multiple scattering in the Monte Carlo, the projected multiple scattering distribution $P(z,y,\phi_y)\,dy\,d\phi_y$ must be known. This distribution describes the number of particles at thickness z, having a displacement y, and traveling at a projected angle ϕ_y , when a beam of particles is incident in the z direction at y=0, z=0. Rossi[58] develops the following differential form for $P(z,y,\phi_y)$:

$$\frac{\partial P}{\partial z} = -\phi_y \frac{\partial P}{\partial y} + \frac{\langle\Theta^2\rangle}{4z} \frac{\partial^2 P}{\partial \phi_y^2} \qquad \text{A.4}$$

whose solution is given by[58]

$$P(z,y,\phi_y) = \frac{2\sqrt{3}}{\pi} \frac{1}{z\langle\Theta^2\rangle} \exp\left[\frac{-4z}{\langle\Theta^2\rangle}\left(\frac{\phi_y^2}{z} - \frac{3y\phi_y}{z^2} + \frac{3y^2}{z^3}\right)\right] \qquad \text{A.5}$$

This is the projected multiple scattering distribution for a single scattering material. The form of $\langle\Theta^2\rangle$ suggested by Highland[59] was used to help account for the long non-Gaussian tails of the scattering distribution.

Rossi's form of $P(z,y,\phi_y)$ describes scattering from only one type of material. In order to speed up the Monte Carlo calculations, the distribution for N different materials needed to be found. Consider the case of two materials. In this case the resultant distribution is[56]

$$P(z,y,\phi_y)=dy\ d\phi_y \int_{-\infty}^{\infty}\int_{-\infty}^{\infty} dy_1\ d\phi_{y_1} P(z_1,y_1,\phi_{y_1})P(z-z_1,y-y_1,\phi_y-\phi_{y_1}) \qquad \text{A.6}$$

where [64]

$$\begin{aligned} \phi_y &= \phi_{y_1} + \phi_{y_2} \\ y &= y_1 + y_2 \\ z &= z_1 + z_2 \end{aligned} \qquad \text{A.7}$$

Now take the Fourier transform of equation A.6

$$\tilde{P}_2(z,\eta,\varepsilon) = \int_{-\infty}^{\infty} d\phi_y\ \text{EXP}(i\varepsilon\phi_y) \int_{-\infty}^{\infty} dy\ \text{EXP}(i\eta y) \quad x$$
$$\int_{-\infty}^{\infty}\int_{-\infty}^{\infty} dy_1\ d\phi_{y_1} P(z_1,y_1,\phi_{y_1})P(z-z_1,y-y_1,\phi_y-\phi_{y_1}) \qquad \text{A.8}$$

We find

$$\tilde{P}_2(z,\eta,\varepsilon) = \tilde{P}(z_1,\eta\ ,\varepsilon\ )\tilde{P}(z_2,\eta\ ,\varepsilon\ ) \qquad \text{A.9}$$

The resulting projected multiple scattering distribution for N different materials is then

$$P(z,y,\phi_y)= \int_{-\infty}^{\infty} d\varepsilon \int_{-\infty}^{\infty} d\eta\ \ \tilde{P}_N(z,\eta,\varepsilon)\ \text{EXP}(-i\varepsilon\phi_y)\ \text{EXP}(-i\eta y) \qquad \text{A.10}$$

The integral in equation A.10 can be found analytically if the projected multiple scattering distribution for an individual material is described by equation A.5.

This method yields a multiple scattering algorithm which can be performed quickly by a computer (approximately 7 lines of Fortran code). This becomes important when it may be used 10^6 times in the course of a Monte Carlo calculation.

The final test of the method and code is to compare the resultant mass resolution with the data in the experiment. This can be done in our experiment using the J/Ψ signal observed in its $\mu^+\mu^-$ decay mode and the K_s^0 signal observed in its $\pi^+\pi^-$ decay mode. Both have negligible width in comparison to their experimental mass resolution (Table 9). As can be seen in Table 9 , there is good agreement between the experimentally measured mass resolution and the mass resolution found by the Monte Carlo.

Figure 34 shows the observed J/Ψ and K_s^0 signals.

Resolution Comparison

Particle	Experimental Mass Resolution	Monte Carlo Calculation
J/Ψ	8.6 ± 1.5 $\mathrm{MeV/c^2}$	7.5 $\mathrm{MeV/c^2}$
K^o_s	3.20 ± 0.26 $\mathrm{MeV/c^2}$	3.39 $\mathrm{MeV/c^2}$
ϕ	- -	0.83±0.09 $\mathrm{MeV/c^2}$

Table 9. Comparison of J/Ψ and K^o_s experimental mass resolution with the Monte Carlo calculation.

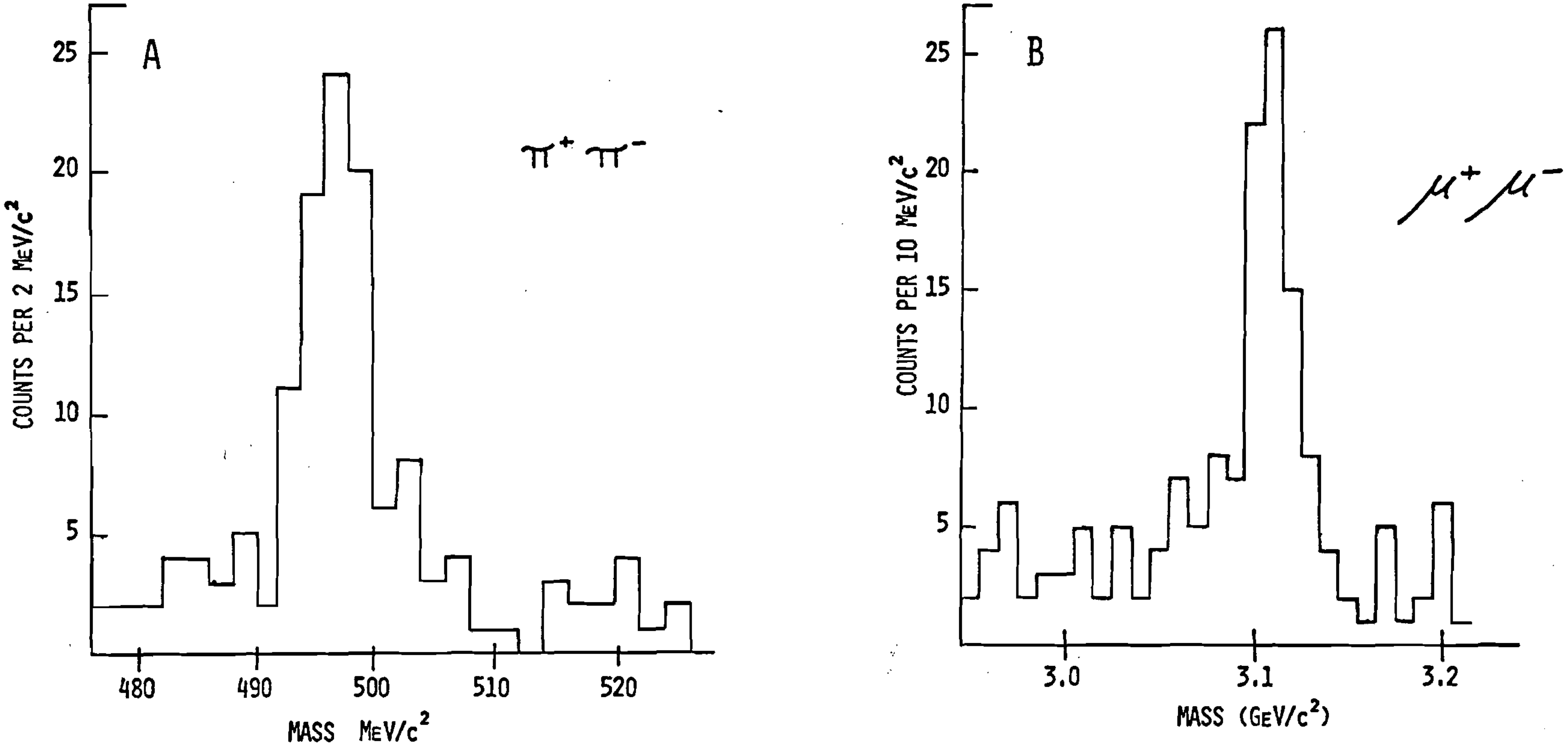

Figure 34. The K_s^0 and J/Ψ signals observed in this experiment. A.) the K_s^0 signal used to calibrate one of the magnets. B.) The total J/Ψ signal observed in this experiment.

REFERENCES

1. B. J. Bjorken and S. L. Glashow, Phys. Lett., 11 (1964) 255; S. L. Glashow, J. Iliopoulos, and L. Maiani, Phys. Rev., D2, (1970) 1285; M. K. Gaillard, B. W. Lee and J. L. Rosner, Rev. Mod. Phys., 47 (1975) 277.

2. D. Bintinger, et al., Phys. Rev. Lett., 37 (1976) 732; W. R. Ditzler, et al., Phys. Letters, 71B (1977) 451.

3. C. W. Akerlof, et al., Phys. Rev. Lett., 39 (1977) 861.

4. H. Fritzsch, M. Gell-Mann and H. Leutwyler, Phys. Lett. B47 (1973) 365; D. J. Gross, F. Wilczek, Phys. Rev., D8 (1973) 3633; S. Weinberg, Phys. Rev. Lett., 31 (1973) 494.

5. L. W. Jones, Rev. Mod. Phys., 49 (1977) 717.

6. T. Appelquist and H. D. Politzer, Phys. Rev. Lett. 34 (1975) 43.

7. M. Gell-Mann and Y. Ne'eman, Eight-Fold Way, (W. Benjamin, Inc., New York and Amsterdam, 1964)

8. S. Okubo, University of Rochester Report UR-616, 1976.

9. J. J. Sakurai, Phys. Rev. Lett., 9 (1962) 472.

10. S. Okubo, Phys. Lett., 5 (1963) 165.

11. G. Zweig, CERN Report Th-412 (1964).

12. J. Iizuka, Prog. Theor. Phys. Suppl., 37-38 (1966) 21.

13. V. Blobeh, et al., Phys. Lett., 59B (1975) 88.

14. J. D. Jackson, Proceedings of Summer Institute on Particle Physics, Stanford Linear Accelerator Center SLAC Report No. 198, 1976.

15. H. J. Lipkin, et al., Weizmann Institute of Science Report WIS-78/23 Ph.

16. D. Cohen, et al., Phys. Rev. Lett. 38 (1977) 269.

17. G. Alexander, et al., Phys. Rev. Lett.,17(1966)412.

18. H. Schopper, DESY at Hamburg, Germany, Report No. 77/79 (1977).

19. R. D. Field and R. P. Feynman, California Institute of Technology Report No. Calt-68-618(1977); R. D. Field and R. P. Feynman, Phys. Rev. ,D15(1977)2590.

20. G. Miller, at el., Phys. Rev.,D5(1972)529.
A. Bodek, et al., Phys. Rev. Lett., 30(1973) 1087.

21. H. Deden, et al., Nuclear Physics,B85(1975)269.

22. R. Hagedorn, Sup. Al Nuovo Cimento, VI(1968)311.
R. Hagedorn, Sup. Al Nuovo Cimento, III(1965)147.

23. H. Nilles, Nuclear Physics,B121(1977)151.
S. C. Frautschi, et al., Nuclear Physics,B121(1977)141.
S. C. Frautschi, et al., University of Hawaii Report No. UH-511-255-76.

24. L. M. Letterman, Phys. Reports, 26,No.4(1976)149.

25. M. Bourquin and J. M. Gaillard, Phys. Lett. 59B(1975) 191.

26. J. A. Appel, et al., Phys. Rev. Lett., 35(1975) 9.

27. N. S. Craigie, Imperial College, London Preprint 3 January 1978.

28. D. D. Yovanovitch, et al., Argonne National Lab. Report No. ANL/HEP 7104.

29. R. Thun,et al., Nuclear Instruments and Methods 138 (1976)437.

30. J. D. Jackson, Nuovo Cimento,34,Ser.10,II(1964)1644.

31. P. M. Endt, et al., Phys. Lett., 75B(1978).

32. S. P. Denisov,et al.,Nuclear Phys.,B61(1973)62.

33. P. V. R. Murthy, et al., Nuclear Phys.,B92(1975)269.

34. K. J. Anderson, et al., Phys. Rev. Lett.,37(1976)803.

35. L. Kluberg, et al., Phys. Rev. Lett.,38(1977)670.

36. D. Antreasyan, et al., Phys. Rev. Lett.,38(1977)112.

38. S. C. Frautschi, et al., University of Hawaii at Manoa Report No. UH-511-255-76.

39. G. G. Henery, *Measurement of Inclusive Low Mass Muon Pairs*, Thesies, Enrico Fermi Institute, The University of Chicago, 1978.

40. F. Halzen and D. M. Scott, University of Wisconsin Physics Depart. Report No. COO-881-45,July, 1978.

41. We also observe a strong P-$\overline{P}$ correlation, with an enhancement of 82%.

42. In this case the approximation is very reasonable and may be found in many books:see reference (44).

43. R. Raja, Fermi National Lab., private communication.

44. W. T. Eadie, et al.,*Statistical Methods in Experimental Physics*,North-Holland Publishing Comp. 1971.

45. D. T. Gillespie, *Monte Carlo Method of Evaluating Integrals*, Navel Weapons Center Report No. NWC TP 5714.

46 This method may be compared to the very simple method of taking the error in each number as $\sqrt{N}$. The result is $C_{\phi K} = 1.04 \pm 0.26$.

47. R. Singer, et al., Phys. Lett., 60B(1976)385.

48. R. Baldi, et al., Phys. Lett., 68B(1977)381.

49 P. L. Woodworth, et al.,CERN Report No.EP-Phys. 76-53 1976.

50. R. A. Donald, et al., Phys. Lett.,61B(1976)210.

51. V. Blobel, et al., Phys. Lett., 59B(1975)88.

52. M. Binkley, et al., Phys. Rev. Lett., 37 (1976) 578.

53. J. G. Branson, et al., Phys. Rev. Lett., 38 (1977) 580.

54. M. Teper, Phys. Lett., 68B (1977) 183.

55. M. B. Einhorn, et al., Phys Rev., D12 (1975) 2007.
S. D. Ellis, et al., Phys. Rev. Lett., 36 (1976) 1263.

56. W. T. Scott, Rev. Mod. Phys., 35 (1963) 231.

57. B. Rossi and K. Greison, Rev. Mod. Phys., 13 (1941) 240.

58. B. Rossi, *High Energy Particles*, (Prentice-Hall, Englewood Cliffs, N.J., 1961)

59 V.L. Highland, Nuclear Instruments and Methods 129 (1975) 497.

60. Before correction the average was 1.45 .

61. P. Darriulat, et al., Nuclear Physics, B107 (1976) 429.

62. In both the thermodynamic model and the Field and Feynman model $\sigma_\omega = \sigma_\rho$. This is reasonable because $m_\omega \sim m_\rho$ and both are made of u and d quarks.

63. Scaling the known data using $x_\perp = 2 P_\perp/\sqrt{s}$ may have been more appropriate. Doing so does not change the the estimate of ϕ production through nonstrange quarks.

64. Here y_1 is the particles position at z, as if material 2 had not been present. In the small angle aproximation this is written $y_1 = z_2\phi_{y_1} + y_1'$. where y_1' is the particles displacement after transversing material 1.